THE UNIVERSITY OF ALBERTA

MECHANISM OF HYDROGEN EVOLUTION REACTION AT STAINLESS STEEL 304 IN STRONG SODIUM HYDROXIDE SOLUTIONS

by

PHILIP SETO

A THESIS

SUBMITTED TO THE FACULTY OF GRADUATE STUDIES

IN PARTIAL FULFILMENT OF THE REQUIREMENTS FOR THE DEGREE

OF MASTER OF SCIENCE

DEPARTMENT OF CHEMISTRY

EDMONTON, ALBERTA

APRIL 1968

UNIVERSITY OF ALBERTA

FACULTY OF GRADUATE STUDIES

The undersigned certify that they have read, and recommend to the Faculty of Graduate Studies for acceptance, a thesis entitled

MECHANISM OF HYDROGEN EVOLUTION REACTION AT STAINLESS STEEL 304 IN STRONG SODIUM HYDROXIDE SOLUTIONS

submitted by PHILIP SETO, B.Sc.

in partial fulfilment of the requirements for the degree of Master of Science.

ACKNOWLEDGEMENTS

The author wishes to express his gratitude to Dr. R. N. O'Brien for his guidance and helpful criticisms and to Dr. K. V. N. Rao for his assistance in starting this work. The value of the suggestions of Dr. J. Leja and Roger Parsons concerning the course pursued in the time domain reflectometry investigation are also gratefully acknowledged.

This work has been made possible through the grants of the National Research Council of Canada and the Defence Research Board of Canada.

ABSTRACT

The hydrogen evolution reaction mechanism at an austenitic stainless steel (type 304) electrode in strong NaOH solutions was determined as a slow discharge of a water molecule followed by fast Tafel recombination. Hydrogen overpotentials were obtained by the dc interruptor technique. Effects of anions F^-, Cl^-, I^- as well as effects of multivalent cations Ba^{+2} and La^{+3} on the H overpotential were studied. Also, effects of changing the metal surface by long time electrolysis, those of electrodeposition of elemental Fe and Ni onto the alloy surface, and those of pickling the surface with 1:1 HCl/H_2SO_4 acid mixture were studied. Surface concentrations of adsorbed reaction intermediates MH were obtained by the galvanostatic stripping and the potential step methods.

The technique of time domain reflectometry, a closed-loop radar method, was introduced to measure the electrical double layer capacities at the stainless steel-alkali interface.

TABLE OF CONTENTS

LIST OF TABLES

LIST OF FIGURES

LIST OF SYMBOLS

C	electrode capacity
O	species in the oxidized state
R	species in the reduced state
ze	no. of moles of electrons
F	Faraday (96,494 coulombs)
k_1, k_{-1}, k_2, k_3	specific rate constants
ΔG_1^*, ΔG_{-1}^*, ΔG^*	free energies of activation
ε_o, ε_m	reversible, measured electrode potential
η	overpotential
k	Boltzmann constant (1.38×10^{-16} erg/deg.)
h	Planck constant (6.62×10^{-27} erg. -sec.)
T	absolute temperature
exp or e	exponential
R	gas constant
v_1', v_{-1}', v_1, v_2, v_3	chemical rates
i_1, i_{-1}, i_2, i_3	electrochemical rates (amp./cm^2.)
i_o	exchange current density
i_c	cathodic rate
ν	stoichiometric number
a	η at 1 amp./cm^2.
b	Tafel slope
α, β	transfer coefficient or symmetry factor
μ, $\bar{\mu}$	chemical, electrochemical potential
M	metal site or atom
θ_H	fraction of electrode surface covered with H

η_r	ohmic overpotential
δ	distance of electrode from Luggin capillary tip
κ	specific conductance of electrolyte
d	outer diameter of Luggin capillary tip
C_H, C_M	concentration of atom H, metal atoms (moles/cm^2.)

LIST OF APPENDICES

INTRODUCTION

The hydrogen evolution reaction is a complex reaction. It is a consecutive electrode reaction which involves chemisorption of an adsorbed intermediate. "In this respect full agreement has not yet been reached on the mechanism of hydrogen ion discharge on various metals after more than half a century of intensive work."[1] As a result, theories on the mechanism of h.e.r. are most abundant and a simple universal theory of hydrogen overvoltage does not exhist. Because of this abundance of literature written on electrode kinetics, only general considerations of the theories of the electrical double layer, charge transfer, and electrochemical kinetics will be presented in this work.

While the hydrogen evolution reaction mechanism was most frequently studied at the platinum[2], the dropping mercury[3], and the nickel [4,5,6,7] cathodes, it has yet to be determined at the commercial stainless steel type 304 metal in strong sodium hydroxide solutions. The elemental composition of commercial stainless steel type 304 is listed as 18-20% Cr, 8-12% Ni, 1% Si, 0.03% S, 0.045% P, 2% Mn, 0.08% max. C, and the rest Fe. The structure of the alloy is therefore very complex. Furthermore, a passivating film of unknown structure and nature exists on the surface on exposure to air or oxidizing agents[8]. The thickness of the ultra-thin film ranged from 30 to 60 A°[9]. This passive film could be removed either by cathodic polarization or pickled with HCl[8], or bromine-methanol solution[9].

It is the purpose of this work to elucidate the mechanism of h.e.r. at the commercial stainless steel type 304 metal in strong sodium hydroxide solutions. Polarization curves were obtained by

the dc electronic interruption technique. Neutral salt effects were studied. A number of methods were employed to determine the surface activity of the metal. Measurements of the concentration of reaction intermediates by current and potential charging pulses were attempted. Finally, the method of time domain reflectometry was introduced to measure the electrical double layer capacity at the stainless steel-alkali solution interface and is reported in Appendix I.

THEORY

Electrical Double Layer

When a metal comes into contact with an electrolytic solution there appears a double layer of opposite charges at the interface. The mechanism of its formation is that the ions and solvent molecules tend to be redistributed between the two phases in accordance with the difference in their standard electrochemical potential. The redistribution of the particles to form an electrical double layer can be distinguished by: (i) charge transfer across the interface, (ii) unequal adsorption of ions of opposite charges, (iii) adsorption and orientation of dipolar molecules, and (iv) deformation of polarizable atoms or molecules in the unsymmetrical force field at the interface[10]. Two or more of these effects may be present at a simple interface, hence, the electrical double layer may consist of many regions or layers.

Helmholtz[11] was the first to realize the existence of this electrical double layer. He pictured it as a parallel plate condenser having an electrode capacity C. In effect, this model shows that the separate charges are in electrostatic equilibrium and no charge transfer can take place in either direction across the double layer. As a result, this double layer is purely capacitative and no transfer of charges for a net electrode reaction can take place[12].

Gouy[13] pointed out that thermal motions of ions and molecules can occur causing a certain amount of diffuseness of the charge on the electrolyte side of the double layer. This distribution is analogous to that of the ionic atmosphere of Debye and Hückel and as the preponderance of ions of opposite charge to the electrode decreases with distance becomes identical with it. Chapman[14] worked out the mathematical equation at the same time. Thus, the Gouy-Chapman

theory shows that the electrolyte side of the double layer is effectively the ionic atmosphere of the electrode. Parsons[10], however, pointed out two wrong assumptions made by the Gouy-Chapman theory. The first assumption is that the ions were discreet charges, that is, the work in bringing the ions up to the electrode surface depends only on the valency and not the nature of the ion. Since the Poisson equation is used for the mathematicsl derivation, it includes the mean dielectric constant value which is invalid because the dielectric constant of a liquid such as water depends on the field strength at the electrode-electrolyte interface. Malsch[15] indicated that field strengths of more than 2.5×10^5 volt/cm. will change the dielectric constant of water. As such, calculations from the Gouy-Chapman model did not compare with experimental capacity-potential profiles.

Stern's model[16] assumed that the ions have a finite size and approach the electrode only to a certain critical distance. Also in certain cases the anions may be chemisorbed or specifically adsorbed on the metal surface. This model is characterized by an inner region called the Helmholtz layer and an outer diffuse layer. A detailed analysis[10] showed that the distance of closest approach of ions and the distance of metal surface to the specifically adsorbed ions are not the same. Grahame[17] called the inner layer of ions at potential ψ_2, the inner Helmholtz layer, and the layer at potential ψ_1, the outer Helmholtz layer as shown in Fig. 1a. The nature of the forces of interaction of specific adsorption involves the formation of some sort of covalent bond between the ion and the metal surface. Devanathan et al[18] considered both electronic-image energy and ionic solvation being the chief factors involved in specific adsorption. Whatever the actual nature of the forces of interaction which bring

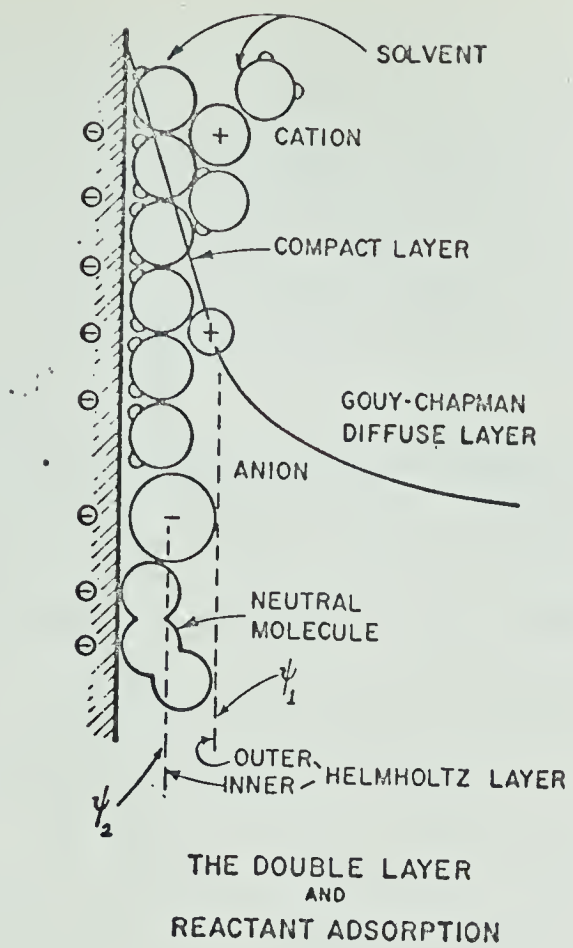

Fig. 1a. Grahame's Model of Electrical Double Layer

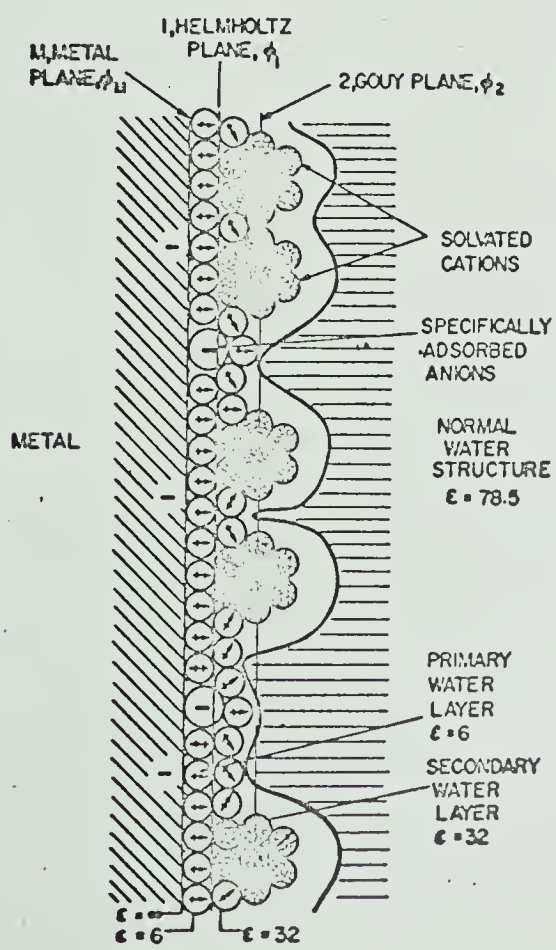

Fig. 1b. Hydration Model of Electrical Double Layer

about specific adsorption, it is generally agreed that an ion must lose its solvation sheath on the side opposite the metal before the ion can penetrate into the inner layer and become specifically adsorbed. Nevertheless, the Stern-Grahame model gives a better agreement than that of Gouy-Chapman.

Up to now, the treatments mentioned regarded the dielectric constant at the electrical double layer as having a normal value. As mentioned previously, an electric field strength greater than 2.5×10^5 volts/cm. can cause dielectric saturation[15]. With the exception of the smallest potential difference at the electrode-solution interface, the field close to the metal surface is of the order of 10^5-10^7 volts/cm.[12] Specific orientation of solvent molecules due to chemical interactions with the metal surface will also cause a dielectric loss. It is generally agreed that the electric field at the diffuse layer is not great enough to cause a dielectric depression. With the magnitude of the electric field mentioned, the electrostatic pressure is about 50,000 atmospheres. Hence, there is an electrostatic effect at the interface[12]. MacDonald[19] accounted for both dielectric saturation and electrostatic effects in his mercury electrode. The potential dependence of a contribution from adsorbed water dipoles to the electrode surface was discussed by Mott and Watts-Tobin[20]. Recently, Devanathan et al[18] regarded the inner layer as being populated by strongly adsorbed solvent dipoles. Chemisorbed anions are regarded as being able to penetrate the inner solvent layer. Hydrated cations are regarded as remaining outside the solvent layer as shown in Fig. 1b. This satisfactorily explains the fact that the cathodic capacity is largely independent of cation radius. Water molecules are regarded as being potentially

adsorbed with their negative ends pointing either toward or away from the electrode surface, depending on the electrode charge. The dielectric constant of this primary hydration layer has a value approaching the limiting Maxwell value. The layer containing the adsorbed cations has a higher dielectric constant.

In general the electrical double layer consists of the metallic phase, an inner layer a few molecular diameters thick located next to the electrode surface and an outer or diffuse layer. The metallic phase has a net electrical charge on the surface because of an excess or deficiency of electrons imposed on the electrode by means of an external source of electric current or as a result of faradaic electrode processes. The inner layer on the solution side of the interface contains solvent molecules and sometimes other neutral molecules adsorbed on the metal surface. Sometimes, anions may be specifically adsorbed via a covalent bond. The plane across the electrical centers of the adsorbed ions is called the inner Helmholtz plane. Whenever the interaction between an ion and the metal is not strong enough to bring about desolvation, the ion will not be able to come as close. The plane passing through the centers of the solvated ions is known as the outer Helmholtz plane. Unlike specifically adsorbed ions at the inner Helmholtz plane which form a two-dimensional monolayer, the nonspecifically adsorbed ions are not all located at the outer Helmholtz plane but are contained in a three-dimensional region, the diffuse layer, which extends all the way from the outer Helmholtz plane into the bulk of the solution. Thermal agitation results in the diffuse layer which provides the ionic atmosphere of the electrode.

Many groups[21] considered the reactants as located in the outer Helmholtz plane. The Boltzmann distribution of the activities of the

reactants was incorporated into the kinetic expression to include the double layer influence on electrode processes. Breiter et al[22] suggested that the effective difference in potential which enhances or retards the electrode reaction may be the potential difference between the measured potential and the potential between the electrode and the plane of closest approach.

Charge Transfer

That the ionic discharge or the atomic ionization step was the slow or rate-controlling step was proposed by Erdey-Gruz and Volmer[23]. A change in electrode potential would cause a change in activation energy of the discharge or ionization stage, and thus the rate of the whole process is affected. From the slow discharge mechanism, two hypotheses resulted: (i) the electronic mechanism where the elementary process consists of a jump of an electron from the metal to an ion in solution, which simultaneously dehydrates and deposits as a neutral atom on the electrode, and (ii) the ionic mechanism where the ion in its hydrated state migrates to the electrode where it is neutralized. Guerny[24] and Butler[25] applied quantum mechanical theory to charge transfer at electrodes. Christov[26] concluded that the transfer of ions from solution to the electrode or from electrode to the solution proceeded as a transfer through a potential barrier in the Helmholtz layer by means of a tunnel effect. He also affirmed that quantum mechanics should be employed to derive kinetic equations when light ions were involved. Proton tunneling through the potential barrier was considered by Conway[27]. Applying the Franck-Condon principle, Libby[28] demonstrated that the electron transfer processes in solution are very rapid compared to the reorientation of the solvent and ligand

shell around the reactive species. In his theory, Marcus[29] assumed that only weak electronic interactions of the electrode and an ion or molecule is required for a simple electron transfer process to occur. From quantum mechanical deductions of his basic assumption, Marcus concluded that the solvent configuration about reacting species gradually changed during the reaction to a configuration compatible with the product. Also using quantum mechanics, Hush[30] showed that most of the activation energy was due to dielectric reorientation outside the first co-ordination shell around the ions.

Electrode Kinetics

A number of authors[31-38] have dealt with the fundamentals of electrode kinetics. All electrode kinetic derivations start with the reversible systems before an applied electric field effect across the electrode-electrolyte interface is considered.

Reversible electrode processes are considered to be in a state of reversible equilibrium[36]. When the system is in this state the forward and reverse reactions are equal and opposite while the currents associated with these reactions are equal and opposite. Whenever a net current flows, this equilibrium state is broken and an irreversible process results. If the electrode process is rapid, or if the current is small enough, the departure from equilibrium will be small and the difference between the theoretical electrode potential and the potential when the current is flowing will also be small.

An electrode reaction is a heterogeneous process since it occurs across two phases[35]. Like homogeneous reactions, the reacting species taking part in electrode processes have to overcome an

energy barrier. Consider the following single step electrode reaction in reversible equilibrium,

$$O + Ze \underset{k_{-1}}{\overset{k_1}{\rightleftharpoons}} R \qquad (1)$$

where O is the species in the oxidized state and R in the reduced state. The reduction of O is represented by a movement from left to right over an energy peak shown in Fig. 2a. The entity at the peak is called an activated complex which has a structure intermediate between O and R. Thermodynamically, a free energy ΔG_1^* is required for the O species to surmount the barrier peak. This energy is called the free energy of activation. Correspondingly, there is a surmounting of the peak when R is oxidized to O. Similarly, a characteristic free energy of activation, ΔG_{-1}^*, is associated with the process. The difference between these two free energies of activation is the free energy of reaction, ΔG^*, which is related to the reversible electrode potential, ε_o, by the expression,

$$\Delta G^* = \Delta G_1^* - \Delta G_{-1}^* = - zF\varepsilon_o \qquad (2)$$

where F is the Faraday.

If the reversible equilibrium is maintained, the specific rate k_1 of the discharge of species O is

$$k_1 = \frac{kT}{h} \exp\left[-\frac{\Delta G_1^*}{RT}\right] \qquad (3)$$

and the specific rate of oxidation of R is

$$k_{-1} = \frac{kT}{h} \exp\left[\frac{-\Delta G_{-1}^*}{RT}\right] \qquad (4)$$

The actual rate of reaction is obtained by multiplying the specific rate by the activity of the reactant[36]. The standard state chosen

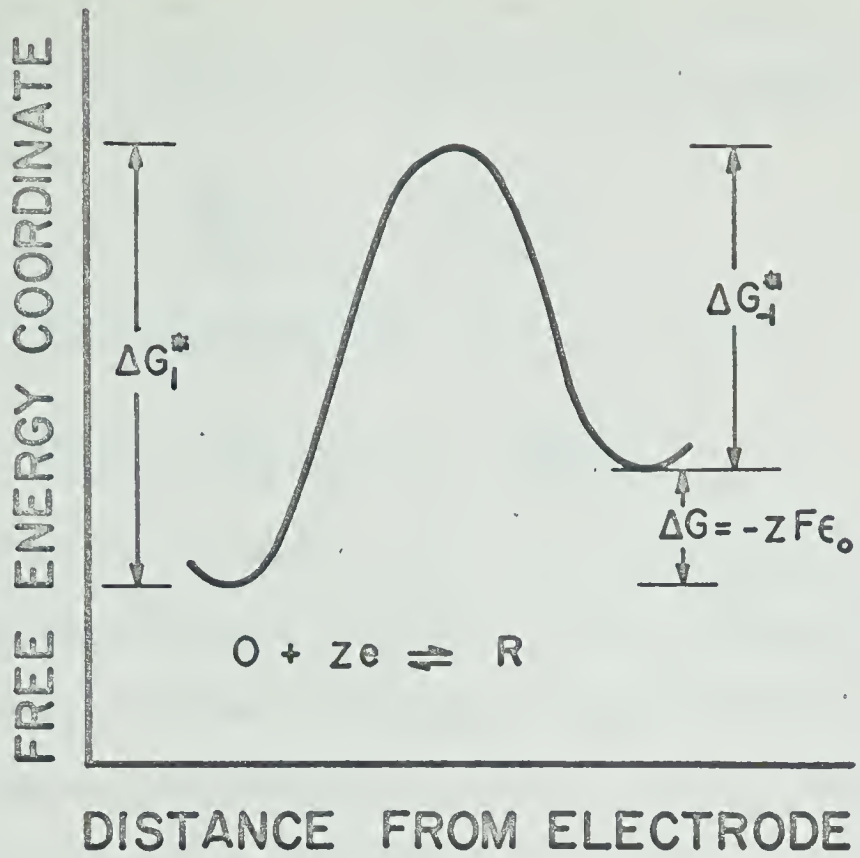

Fig. 2a. Activation Energy Curve
For a Reversible Electrode Process

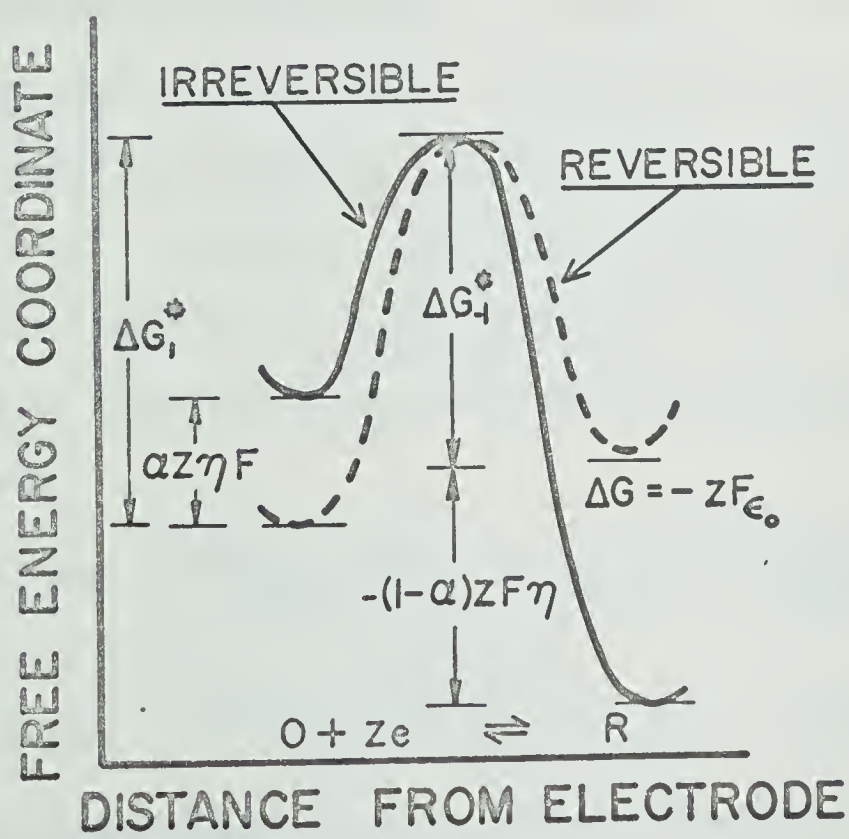

Fig. 2b. Activation Energy Curve For
an Irreversible Electrode Process

for the species is one of a hypothetical ideal solution at unit concentration. It follows that the rate of the forward reaction, v_1', is

$$v_1' = k_1 a_o = \frac{kT}{h} a_o \exp\left[\frac{-\Delta G_1^*}{RT}\right] \tag{5}$$

and similarly the rate of reverse reaction, v_{-1}', is

$$v_{-1}' = k_{-1} a_R = \frac{kT}{h} a_R \exp\left[\frac{-\Delta G_{-1}^*}{RT}\right] \tag{6}$$

If the reduction of 0 is made faster than the oxidation of R by applying a potential across the metal solution interface, a net reaction occurs. This new situation is depicted in Fig. 2b. The electrode potential under the irreversible condition departs from the equilibrium potential by an amount η, called the overpotential,

$$\eta = \varepsilon - \varepsilon_o \tag{7}$$

A fraction of the overpotential accelerates the reduction of 0 and the remainder retards the oxidation of R. Acceleration of the discharging process is accomplished by decreasing the free energy of activation from ΔG_1^* to $\Delta G_1^* + z\alpha F\eta$. Similarly, the oxidizing process is retarded by increasing the free energy of activation from ΔG_{-1}^* to $\Delta G_{-1}^* - z(1-\alpha)F\eta$. It should be noted that the overpotential, η, is negative in a reducing process. Then the electrochemical rates of reaction for the reduction and oxidation processes are respectively,

$$v_1 = \frac{kT}{h} a_o \exp\left[\frac{-\Delta G_1^* + z\alpha F\eta}{RT}\right] = k_1 a_o \exp\left[\frac{-z\alpha F\eta}{RT}\right] \tag{8}$$

and

$$v_1 = \frac{kT}{h} a_R \exp\left[\frac{-\Delta G_{-1}^* - z(1-\alpha)F\eta}{RT}\right] = k_{-1} a_R \exp\left[\frac{z(1-\alpha)F\eta}{RT}\right] \tag{9}$$

If the activity coefficients of species 0 and R are incorporated into

the specific rate constants, equations (8) and (9) respectively become functions of the concentrations of O and R,

$$v_1 = k_1 c_1 \exp\left[\frac{-z\alpha F\eta}{RT}\right] \tag{10}$$

$$v_{-1} = k_{-1} c_R \exp\left[\frac{z(1-\alpha)F\eta}{RT}\right] \tag{11}$$

Electrochemical rates of reaction are conveniently expressed in terms of current densities. If the units of the rates v_1 and v_{-1} are in grams per second per unit area of electrode surface, the rates v and the current density i is related by the expression

$$v = \frac{i}{zF} \tag{12}$$

Putting this identity into equations (10) and (11), the new rates of equations expressed in units of amperes per cm^2. are

$$i_1 = zFk_1 a_o \exp\left[\frac{-z\alpha F\eta}{RT}\right] \tag{13}$$

$$i_{-1} = zFk_{-1} a_R \exp\left[\frac{z(1-\alpha)F\eta}{RT}\right] \tag{14}$$

When the electrode potential reaches values near the reversible equilibrium potential, the reverse reaction can become kinetically significant; that is, the reverse rate cannot be neglected in the net cathodic rate i_c

$$i_c = i_1 - i_{-1} \tag{15}$$

$$i_c = zFk_1 a_o \exp\left[\frac{-z\alpha F\eta}{RT}\right] - zFk_{-1} a_R \exp\left[\frac{z(1-\alpha)F\eta}{RT}\right] \tag{16}$$

When the electrode is behaving reversibly, i.e. $\eta = o$, the situation arises

$$i_1 = i_{-1} = zFk_1 a_o = zFk_{-1} a_R \tag{17}$$

The exchange current density is thus defined as

$$i_o = zFk_1a_o = zFk_{-1}a_R \tag{18}$$

resulting in new expressions for equations (13), (14), and (16)

$$i_1 = i_o \exp\left[\frac{-z\alpha F\eta}{RT}\right] \tag{19}$$

$$i_{-1} = i_o \exp\left[\frac{z(1-\alpha)F\eta}{RT}\right] \tag{20}$$

$$i_c = i_o\left(\exp\left[\frac{-z\alpha F\eta}{RT}\right] - \exp\left[\frac{z(1-\alpha)F\eta}{RT}\right]\right) \tag{21}$$

Under highly irreversible conditions, rates i_1 and i_c are identical

$$i_c = i_1 = i_o \exp\left[\frac{-z\alpha F\eta}{RT}\right] \tag{22}$$

The following equation results upon taking the logarithm of (22)

$$\log i_c = \log i_o + \frac{-z\alpha F\eta}{RT} \tag{23}$$

Rearranging, the usual Tafel equation is obtained

$$\eta = \frac{2.303\ RT}{z\alpha F} \log i_o + \frac{-2.303\ RT}{z\alpha F} \log i_c \tag{24}$$

$$= a + b \log i_c \tag{25}$$

where

$$a = \frac{2.303\ RT}{z\alpha F} \log i_o \text{ and } b = \frac{-2.303\ RT}{z\alpha F} \tag{26}$$

The Tafel parameter "a" is the overpotential at $i_c = 1$ amp./cm.^{2} and b is the Tofel slope when η is plotted against $\log i_c$. Parameters "a" and "b", and i_o are very necessary in the elucidation of the mechanism of electrode processes.

Transfer Coefficient (α)

The constant α used in the previous equations has been named

transfer coefficient[34]. In the rate equations α is " a priori" considered strictly as a parameter introduced to fit experimental data. As such, with $\alpha = 1/2$ a large number of electrode kinetic rate equations may be represented with fair accuracy.

The electrostatic part of the Gibb's free energy of an individual ion in a field generated by a large number of other identical point charges, cannot be determined separately, but only in conjunction with an opposite counter charge. In the electrical double layer the positive ions on the solution side must be considered jointly with the opposite negative charges on the electrode. The electrostatic energy of each charge pair may be obtained by a charging process as used in determining the electrostatic energy of electric condensers. Applying this principle, the electrostatic potential energy of the reacting species in the interface depends on the potential across the double layer

$$\Delta G = 1/2\ z_i F\eta \tag{27}$$

Hence, the transfer coefficient is derived to be $\alpha = 1/2$.

A synonomous term very often used in the symmetry factor β[38]. This is the ratio of the gradients of the potential-energy distance relation of the initial and final states,

$$\beta = \frac{m_1}{m_1+m_2}$$

where m_1 is the slope of the initial state and m_2 the slope of the final state.

Stoichiometric Number

The stoichiometric number is the number of acts of the rate-determining step accompanying one act of the over-all reaction[38]. Its derivation is given by Bockris who considered the general reaction of the form

$$xX + bB^{z} + ne \rightarrow wW + cC^{\frac{bz-n}{c}} \tag{28}$$

The rate-determining step corresponding to it is given by

$$\frac{xX}{\nu} + \frac{bB^{z}}{\nu} + \frac{ne}{\nu} \rightarrow \frac{wW}{\nu} + \frac{cC^{\frac{bz-n}{c}}}{\nu} \tag{29}$$

where ν is the stoichiometric number. The electrochemical potentials of the activated state and that for the initial state is

$$\bar{\mu}_A^{o\ddagger} - \mu_A^{o\ddagger} - \bar{\mu}_P^{o} = (\bar{\mu}_Q^{o} - \mu_Q^{o}) - (\bar{\mu}_P^{o} - \mu_P^{o}) \tag{30}$$

where P and Q are the states just before and just after the rate-determining step, $A^{\ddagger}$ is the activated complex, and $\bar{\mu}$ and μ are the electrochemical and chemical potentials, respectively. The rate constants for the forward and reverse reactions are

$$\vec{k} = \frac{kT}{h} \exp\left[\frac{-\Delta\vec{G}^{\ddagger} + (1-\beta)_P + \beta_P + \frac{n\beta F\eta}{\nu}}{RT}\right] \tag{31}$$

and $$\overleftarrow{k} = \frac{kT}{h} \exp\left[\frac{-\Delta\overleftarrow{G}^{\ddagger} + (1-\alpha)_P + \alpha_P - (1-\beta)\frac{nF\eta}{\nu}}{RT}\right] \tag{32}$$

The rates of forward and reverse reactions are given by

$$\vec{i} = \frac{n}{\nu} F \vec{k} a_X^{x^1} a_B^{b^1} \text{ and } \overleftarrow{i} = \frac{n}{\nu} F k a_W^{w^1} a_C^{c^1} \tag{33}$$

The net cathodic rate is then

$$i_c = \vec{i} - \overleftarrow{i} = i_o \left\{\exp\left[\frac{-(\beta+\gamma)F\eta}{\nu RT}\right] - \exp\left[\frac{(1-\beta-\gamma)F\eta}{\nu RT}\right]\right\} \tag{34}$$

At low overpotentials the exponentials can be expanded, which led to the evaluation of the stoichiometric number

$$\nu = \frac{-nFi_o}{RT}\left(\frac{\partial\eta}{\partial i}\right)_{\eta\to o} \tag{35}$$

Hydrogen Evolution Reaction in Alkaline Media

The hydrogen evolution reaction in aqueous media is a consecutive reaction in which reaction intermediates are involved. In these consecutive reactions, it is always the step with the smallest rate constant which controls the rate, that is, the step involving the highest energy barrier. The steady state of an electrochemical reaction is reached when the concentration of the reaction intermediate on the electrode surface remains constant.

The h.e.r. involves the discharge of hydronium ions at the electrode-solution interface in acid media. It is generally recognized, however, that water molecules are the species being discharged in neutral or alkaline solutions[39, 40].

The standard heat content change accompanying the reaction

$$H_3O^+ + e \text{ (in metal)} \rightarrow H_{ads.} \tag{36}$$

may be written

$$\Delta H_1 = (H_H)_1 - H_{H_3O^+} - H_e \tag{37}$$

where the H's are the standard heat contents[39]. Similarly, for the reaction

$$H_2O + e \text{ (in metal)} \rightarrow H_{ads.} + OH^- \tag{38}$$

the accompanying heat content change is

$$\Delta H_2 = (H_H)_2 + H_{OH^-} - H_{H_2O} - H_e \qquad (39)$$

Subtracting (37) from (39) the following comparison is obtained

$$\Delta H_2 - \Delta H_1 = (H_H)_2 - (H_H)_1 + H_{H^+} + H_{OH^-} - H_{H_2O} \qquad (40)$$

The heat of dissociation of water into its ions, $H_{H^+} + H_{OH^-} - H_{H_2O}$, is about 13.6 kcal. per mole. The difference of the standard heat content of the adsorbed H in the two reactions arises from the different interaction energies between H and H_2O and between H and OH^-. Calculations showed that $(H_H)_2 - (H_H)_1$ is very small and positive. Hence, $\Delta H_2 - \Delta H_1$ is very close to 14 kcal./mole. The potential energy curve for reaction (39) is, therefore, similar to that for reaction (37) with the initial state lowered by 14 kcal./mole. Since the slopes of the initial and final state curves are approximately equal this change would result in an increase in the activation energy of about 7 kcal./mole. However, the potential energy curves are also different in shape. The OH^- ion is larger than the water molecule by about 0.1 A° and as a result of this the curve for the final state is steeper than that for reaction (37). Similarly, the initial state curve is steeper for reaction (39) than for reaction (37) because the force constant of the O-H bond in the water molecule is larger than that of the O-H bond in the hydronium ion. Consequently, the activation energy of reaction (39) is greater than that of reaction (37) by more than 7 kcal./mole. Therefore, the total increase of activation energy for reaction (39) is close to 14 kcal./mole.

In alkaline solutions, the concentration of water molecules is about 10^{14} times greater than that of hydronium ions and both the

discharge of protons and water molecules may be energetically possible. Under these conditions the reduction of water molecules is however much more probable as the supply of hydronium to the electrode surface from the bulk of the solution is not fast enough. On the other hand, the concentration of water molecules in acid solutions is only a few powers of ten greater than hydronium ions; hence, the discharge of water molecules is improbable unless there is a large difference in the entropy of activation for the two reactions.

Mechanisms of H.E.R. in Alkaline Solutions

With the exception of mercury and its amalgam electrodes, there are four possible mechanisms for the electrolytic evolution of hydrogen in alkaline or neutral solutions[38]:

(A) $H_2O + M + e \underset{-1}{\overset{1}{\rightleftharpoons}} M - H + OH^-$ (rate-controlling) (41)

$M - H + M - H \xrightarrow{2} H_2 + 2M$ (fast) (42)

(B) $H_2O + M + e \underset{-1}{\overset{1}{\rightleftharpoons}} M - H + OH^-$ (fast) (41)

$M - H + M - H \xrightarrow{2} H_2 + 2M$ (rate-controlling) (42)

(C) $H_2O + M + e \underset{-1}{\overset{1}{\rightleftharpoons}} M - H + OH^-$ (rate-controlling) (41)

$H_2O + M - H + e \xrightarrow{3} H_2 + M + OH^-$ (fast) (43)

(D) $H_2O + M + e \underset{-1}{\overset{1}{\rightleftharpoons}} M - H + OH^-$ (fast) (41)

$H_2O + M - H + e \xrightarrow{3} H_2 + M + OH^-$ (rate-controlling) (43)

Three rate-controlling reactions are possible: (i) the discharge of a water molecule onto a metal site M to form a reaction intermediate M-H, equation (41); (ii) the recombination of two atomic hydrogens to form a molecular H_2, equation (42); and (iii) the electrochemical desorption, equation (43).

The kinetics may be complicated by the presence of: (i) simultaneous reactions in which two desorptive reactions proceed at the same or near the same velocity in the steady state; (ii) dual reactions in which two steps in the mechanism have virtually the same energy barrier; and (iii) linked reactions, where the energy barrier of various steps are of appreciable different heights, but the kinetics of the overall process depend upon the heights of two or more energy barriers.

Steady-State Kinetic Equations

The kinetic equations can be elucidated by applying the steady state theory which states that in the state of steady current, the surface concentration of adsorbed atomic hydrogen remains constant[12],

$$\frac{d\theta}{dt} = 0 \qquad (44)$$

In the present derivations, it will be assumed that the adsorption of hydrogen upon the electrode is governed by a Langmuir isotherm and that the rates of the reverse desorption reactions may be neglected at potentials not near the reversible hydrogen potential. Furthermore, the double layer effects are assumed constant in concentrated salt solutions.

(1) Mechanism (A): Slow Discharge - Fast Recombination.

Assuming the activity of water at the electrode surface is

the same as that in the bulk solution, it follows,

$$v_1 = k_1(1-\theta) \exp \left[\frac{-z\alpha F\eta}{RT}\right] \tag{45}$$

$$v_{-1} = k_{-1}\theta a_{OH^-} \exp \left[\frac{z(1-\alpha)F\eta}{RT}\right] \tag{46}$$

and

$$v_2 = k_2\theta^2 \tag{47}$$

In the steady state

$$\frac{d\theta}{dt} = v_1 - v_{-1} - 2v_2 = 0 \tag{48}$$

Substituting (45), (46), and (47) into (48) results

$$k_1(1-\theta) \exp \left[\frac{-z\alpha F\eta}{RT}\right] - k_{-1}\theta a_{OH^-} \exp \left[\frac{z(1-\alpha)F\eta}{RT}\right] - 2k_2\theta^2 = 0 \tag{49}$$

For slow discharge - fast recombination mechanism to prevail, $k_2 >> k_1, k_{-1}$, equation (49) becomes

$$k_1 \exp \left[\frac{-z\alpha F\eta}{RT}\right] - 2k_2\theta^2 = 0 \tag{50}$$

From which, the fraction of electrode surface covered with atomic hydrogen is

$$\theta = \left(\frac{k_1}{2k_2}\right)^{1/2} \exp \left[\frac{-z\alpha F\eta}{2RT}\right] \tag{51}$$

Since the combination of atomic hydrogen is desorptive, application of equation (12) leads to the cathodic rate (this is not the rate controlling step but must have a rate equal to it)

$$i_c = nFv_2 = 2Fk_2\theta^2 \tag{52}$$

$$= 2Fk_2 \left\{ \left(\frac{k_1}{2k_2} \right)^{1/2} \exp \left[\frac{-z\alpha F\eta}{2RT} \right] \right\}^2 \tag{53}$$

$$= Fk_1 \exp \left[\frac{-z\alpha F\eta}{RT} \right] \tag{54}$$

Upon taking the logarithm and rearranging the Tafel equation is obtained for this mechanism

$$\eta = \frac{2.303\ RT}{z\alpha F} \log Fk_1 - \frac{2.303\ RT}{z\alpha F} \log i_c \tag{55}$$

$$\eta = a + b \log i_c \tag{56}$$

Experimentally, a plot of η vs $\log i_c$ should yield a straight line with slope

$$\frac{\partial \eta}{\partial \log i_c} = b = \frac{-2.303\ RT}{z\alpha F} \tag{57}$$

and with intercept

$$a = \frac{2.303\ RT}{z\alpha F} \log Fk_1 \tag{58}$$

If $T = 35°$ C, $\alpha = 1/2$, and $z = 1$, the theoretical Tafel slope is -122 mv. Since the rate-controlling step occurs twice when the overall reaction occurs once[38], the stoichiometric number for the mechanism is 2.

(2) Mechanism (B): Fast Discharge - Slow Recombination

For this mechanism, the same equations (45) - (49) hold. However, the condition is $k_1, k_{-1} >> k_2$, so that (49) reduces to

$$k_1(1-\theta) \exp \left[\frac{-z\alpha F\eta}{RT} \right] - k_{-1}\theta a_{OH^-} \exp \left[\frac{z(1-\alpha)F\eta}{RT} \right] = 0 \tag{59}$$

Rearranging,

$$k_1\theta \exp \left[\frac{-z\alpha F\eta}{RT} \right] + k_{-1}\theta a_{OH^-} \exp \left[\frac{z(1-\alpha)F\eta}{RT} \right] = k_1 \exp \left[\frac{-z\alpha F\eta}{RT} \right] \tag{60}$$

It follows that

$$\theta = \frac{k_1 \exp\left[\frac{-z\alpha F\eta}{RT}\right]}{k_1 \exp\left[\frac{-z\alpha F\eta}{RT}\right] + k_{-1}a_{OH^-} \exp\left[\frac{z(1-\alpha)F\eta}{RT}\right]} \tag{61}$$

Two limit cases are possible as $\frac{k_{-1}}{k_1}$ is constant for a given electrode of constant surface properties:

(i) At small negative values of η and low concentration of M - H, for example, $k_{-1}a_{OH^-} \exp \frac{z(1-\alpha)F\eta}{RT} > 10k_1 \exp \frac{-z\alpha F\eta}{RT}$, equation (61) becomes

$$\theta = \frac{k_1 \exp\left[\frac{-z\alpha F\eta}{RT}\right]}{k_{-1}a_{OH^-} \exp\left[\frac{z(1-\alpha)F}{RT}\right]} \tag{62}$$

$$= \frac{k_1}{k_{-1}a_{OH^-}} \exp\left[\frac{-zF\eta}{RT}\right] \tag{63}$$

Putting (63) into (52) the rate equation is

$$i_c = 2Fv_2 = 2Fk_2\theta^2 = 2Fk_2\left(\frac{k_1}{k_{-1}a_{OH^-}}\right)^2 \exp\left[\frac{-2zF\eta}{RT}\right] \tag{64}$$

The following Tafel relationship is obtained after taking the logarithm and rearranging the preceding expression

$$\eta = \frac{2.303\ RT}{2zF} \log 2Fk_2\left(\frac{k_1}{k_{-1}a_{OH^-}}\right)^2 - \frac{2.303\ RT}{2zF} \log i_c \tag{65}$$

where the Tafel slope is

$$\frac{\partial\eta}{\partial \log i_c} = b = -\frac{2.303\ RT}{2zF} \tag{66}$$

and the intercept is

$$a = \frac{2.303\ RT}{2zF} \log 2Fk_2\left(\frac{k_1}{k_{-1}a_{OH^-}}\right)^2 \tag{67}$$

Putting T = 35°C and z = 1, the theoretical Tafel slope is -30 mv.

(ii) At high negative values of η and high concentrations of M - H, then $k_1 \exp \frac{-z\alpha F\eta}{RT} >> k_{-1} a_{OH^-} \exp \frac{z(1-\alpha)F\eta}{RT}$ such that (63) becomes

$$\theta = \frac{k_1 \exp \left[\frac{-z\alpha F\eta}{RT}\right]}{k_1 \exp \left[\frac{-z\alpha F\eta}{RT}\right]} = 1 \tag{68}$$

The corresponding rate equation is

$$i_c = 2Fv_2 = 2Fk_2\theta^2 = 2Fk_2 \tag{69}$$

which shows that the current is independent of the overpotential indicating a limiting current at unit coverage.

(3) Mechanism (C): Slow Discharge - Fast Electrochemical

The corresponding rate equations are:

$$v_1 = k_1(1-\theta) \exp \left[\frac{-z\alpha F\eta}{RT}\right] \tag{45}$$

$$v_{-1} = k_{-1}\theta a_{OH^-} \exp \left[\frac{z(1-\alpha)F\eta}{RT}\right] \tag{46}$$

and

$$v_3 = k_3\theta \exp \left[\frac{-z\alpha F\eta}{RT}\right] \tag{70}$$

Under steady-state conditions

$$\frac{d\theta}{dt} = k_1(1-\theta) \exp \left[\frac{-z\alpha F\eta}{RT}\right] - k_{-1}\theta a_{OH^-} \exp \left[\frac{z(1-\alpha)F\eta}{RT}\right] - k_3\theta \exp \left[\frac{-z\alpha F\eta}{RT}\right] = 0 \tag{71}$$

The condition for this mechanism is $k_3 >> k_1, k_{-1}$, then (71) becomes

$$k_1 \exp \left[\frac{-z\alpha F\eta}{RT}\right] - k_3\theta \exp \left[\frac{-z\alpha F\eta}{RT}\right] = 0 \tag{72}$$

It can then be shown by rearrangement that

$$\theta = \frac{k_1}{k_3} \tag{73}$$

Since equation (43) is desorptive, the rate equation is

$$i_c = zFv_3 = zFk_3\theta \exp\left[\frac{-z\alpha F\eta}{RT}\right] \tag{74}$$

$$= zFk_3 \frac{k_1}{k_3} \exp\left[\frac{-z\alpha F\eta}{RT}\right] \tag{75}$$

$$= zFk_1 \exp\left[\frac{-z\alpha F\eta}{RT}\right] \tag{76}$$

The Tafel equation is then shown to be

$$\eta = \frac{2.303\ RT}{z\alpha F} \log zFk_1 - \frac{2.303\ RT}{z\alpha F} \log i_c \tag{77}$$

$$= a + b \log i_c$$

where

$$a = \frac{2.303\ RT}{z\alpha F} \log zFk_1 \quad \text{and } b = \frac{-2.303\ RT}{z\alpha F} \tag{78}$$

If T = 35°C, = 1/2, and z = 1, the Tafel slope value is -122 mv.

(4) Mechanism (D): Fast Discharge - Slow Electrochemical

If the mechanism is fast discharge of a water molecule followed by rate-controlling electrochemical desorption, the rate equations (45), (46), (70), and (71) hold except that two conditions are possible: (i) If η is low then necessarily θ is low. As such $k_{-1} >> k_1, k_3$. It then follows that (71) becomes

$$k_1 \exp\left[\frac{-z\alpha F\eta}{RT}\right] - k_{-1}\theta a_{OH^-} \exp\left[\frac{z(1-\alpha)F\eta}{RT}\right] = 0 \tag{79}$$

Rearranging, an expression for θ is obtained

$$\theta = \frac{k_1 \exp\left[\frac{-z\alpha F\eta}{RT}\right]}{k_{-1}a_{OH^-} \exp\left[\frac{z(1-\alpha)F\eta}{RT}\right]} \tag{80}$$

which reduces to

$$\theta = \frac{k_1}{k_{-1}a_{OH^-}} \exp\left[\frac{-zF\eta}{RT}\right] \tag{81}$$

The cathodic rate is then

$$i_c = zFv_3 = zFk_3\theta \exp\left[\frac{-z\alpha F\eta}{RT}\right] = zF\frac{k_1k_3}{k_{-1}a_{OH^-}} \exp\left[\frac{-z(1+\alpha)F\eta}{RT}\right] \tag{82}$$

Upon taking the logarithm and rearranging the usual Tafel expression for the present mechanism is

$$\eta = \frac{2.303\ RT}{z(1+\alpha)F} \log zF\frac{k_1k_3}{k_{-1}a_{OH^-}} - \frac{2.303\ RT}{z(1+\alpha)F} \log i_c \tag{83}$$

Using the same values for T, α, and z, the Tafel slope is calculated to be -40 mv.

(ii) If $k_1 >> k_{-1}, k_3$, equation (71) becomes

$$k_1(1-\theta) \exp\left[\frac{-z\alpha F\eta}{RT}\right] = 0 \tag{84}$$

It then follows that $\theta_H = 1$. Then the rate equation is

$$i_c = zFv_3 = zFk_3\theta \exp\left[\frac{-z\alpha F\eta}{RT}\right] \tag{85}$$

$$= zFk_3 \exp\left[\frac{-z\alpha F\eta}{RT}\right] \tag{86}$$

The corresponding η- log i_c relationship is

$$\eta = \frac{2.303\ RT}{z\alpha F} \log zFk_3 - \frac{2.303\ RT}{z\alpha F} \log i_c \tag{87}$$

$$= a + b \log i_c$$

where

$$a = \frac{2.303\ RT}{z\alpha F} \log zFk_3, \text{ and } b = \frac{-2.303\ RT}{z\alpha F} \tag{88}$$

The Tafel slope can be shown to be -122 mv.

Experimental Considerations to the Elucidation of Mechanism

Table I shows a list of diagnostic criteria for elucidating the mechanisms of the cathodic hydrogen evolution reaction. The mechanism is uniquely determined if the Tafel slope b and the stoichiometric number are known. Values of quoted b involved the assumption that $\alpha = 1/2$. The determination of ν is unnecessary if b is found to be -30 or -40 mv. If the hydrogen overpotential is high, then ν is not determinable. The mechanism would then have to be elucidated by determining the concentration of adsorbed atomic hydrogen.

TABLE I

Table of Diagnostic Criteria*

	Mechanism	$b = \frac{\partial \eta}{\partial \log i_c}$, mv.	ν	$\frac{\partial \eta}{\partial \log \theta}$, mv.
(A)	$H_2O+M+e \underset{}{\overset{slow}{\rightleftharpoons}} M\text{-}H+OH^-$ $M\text{-}H+M\text{-}H \xrightarrow{fast} H_2+2M$	-122	2	-244
(B)	$H_2O+M+e \overset{fast}{\rightleftharpoons} M\text{-}H+OH^-$ $M\text{-}H+M\text{-}H \xrightarrow{slow} H_2+2M$	-30; ∞	1	-60; ∞
(C)	$H_2O+M+e \overset{slow}{\rightleftharpoons} M\text{-}H+OH^-$ $H_2O+M\text{-}H+e \xrightarrow{fast} H_2+OH^-+M$	-122	1	0
(D)	$H_2O+M+e \overset{fast}{\rightleftharpoons} M\text{-}H+OH^-$ $H_2O+M\text{-}H+e \xrightarrow{slow} H_2+OH^-+M$	-40; -122	1	-60; ∞

* b - Tafel slope, ν - stoichiometric number

EXPERIMENTAL

Assembly of Electrodes

Polarizing Electrode: Commercial stainless steel type 304 rods supplied by Atlas Steel Company were used. A small piece of a rod was tapped, threaded, and attached to a steel rod to serve as the electrical lead. The stainless steel end of the rod was forced into a hole in a small piece of Teflon rod. A thick-walled glass tube fitted over the Teflon isolated the polarizing electrode from the electrolytic solution. The other end of the glass rod was fused onto the plunger of a 20 c.c. Luer syringe so that the electrode could be raised from or lowered into the electrolyte. With the aid of a Teflon ring, brass cap, and a nut over the glass tube the electrode was made leakproof. A 24/40 ground glass joint was welded to the barrel of the syringe to insert the electrode into the cell[41]. Two separate flat electrodes of surface areas 0.44 and 0.23 cm^2 were obtained by machining.

For high current density studies heat drawn stainless steel type 304 wire of 1/16 inch diameter was forced through a Teflon spaughetti. An area of 0.02 cm^2 was obtained.

Counter Electrode: A bright platinum sheet of 3 cm^2 was employed. About half of the sheet was coated with platinum black to give a larger surface. The platinizing solution was prepared by dissolving 3 grams of platinic acid and 200 mg. of lead acetate in 100 ml. conductivity water. A current density of 250 ma/cm^2 was employed for the electrodeposition.

Reference Electrodes: Half-cells of HgO/Hg in 0.1, 1.0, 3.0, 5.0, and 10 M NaOH solution were prepared according to Ives and Janz[42].

Mercuric oxide, liquid Hg, and electrolyte were mortared to a thick paste. A thin layer of the paste was laid on top of a mercury pool in contact with a solution of NaOH. Electrical contact was made by means of a Pt wire.

Electrolytic Cell

An all glass cell was employed consisting of three compartments--reference (R.E.), counter (C.E.), and working (W.E.). A Luggin capillary bridged the R.E. and W.E. compartments. The C.E. compartment was separated from the W.E. compartment by a fine sintered disk. Ground glass joints were glass blown onto the R.E. and C.E. compartments to accommodate the reference and counter electrodes. To prevent any significant bulk concentration changes, the capacity of the W.E. compartment was made to be about 600 ml. An inner 71/60 ground glass joint was fused to the large chamber which was fitted with an outer 71/60 ground glass joint cap for isolation from the atmosphere. Smaller joints were fused onto the cap so that the thermometer, working electrode, gas outlet, and pre-electrolysis electrode could be inserted. Further atmospheric isolation of the W.E. chamber was obtained by filling the gas outlet with conductivity water. A gas dispersion tube was also installed to the center compartment for bubbling He or H_2 gas through the solution.

Preparation of Solutions

Reagent grades of NaOH, NaCl, NaI, NaF, $NaIO_3$, $LaCl_3$, $BaCl_2$, $NiCl_2$, $Fe_2(SO_4)_3$, and other auxiliary chemicals were weighed gravimetrically and dissolved in conductivity water. Chromic-sulfuric acid bath cleaned volumetric flasks were employed.

Experimental Procedures

The stainless steel type 304 electrodes were abraded with 4/0 emery paper. The electrolytic cell, polarizing electrode, counter electrode, pre-electrolysis electrode, thermometer, and Teflon-coated stirring bar were cleaned by immersing in chromic-sulfuric acid solution for 4-24 hours and then by washing thoroughly with distilled water and finally with conductivity water. Grade A helium gas was bubbled through the electrolyte during the 14-20 hour pre-electrolysis period which had a cathodic current density of about 1 ma/cm^2. The polarizing electrodes were made anodic for 5 minutes at 0.1 ma/cm^2 to dissolve any impurities from the electrode surface. A cathodic current density of about 12 ma/cm^2 was employed for 5 minutes to activate the electrodes before overpotential measurements were taken. Vigorous stirring via a magnetic stirrer was employed during the runs to eliminate concentration overpotentials.

Methods of Measurement

Luggin Capillary: The most common method of obtaining electrode potential near-free of ohmic polarization is by the Luggin capillary. In this method the working electrode compartment is connected to the reference electrode compartment via a salt bridge which is drawn out to a fine capillary near the polarizing electrode. Usually the capillary tip of outer diameter d may be placed as close as 2d from the electrode surface for negligible shielding error. The capillary will not measure directly the desired potential in the solution immediately adjacent to the electrode surface, but will measure the one at some distance δ from the surface. This is a

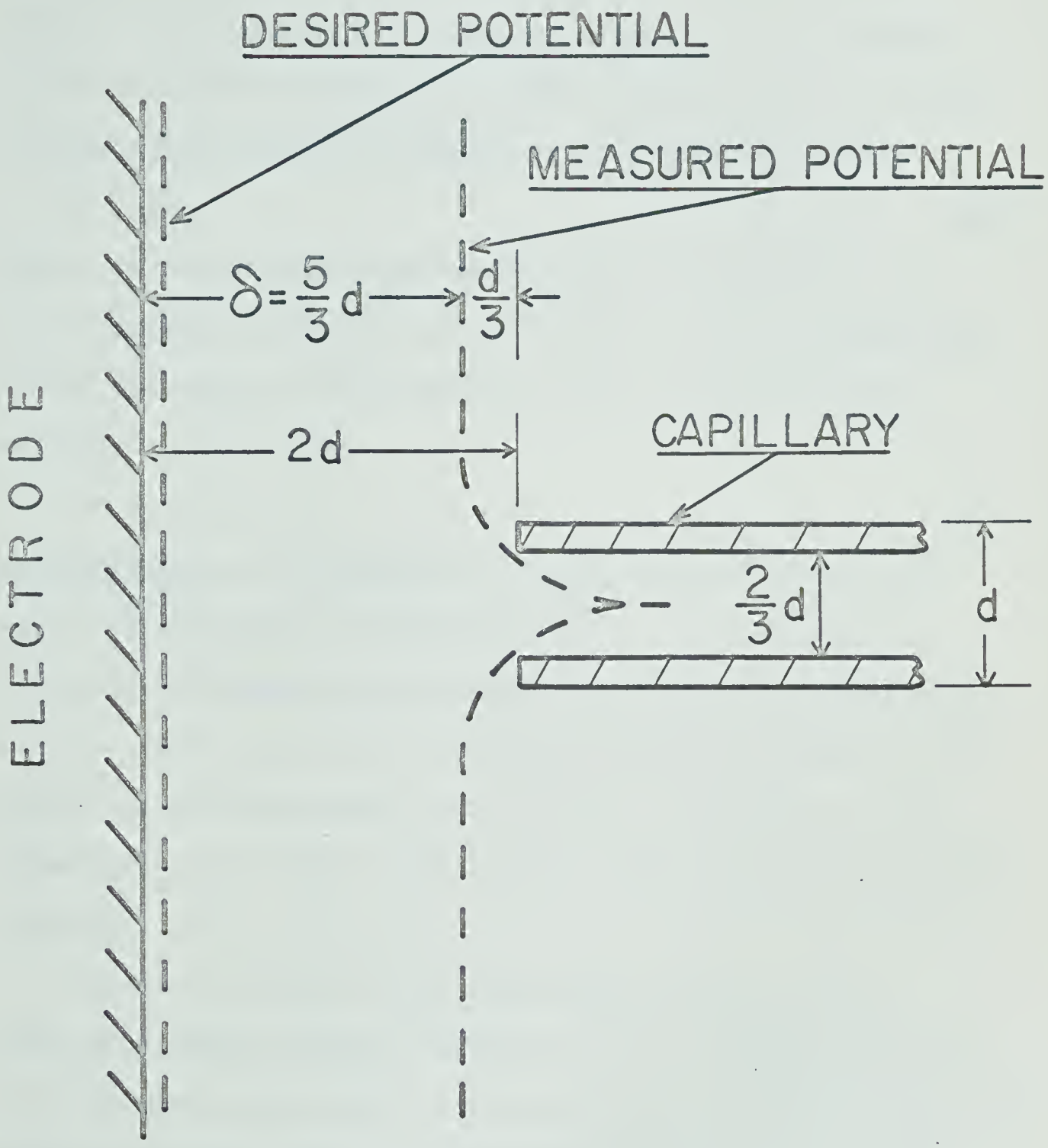

Fig. 3. Illustration of Ohmic Potential Drop

result of polarization measurements which are made while current is passing. Barnartt[43] emphasized that the difference in these two potentials represents an error as illustrated in Fig. 3. At a distance 2d he found that the measured potential is at a distance $\delta = 5/3$ d from the electrode. The ohmic potential drop, ηr between the Luggin capillary and the polarizing electrode is given by

$$\eta r = \frac{i\delta}{\kappa} \tag{89}$$

where κ is the specific conductance of the electrolyte and i the current passing through the cell. As such the ohmic potential drop must be subtracted from the measured value to obtain the true activation overpotential

$$\eta = \varepsilon_m - \eta r \tag{90}$$

<u>DC Interruption</u>: The elimination of ohmic potential drop by the Luggin capillary has two disadvantages[35]: (i) the method of correction is tedious and sometimes involves the uncertain assumption that the conductivity of the electrolyte near the electrode is the same as the solution conductivity; and (ii) in solutions of low conductivity or at high current densities large corrections are often necessary.

In order to overcome these disadvantages the d-c current interruptor method is used in conjunction with the Luggin capillary. The interruptor method exploits the fact that the resistive polarization decays or builds up almost instantaneously whereas activation and double layer charging take an appreciable time[35]. The detailed separation of the resistive, double layer charging and activation components will be shown later. The present measurements employed an electrolysis circuit with electronic current interruptor as

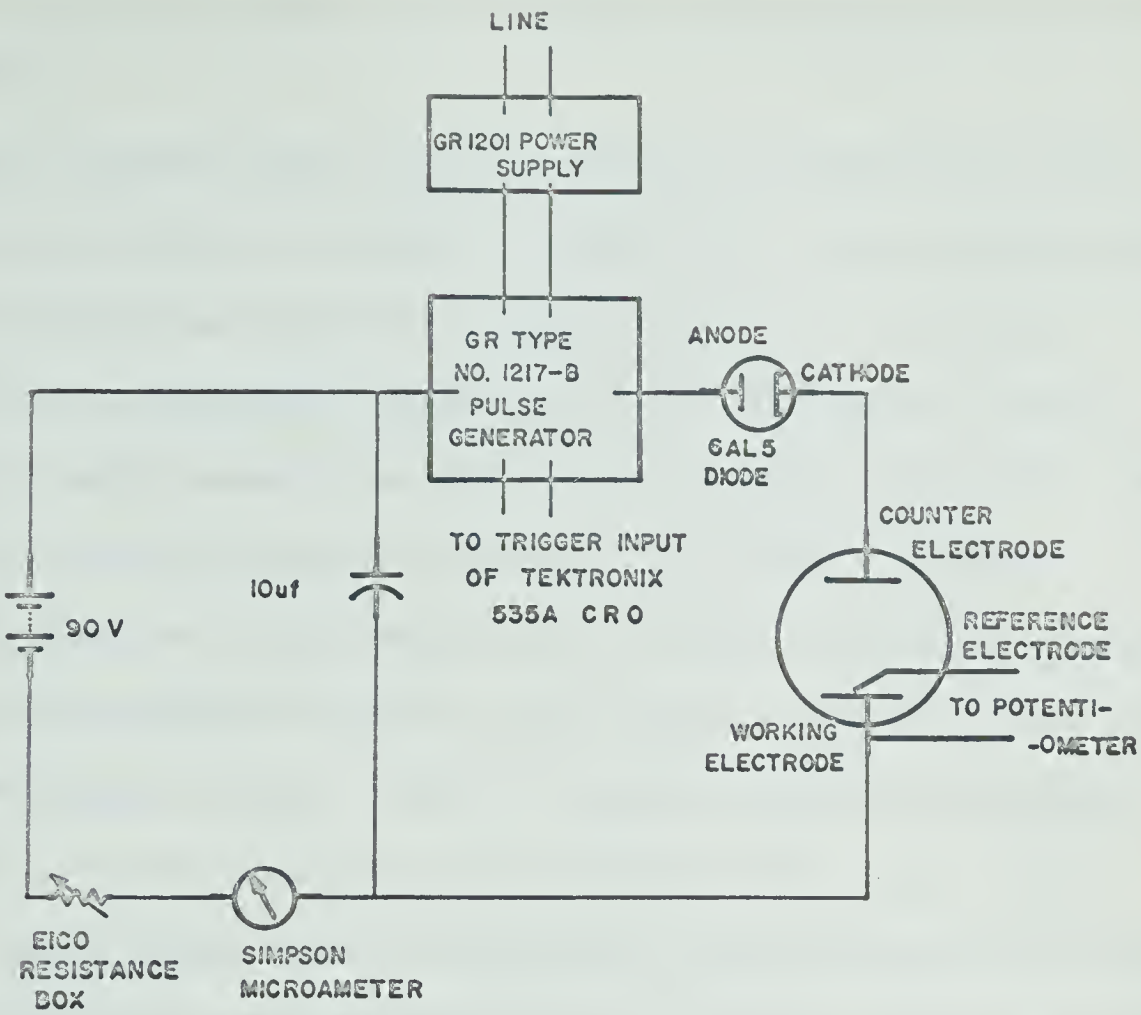

Fig. 4a. DC Interruption Electrical Polarization Circuit

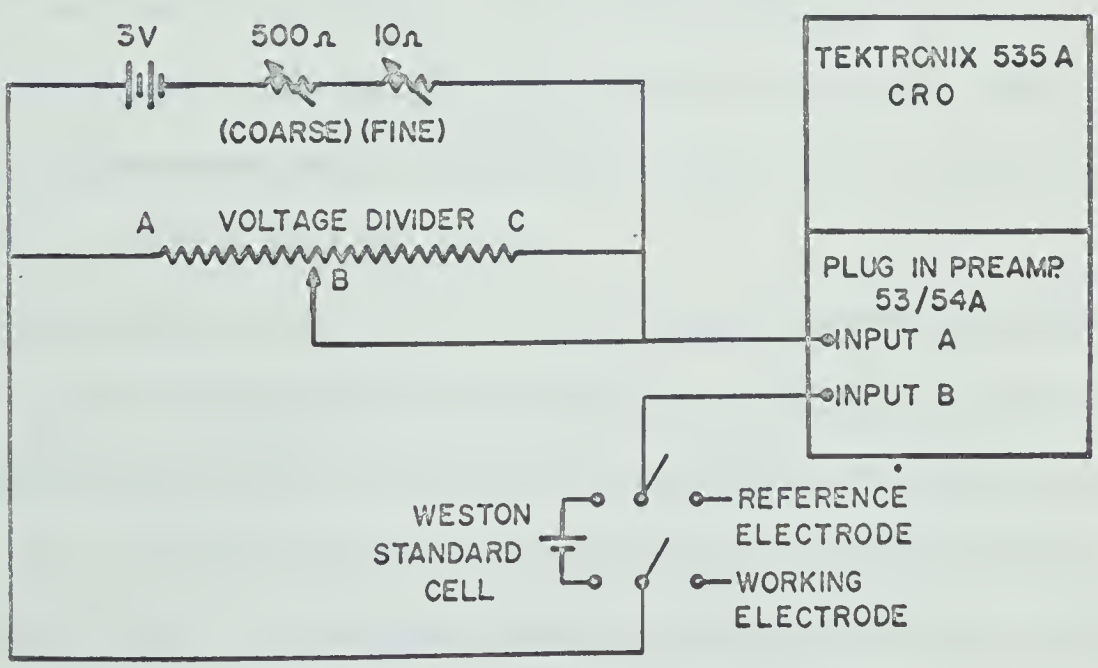

Fig. 4b. Cathode Ray Oscilloscope Measuring Circuit

shown in Fig. 4a, which is quite similar to that employed by Hoey and Cohen[44].

The stainless steel type 304 electrode was polarized via the counter electrode by a constant current source. As usual this constant current source was composed of a high capacity 90 v. dry cell battery and a resistance box giving a high resistance. A pulse generator and a vacuum diode were inserted between the current source and the electrolytic cell to interrupt the current. Negative current pulses of 22 monosecond rise time were supplied by a General Radio Pulse Generator Type No. 1217-B which was powered by its analogous GR Power Supply Type No. 1201-B. The pulse repetition frequency (PRF) and the pulse duration were adjusted to 100 c.p.s. and 100 μsec, respectively. Current interruption was obtained by adjusting the amplitude of the negative pulses to a slightly larger value than current supplied by the battery source. The 6AL5 vacuum diode did not conduct during the time of each negative pulse. As a result, for each 10 msec. period, the current flowed in the circuit for 9.9 msec. and the electrolysis current was interrupted for 0.1 msec. (100 μsec.). The polarizing current was measured with a Simpson's microammeter while any noise in the circuit was filtered by the 10 μf electrolytic capacitor.

The switching on and off of the polarizing current resulted in a build up and a decay of the electrode potential which was monitored by a Tektronix Type 535 A cathode ray oscilloscope (C.R.O.) as shown in Fig. 4b. By synchronizing the interruption rate with the time base of the C.R.O., a stationary trace was obtained on the oscilloscope screen. The signals were amplified with a Tektronix Type D pre-amplifier. It should be noted that the oscilloscope took the place

of the galvanometer in the usual potentiometer circuit. After a 15-20 minute warm up and with no input, the oscilloscope, whose sensitivity was adjusted to 5 mv./cm., was zeroed by adjusting the trace to the center of the C.R.O. graticule. Then the potentiometer circuit was connected to Inputs A and B of the preamplifier. With the double pole double throw (DPDT) switch at the standard cell terminals, the voltage divider was set at 1.0190 v., the potential of the Weston standard cell. Standardization was completed by adjusting the "COARSE" and the "FINE" heliopots until the C.R.O. trace was centered. To measure the polarizing potential, the DPDT switch was flipped to the REFERENCE-WORKING terminals of the potentiometer box.

Galvanostatic Stripping: This method involves the charging of the polarizing electrode by a large constant anodic current following cathodic polarization to determine the surface concentration of adsorbed atomic hydrogen[45].

An electrical circuit similar to that of Devanathan et al[46] was employed. As shown in Fig. 5, a constant current source was used to cathodically polarize the test electrode via the bright platinum counter electrode. Steady-state cathodic potentials were taken with a Keithley 660 differential vacuum tube voltmeter while polarizing currents were read from a Simpson's microammeter. The cathodic current was cut off and simultaneously a pre-determined large opposite current was put on to polarize the test electrode anodically. The change of polarity of the current was effected in about 10^{-7}-10^{-8} seconds by a Western type 275 B mercury-wetted relay switch[47]. The resultant potential-time transient was monitored by the Tektronix 535 A C.R.O. The Tektronix Type D

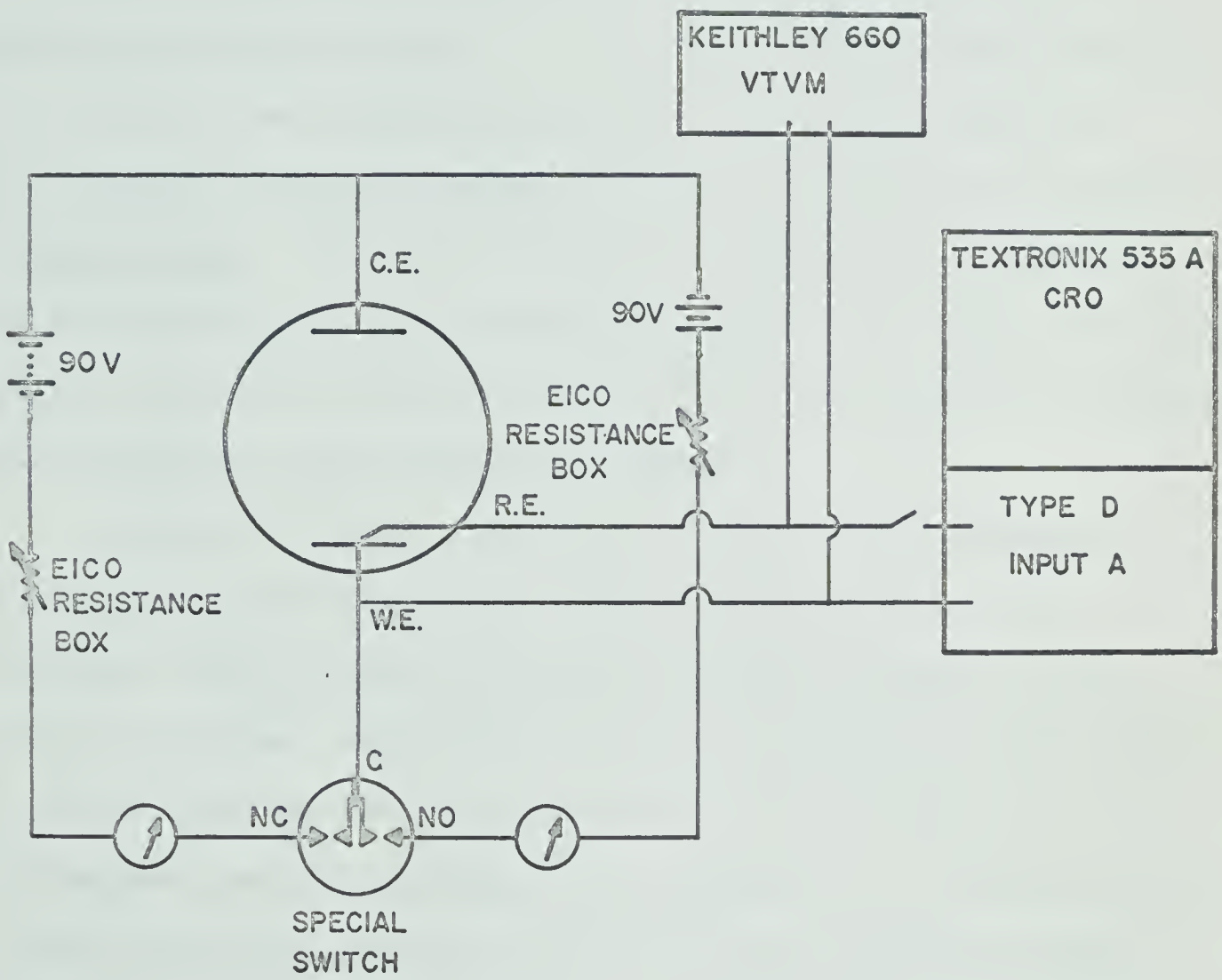

Fig. 5. Galvanostatic Stripping Electrical Circuit

plug-in unit was employed to amplify the signal to the C.R.O. Internal triggering of the oscilloscope was employed so that the transient was viewed the moment the relay was activated. The resulting electrode potential-time trace was photographed by an Exakta camera on a fast green-sensitive film, Polaroid type 47, speed 3000.

The procedures mentioned previously for preparing the cell and electrodes were employed. One molar NaOH solutions were employed. The electrode was cathodically polarized to a steady-state value for one-half to one hour before each anodic current pulse was applied.

Potential Step: This method involves the charging of the electrode at rest potential to a pre-determined potential. The charge associated with the quantity of adsorbed hydrogen atom on the surface is obtained by integration of the current-time transient.

As shown in Fig. 6a, a fast-rise Wenking 6432R potentiostat was employed for the experiment. The surface potential of the stainless steel electrode was obtained instantly between the W.E. and R.E. This was accomplished by automatic regulation of the current I which flowed from the C.E. to the W.E. as shown in Fig. 6b. The desired operating potential (U_s) originated in the reference input source (RIS) which included a battery (B), and a precision potentiometer (P). In the comparator (D), the potential (U_i), which existed between electrodes W.E. and R.E. was compared to U_s. The difference $E = U_s - U_i$ was amplified in a voltage amplified (VA) to VXE, which controlled the power amplifier (PA) from where the cell current (I) was supplied. The latter flowed from C.E. to W.E. and if necessary equalized the potentials U_s and U_i.

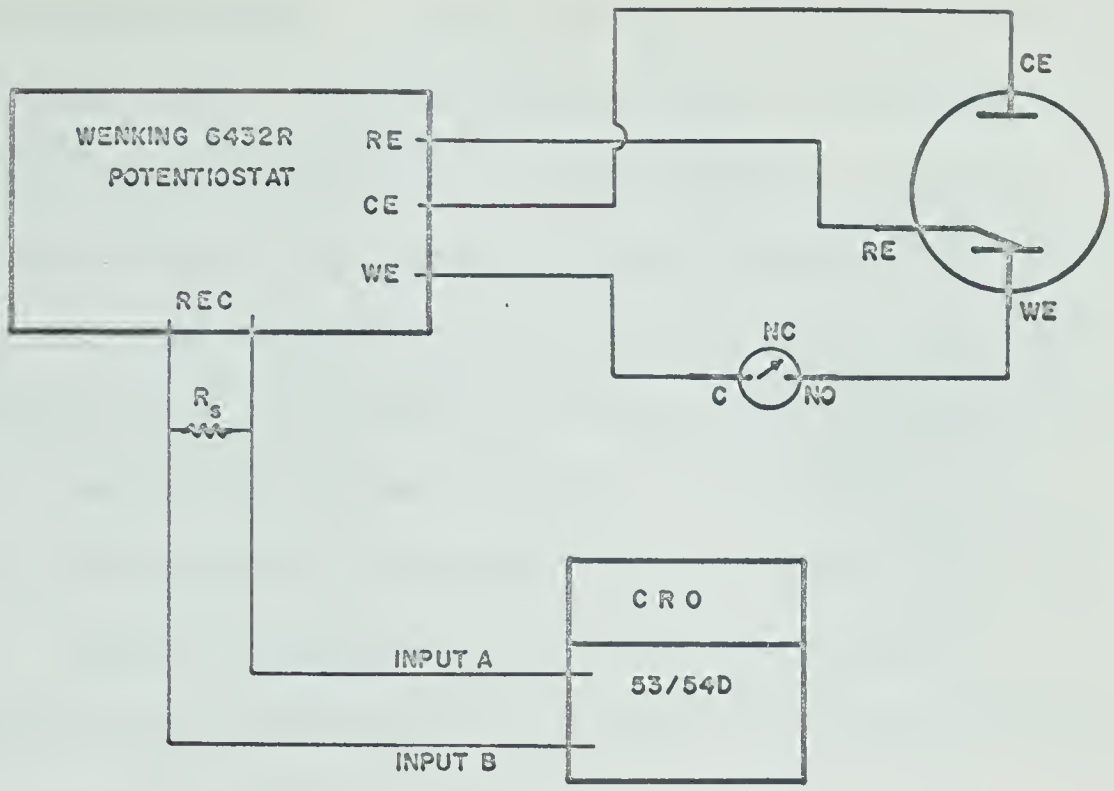

POTENTIAL STEP CIRCUIT

Fig. 6a. Potential-Step Electrical Circuit

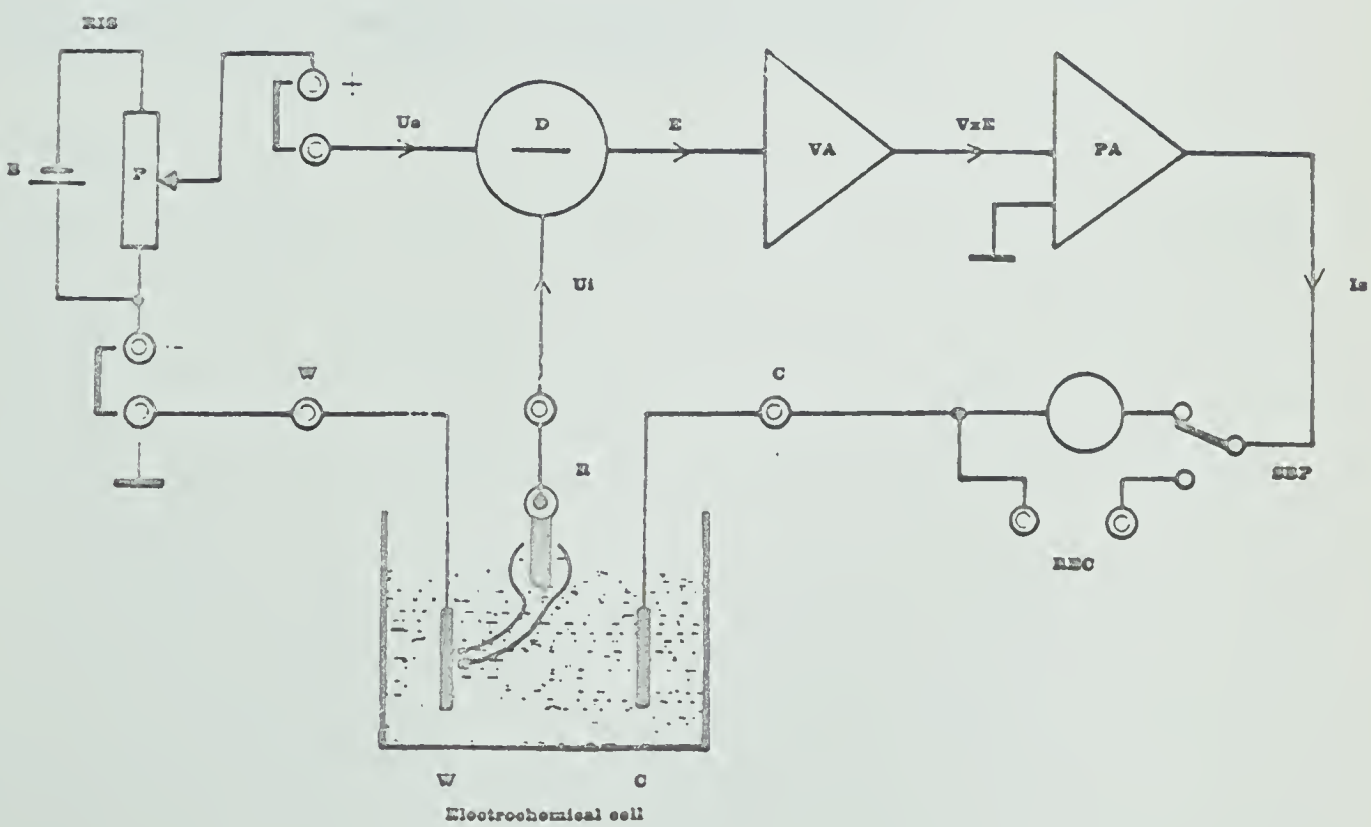

Fig. 6b. Fast-Rise Wenking Potentiostat Principle

The desired potential employed for the step was selected by the voltage divider dial. The same Hg-wetted relay was employed for switching on the potential step. A time dependent voltage drop across a GR precision 1 ohm resistor hooked across the RECORD terminals of the potentiostat was given by the resulting current transients. The Tektronix 535 A C.R.O. and the Tektronix Type D preamplifier were employed to monitor the current transient. A current-time plot was obtained by dividing the voltage scale by the value of the 1 ohm resistor. Internal triggering of the C.R.O. was employed. The i-t transients were photographed by an Exakta camera onto the fast green-sensitive polaroid land film.

Short shielded leads were used to connect the cell and the potentiostat.

One molar solution was employed in this set of experiments. The number of coulombs of electricity under the i-t transient was integrated with a Keuffel and Esser planimeter.

RESULTS

Oscillographs from DC Interruption

An oscillograph obtained with the dc interruptor method and its illustration are shown in Figs. 7a and 7b, respectively. The portion AC represents the decay overpotential for 100 μsec. when no external current flowed through the electrolytic cell. The portion CE represents the build-up of the electrode potential while the top line AF represents the sum of ohmic and activation overpotentials. In sufficient time the charging curve CE will meet with AF as shown in Fig. 9.

The electrolytic resistance between the polarizing electrode and the Luggin capillary tip gave an ohmic contribution to the total overpotential AF. This ohmic overpotential is indicated by AB of the decay curve and CD of the charging section. It can be seen that the decaying or the charging of an ohmic potential occurred in about 10 μsec. Ideally, the ohmic portions AB and CD should be nearly vertical. As shown in Figs. 7a, 8, 9 and 10, AB is a linear function of the electrolytic current which is a further proof that AB was of an ohmic nature. It should also be noted that the magnitudes of AB and CD are equal. Furthermore, the magnitudes of AB and CD increased when the distance between the polarizing electrode and the Luggin tip increased.

By adjusting the voltage divider to move B to ground G, the true activation overpotential was obtained. Point B remained at the same place when the PRF of the pulse generator was changed from 100 c.p.s. to 10 c.p.s. Point B also remained stationary when the pulse duration was increased from 100 μsec. to 500 μsec. The validity of measurement by moving point B to ground G was established by further measurement

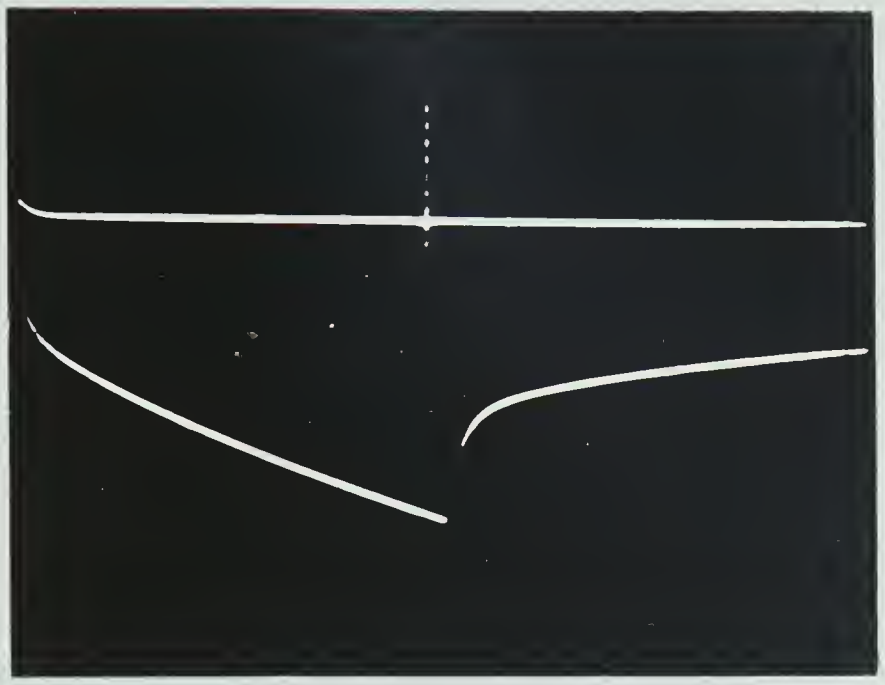

Fig. 7a. Oscillograph From DC Interruption.
$i = 5.4$ ma/cm^2.; $\varepsilon = -1.307$ vs. 1.0 M NaOH/HgO/Hg (+0.105 vs. NHE); 5 mv/cm.; 20 μsec/cm.

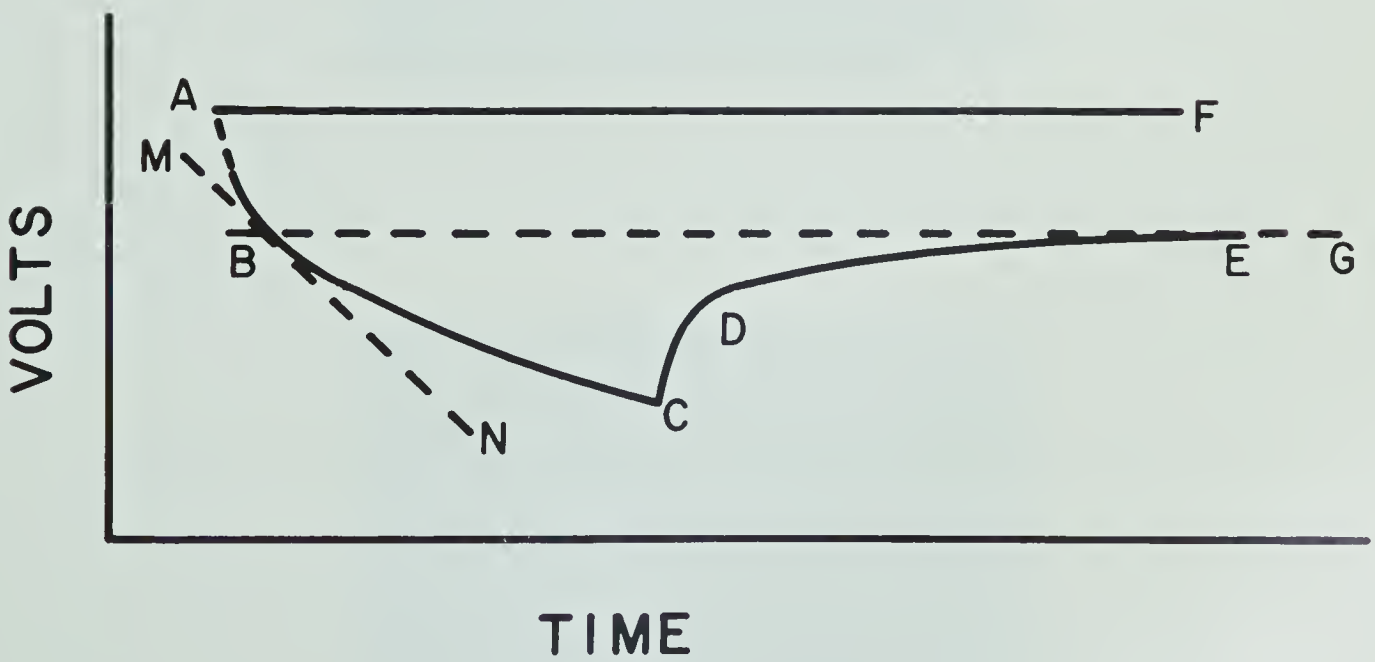

Fig. 7b. Illustration of 7a.

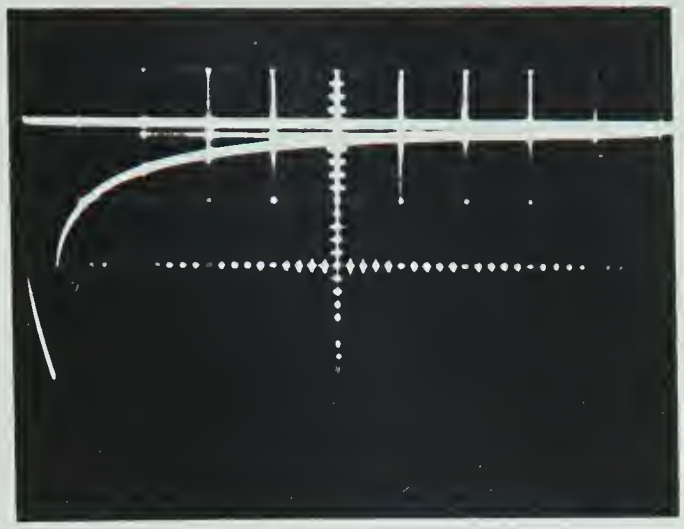

Fig. 8. Oscillograph From DC Interruption
5 mv/cm.; 0.2 msec/cm.

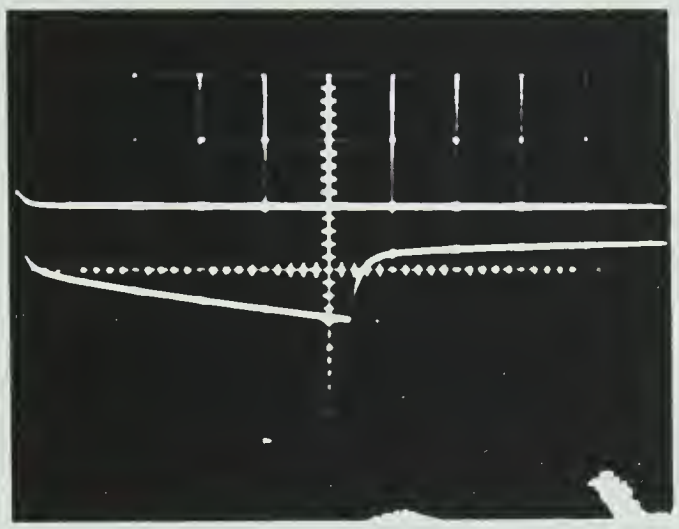

Fig. 9. Oscillograph From DC Interruption
i = 4.13 ma/cm.; ε= -1.261 vs. HgO/Hg; 5 mv/cm.; 20 μsec/cm.

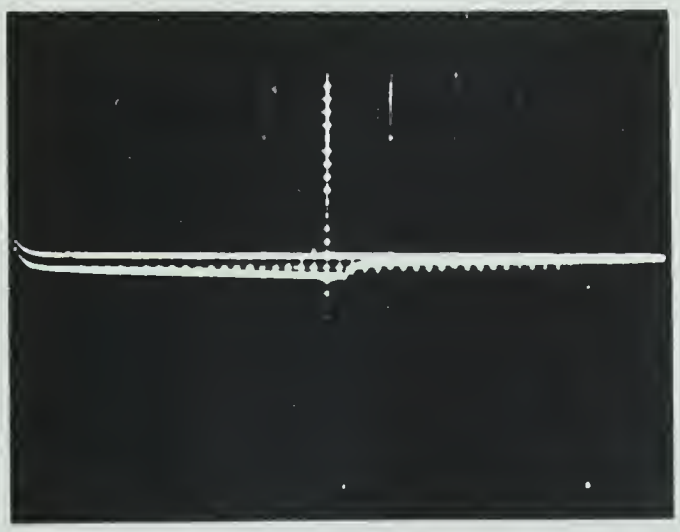

Fig. 10. Oscillograph From DC Interruption
i = 0.849 ma/cm^2.; ε = -1.176 vs. HgO/Hg; 5 mv/cm.; 20 μsec/cm.

with a Keithley 660 differential VTVM at low electrolytic currents where the ohmic overpotential was negligible.

Calculation of Electrode Capacity

The straight line MN was drawn tangent to B in Fig. 7b. The slope of line MN was employed to calculate the electrode capacity described by the equation[48],

$$C = -i\left(\frac{d\varepsilon}{dt}\right)^{-1}_{t=o} \tag{91}$$

For example, the slope of the line MN of the present oscillograph was measured after being magnified 3x onto a millimeter graph paper to be $\left(\frac{d\varepsilon}{dt}\right)_{t=o} = -0.187 \times 10^{-3} \frac{\text{volt}}{\text{sec.}}$. The steady-state current density at which this decay curve was taken was 5.47 ma/cm^2. By substituting these values into equation (91), the double layer capacity could be obtained.

$$C = -i\left(\frac{d}{dt}\right)^{-1}_{t=o} = 5.47 \times 10^{-3} \frac{\text{amp.}}{\text{cm}^2.} \times \left(0.187 \times 10^{3} \frac{\text{volt}}{\text{sec.}}\right)^{-1}$$

$$= 29.3 \times 10^{-6} \frac{\text{amp. - volt}}{\text{sec. - cm}^2.}$$

$$= 29.3 \frac{\mu C}{\text{cm}^2.}$$

Figs. 7a, 8, 9 and 10 show the amount of potential decay as a function of current density. The lower the current density, the smaller the amount of potential decay for a given period of time. Increasing the interruption time from 100 μsec. to 1 msec. did not increase significantly the amount of decay at current densities lower than 0.1 ma/cm^2. The slope MN was difficult to obtain accurately at current densities lower than 1 ma/cm^2. Even at current densities

higher than 1 ma/cm^2. slopes $\left(\frac{d\varepsilon}{dt}\right)_{t=o}$ could not be obtained with a precision better than 10-20%. Again, at rates higher than 40 ma/cm^2. less precise slopes were obtained because of higher ohmic overpotential contribution.

Time domain reflectometry (TDR) was introduced (explained in Appendix I) to obtain electrode capacity-potential relationships. The TDR technique eliminated the problem of obtaining precise initial potential-time slopes.

Reproducibility

A typical decreasing-increasing-decreasing of current density run plot taken over a 3-1/2 hour period is shown in Fig. 11. The measured cathodic potential was plotted against the logarithm of apparent current density. The down line (I) has a Tafel slope of -130 mv. while the second and third lines were -134 mv. and -142 mv. respectively. The combination of the lower Tafel slope and of the overpotential indicated that the initial electrode surface was less contaminated by adsorbed impurities during the first run. Generally, the potential went up after prolonged electrolysis indicating impurity effects. For this reason, the initial down runs are reported in this work.

When fresh solutions were employed, the overvoltages were reproducible to ±40 mv. which is comparable to that of the dropping mercury electrode in sodium hydroxide solutions by Bockris and Watson[3]. The lack of reproducibility of the overvoltage is connected with the great sensitivity of overvoltage to catalytically active impurities, with the high negative value of the potential, and with the attack of sodium hydroxide solutions on glass.

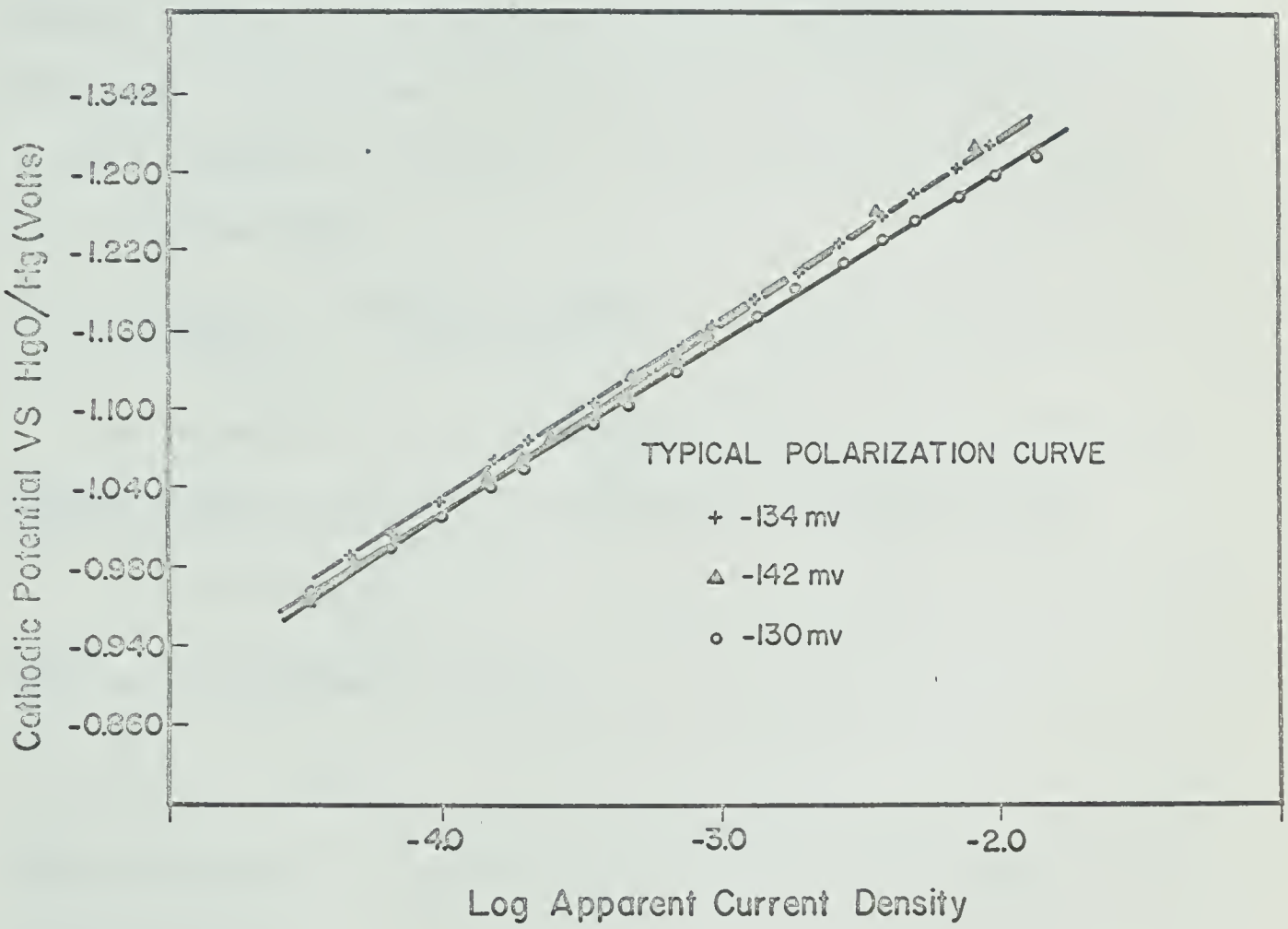

Fig. 11. Typical Tafel Plots of an Experiment

Calculation of Tafel Parameters

The experimental Tafel parameters a, b, i_o and α can be obtained from overpotential-log current density plots. Line I of Fig. 11 will be employed to illustrate this.

Tafel slope b was defined in the Theory section as $b = \frac{\partial \eta}{\partial \log i_c}$ or synonymously as the change of potential per decade change of current density. As such, the parameter b could be read directly from Line I. From Line I, the overpotential at 10^{-3} amp./cm^2. was -1.154 v. while at 10^{-4} amp./cm^2. the overpotential was -1.024 v.

It follows that

$$b = \frac{\partial \eta}{\partial \log i_c} = \frac{-1.154 - (-1.024)}{-3 - (-4)} = -0.130 \text{ v. or } -130 \text{ mv.}$$

The potential "a" can be obtained by extrapolating Line I to current density 1 amp./cm^2. or calculated from equation (25)

$$\eta = a + b \log i_c \tag{25}$$

which on rearrangement, becomes

$$a = \eta - b \log i_c \tag{92}$$

Using the values b = -0.130 v., $i_c = 10^{-3}$ amp./cm^2., and η = -1.154 v., it follows that

$$\begin{aligned} a &= -1.154 - (-0.130) \log 10^{-3} \\ &= -1.154 + 0.130\ (-3) \\ &= -1.154 - 0.390 \\ &= -1.540 \text{ v. vs. N.H.E.} \end{aligned}$$

An identical form of potential "a" is

$$a = -b \log i_o \tag{93}$$

Upon rearrangement the above expression becomes

$$\log i_o = \frac{-a}{b} \tag{94}$$

Substituting the values a = -1.540 v. and b = -0.130 v.,

$$\log i_o = -\frac{(-1.540)}{(-0.130)} = -11.7$$

or $i_o = 10^{-11.7}$ amp./cm^2., the exchange current density at $\eta = o$.

For b to approach -0.130 v., the theoretical form of b is

$$b = \frac{-2.303\ RT}{\alpha F}$$

From this expression the transfer coefficient α can be evaluated by inserting b = -0.130 v. and T = 35°C,

$$\alpha = \frac{-2.303\ RT}{bF} = -\frac{0.061}{(-0.130)} = 0.47$$

Effect of NaOH Concentration

The cathodic electrode potentials-logarithm of apparent current density relationships for 0.10, 1.0, 3.0, 5.0, and 10 M NaOH solutions are shown in Fig. 12-13 and Tables I-X (Appendix II). With the exception of the 5.0 M NaOH solution, a general trend of decreasing overpotential with decreasing NaOH concentration was observed. This difference was more noticeable at low current densities than at high current densities. At constant temperature and constant current density of $10^{-3}\ \frac{\text{amp.}}{\text{cm}^2}$, the derivative $\frac{\partial\eta}{\partial \log [OH^-]} = +23$ mv. was observed; while at $10^{-4}\ \frac{\text{amp.}}{\text{cm}^2}$ the derivative was about +48 mv.

Solutions saturated with He and then H_2 (the H_2 was purified by a Surfass purifier) showed higher hydrogen overvoltages and higher Tafel slopes than those saturated with only He. The difference in overvoltage was more noticeable at high current densities. The

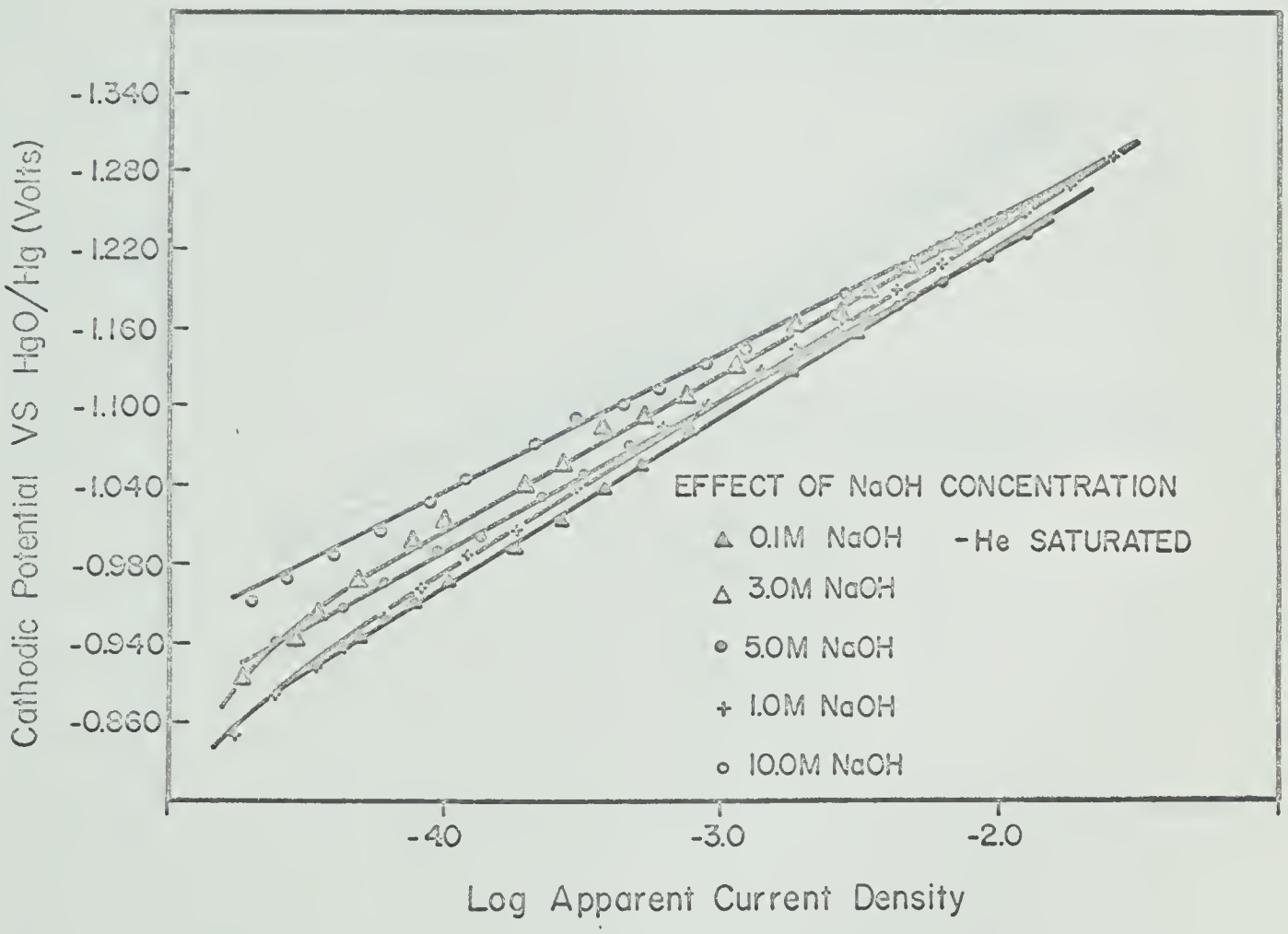

Fig. 12. Effect of Sodium Hydroxide Concentration. Helium Saturated

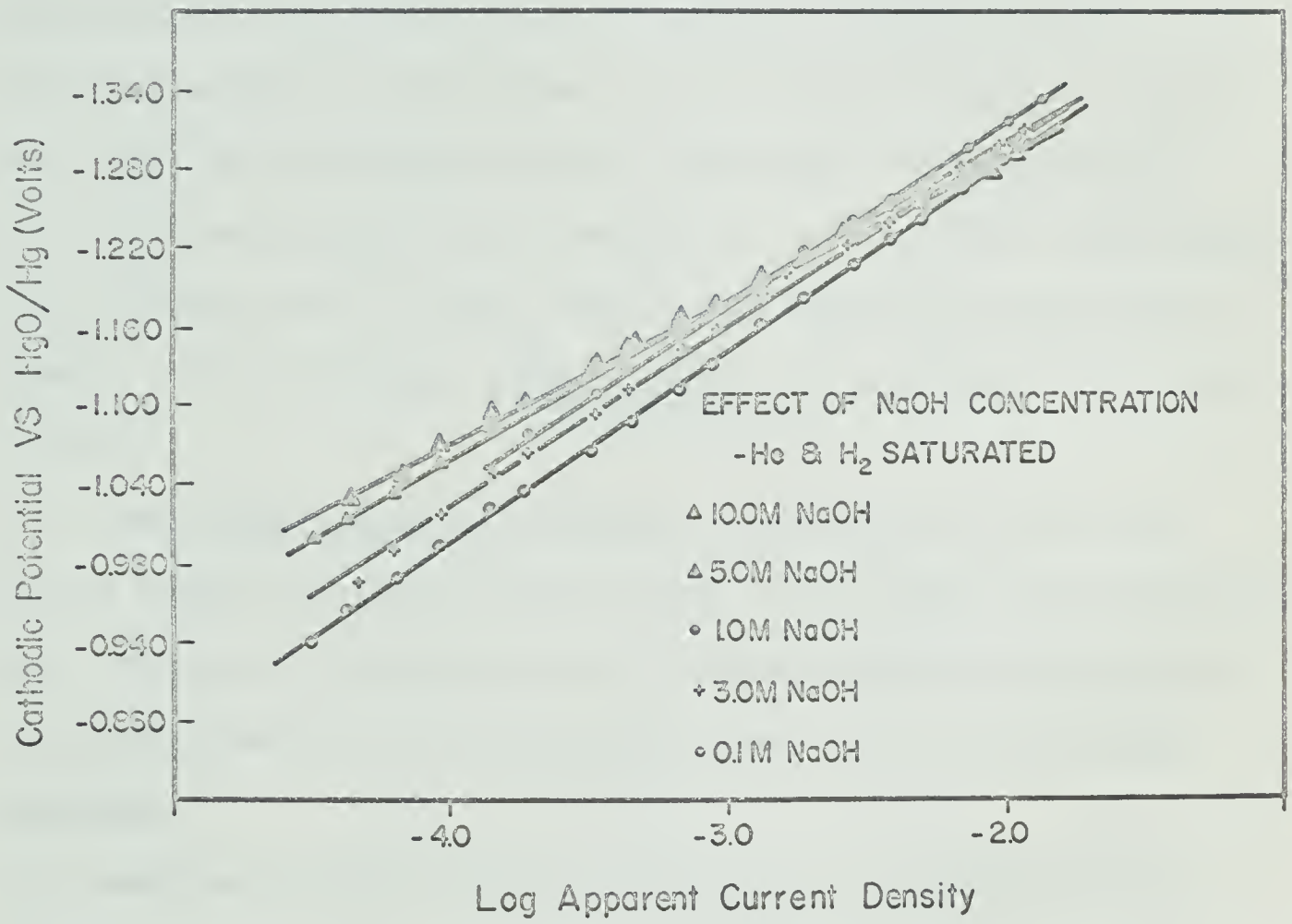

Fig. 13. Effect of Sodium Hydroxide Concentration. Helium and then Hydrogen Saturated.

experimental Tafel parameters are summarized in Table II. A constant capacity 25 - 45 $\mu f/cm^2$. was observed for the current density range studied. Therefore, no adsorption pseudo capacity is believed to be present.

Effect of Sodium Halides

The results of adding 0.1, 1.0 and 3.0 moles NaCl to 3.0 M NaOH solutions are shown in Fig. 14 and Table XI-XIII (Appendix II). No definite trend of overvoltage variation with the addition neutral salt could be noticed although the overvoltages for solutions with 3.0 M NaCl were higher than those with 1.0 or 0.1 M NaCl. Overvoltages for solutions with 1.0 M NaCl were in turn higher than those with 0.1 M NaCl. The relationship $\left(\frac{\partial \eta}{\partial \log [NaCl]}\right)_{i,T}$ was estimated to be about 20 mv.

Lower Tafel slopes were obtained by adding 2.9 or 4.9 M NaCl to 0.1 M NaOH solutions as shown in Fig. 15 and Tables XIV-XV (Appendix II). Addition of neutral salt to 0.1 M NaOH solution stabilized the electrode potentials, which fluctuated about ±25 mv. in pure NaOH solutions.

Addition of 10^{-3}, 10^{-2} and 10^{-1} M NaI to 3.0 M NaOH solutions showed an increase of overvoltage. Fig. 16 and Tables XVI-XVIII show that overvoltages decreased in the order of $10^{-3} > 10^{-2} > 10^{-1}$ M NaI added.

The effect of halide anion size on the hydrogen overvoltage at the stainless steel electrode is compared in Fig. 17 and Tables XIX-XXII. No clearcut picture could be observed but the overvoltage seemed to increase with anion size.

Table II

Table of Tafel Parameters

Solution	-a (volt)	-b (volt)	$-\log i_o$	
He saturated				
0.10 M NaOH	1.487	0.134	11.1	0.45
1.0 M NaOH	1.503	0.133	11.3	0.45
3.0 M NaOH	1.476	0.121	12.2	0.50
5.0 M NaOH	1.524	0.115	11.6	0.53
10 M NaOH	1.445	0.104	13.9	0.58
He and then H_2 saturated				
0.10 M NaOH	1.576	0.146	10.8	0.41
1.0 M NaOH	1.584	0.139	11.4	0.44
3.0 M NaOH	1.577	0.136	11.6	0.45
5.0 M NaOH	1.536	0.120	12.8	0.50
10 M NaOH	1.490	0.108	13.8	0.56

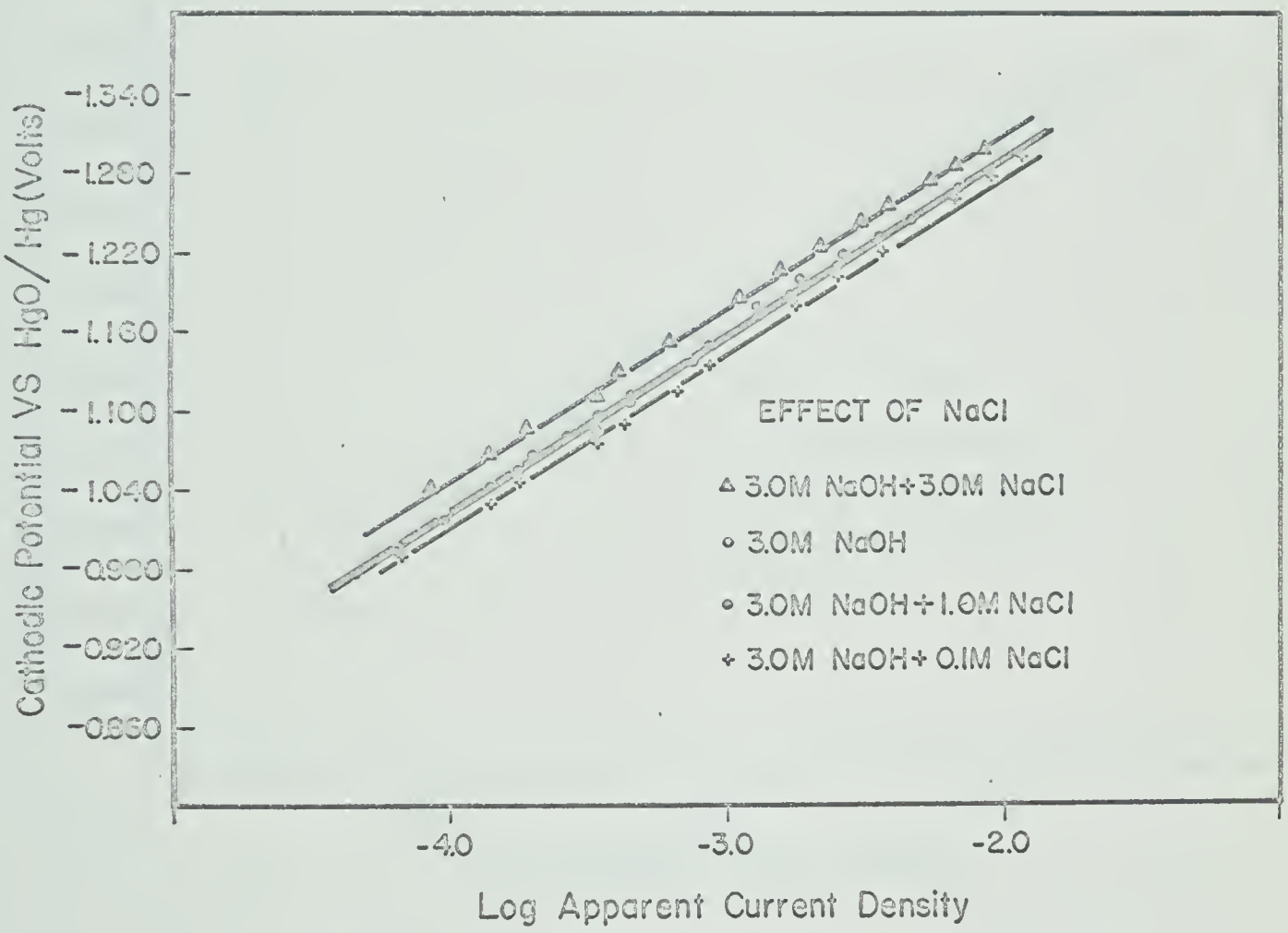

Fig. 14. Effect of Sodium Chloride

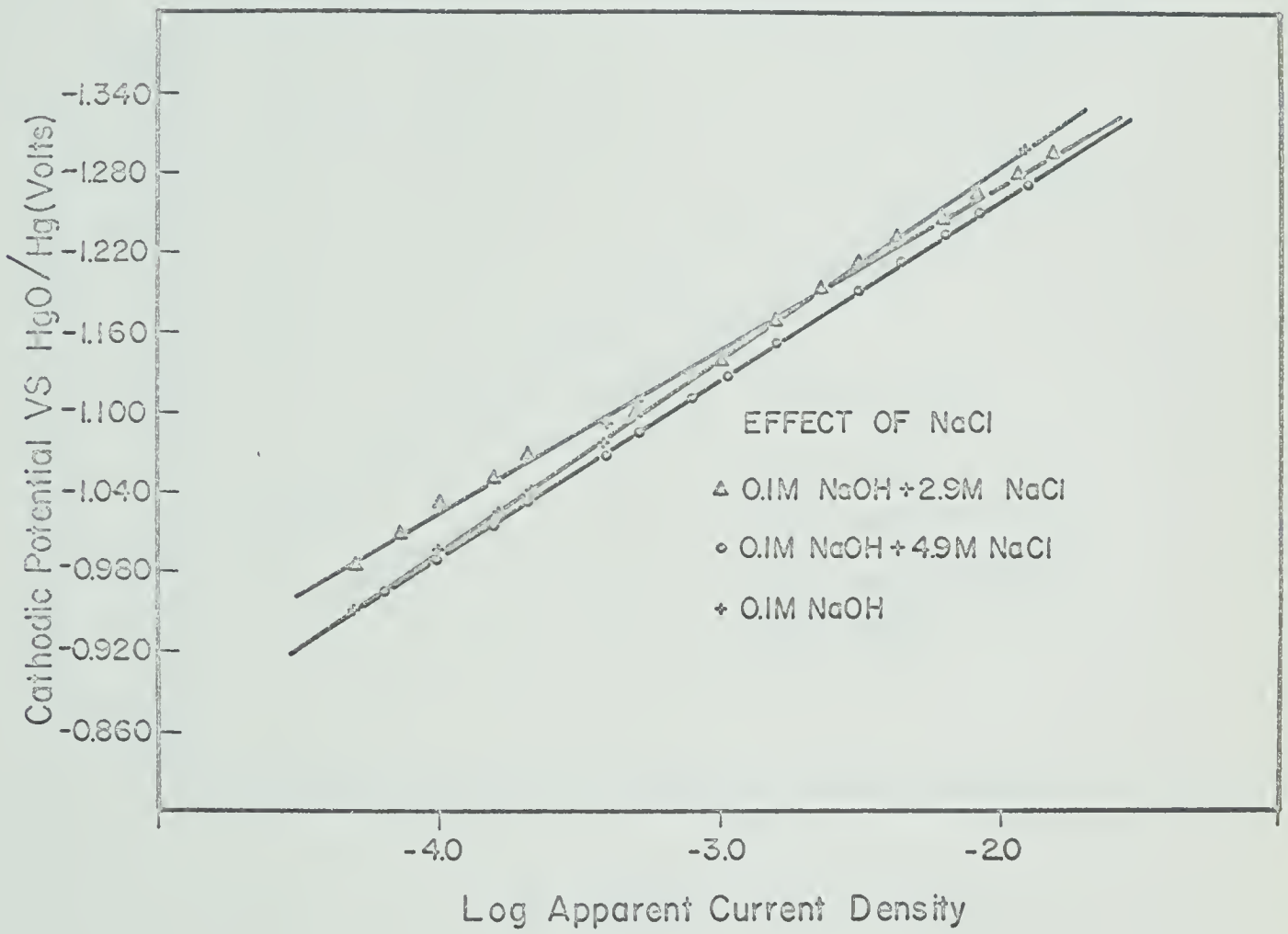

Fig. 15. Effect of Sodium Chloride

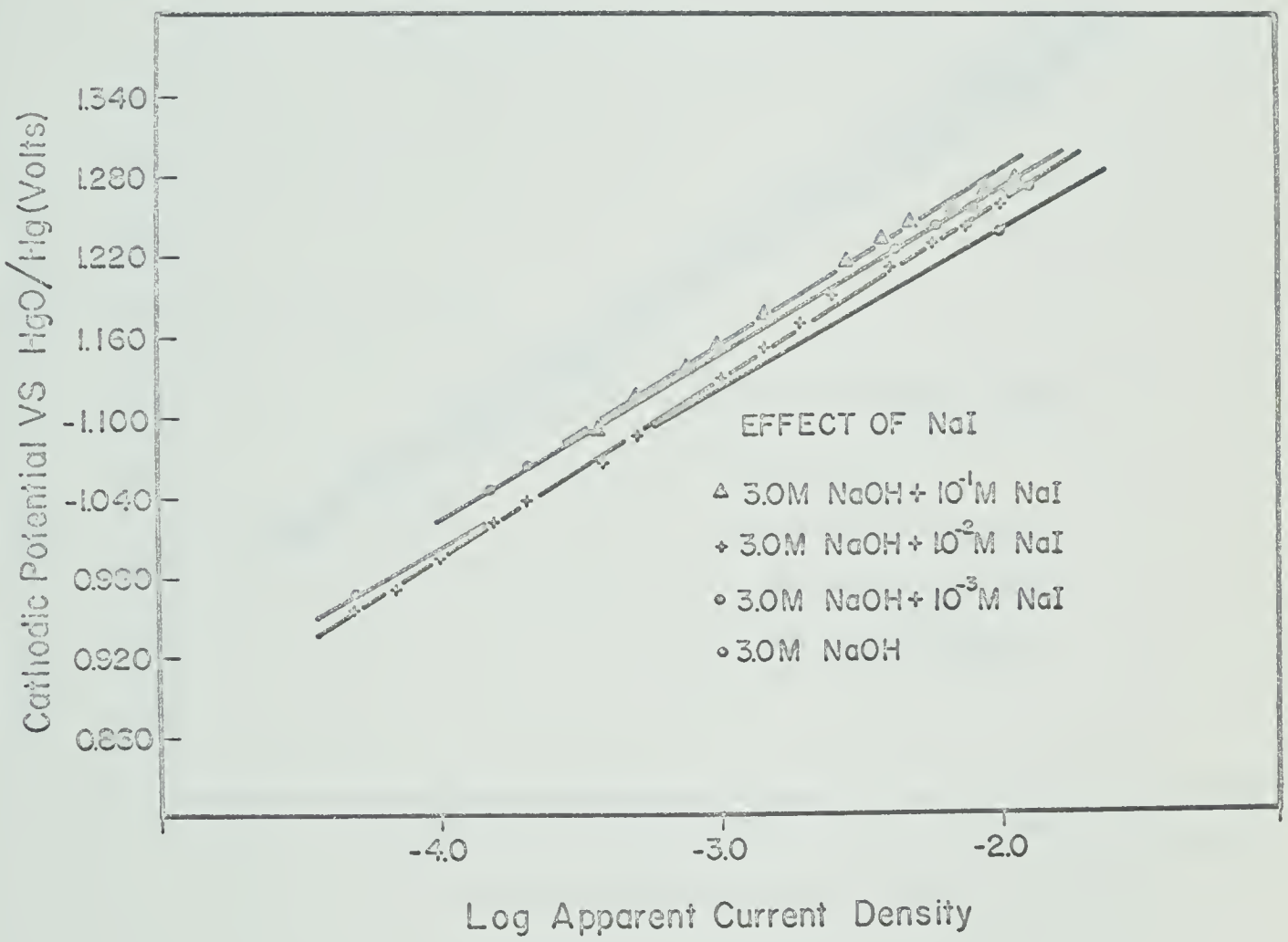

Fig. 16. Effect of Sodium Iodide

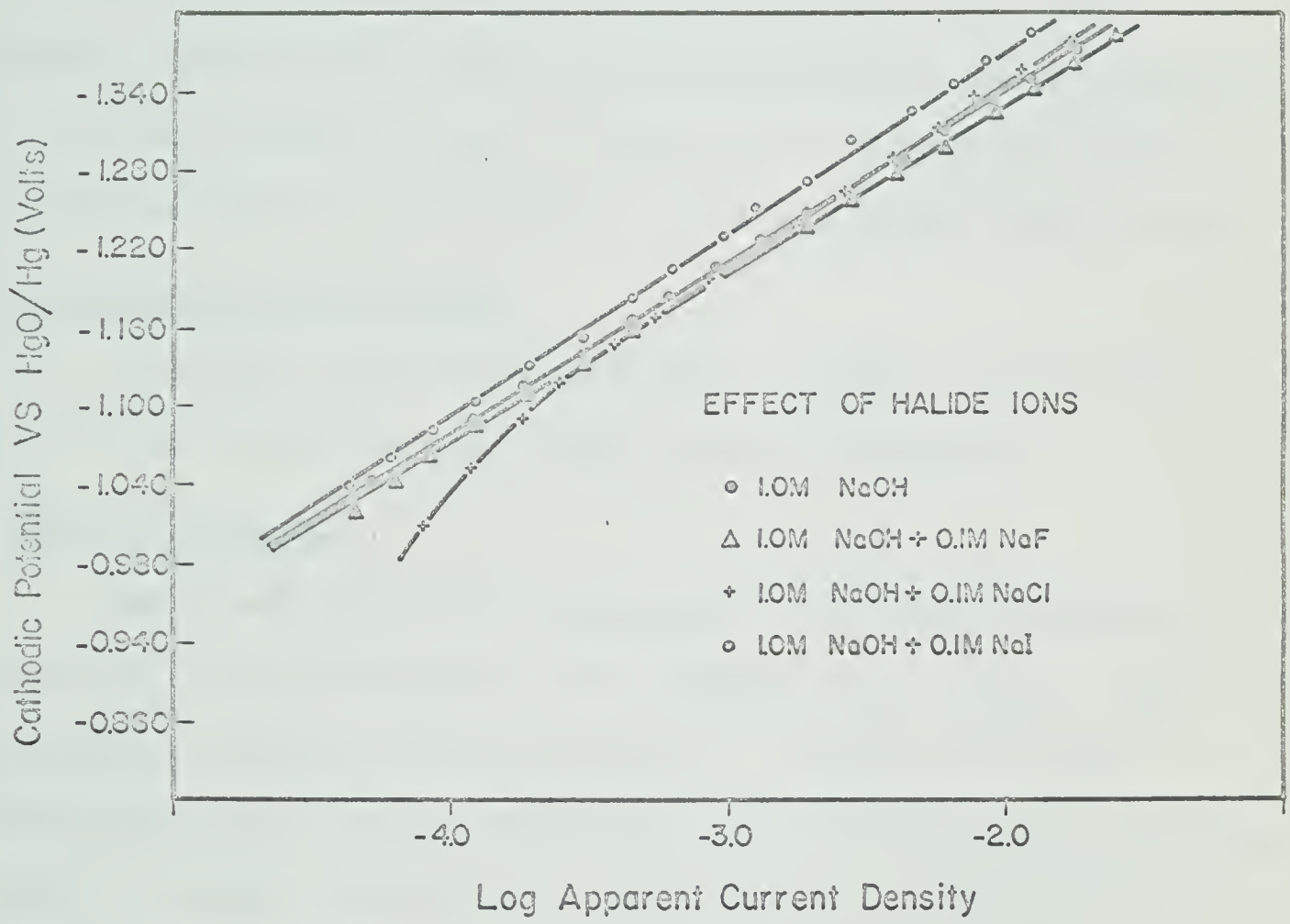

Fig. 17. Effect of Halide Anion Size

Effect of Cation Charge

The overvoltage was lowered slightly with the addition of Ba^{+2} and La^{+3}. This was more evident at higher current densities as shown in Figs. 18-19 and Tables XXIII-XXIV.

Effect of Another Electroactive Species

Addition of reducible IO_3^- to molar NaOH solutions caused hydrogen to evolve at a higher cathodic potential as shown in Fig. 20 and Tables XXV-XXVII. With 0.1 M $NaIO_3$ in 1.0 M NaOH the hydrogen evolution region was not reached in the normal current density region.

High Current Density Studies

A limiting current density of about 4.5 $\frac{amp.}{cm^2.}$ was obtained in 1.0 M NaOH solution as shown in Fig. 21 and Table XXVIII.

Effect of Ammonia

Ammonia was added to the electrolyte in an attempt to dissolve any Cr_2O_3 and/or NiO present on the stainless steel surface; these oxides are slightly soluble in ammonia[49]. Fig. 22 and Tables XXIX-XXXI showed that the overvoltage lowered noticeably with increasing amount of ammonia added to 3.0 M NaOH solution. This suggested a small amount of oxide may have been dissolved , thus resulting in a decrease of adsorption energy for hydrogen by the electrode surface.

Effect of Electrodeposition of Elements Fe and Ni

An attempt was made to cover various fractions (less than a monolayer) of the stainless steel electrode surface with either Ni or Fe. Element Fe was deposited from a bath consisting of $FeCl_2$, $FeSO_4$, and NH_4Cl while element Ni was deposited from a bath consisting of $NiCl_2$, $NiSO_4$, and H_3BO_3[50].

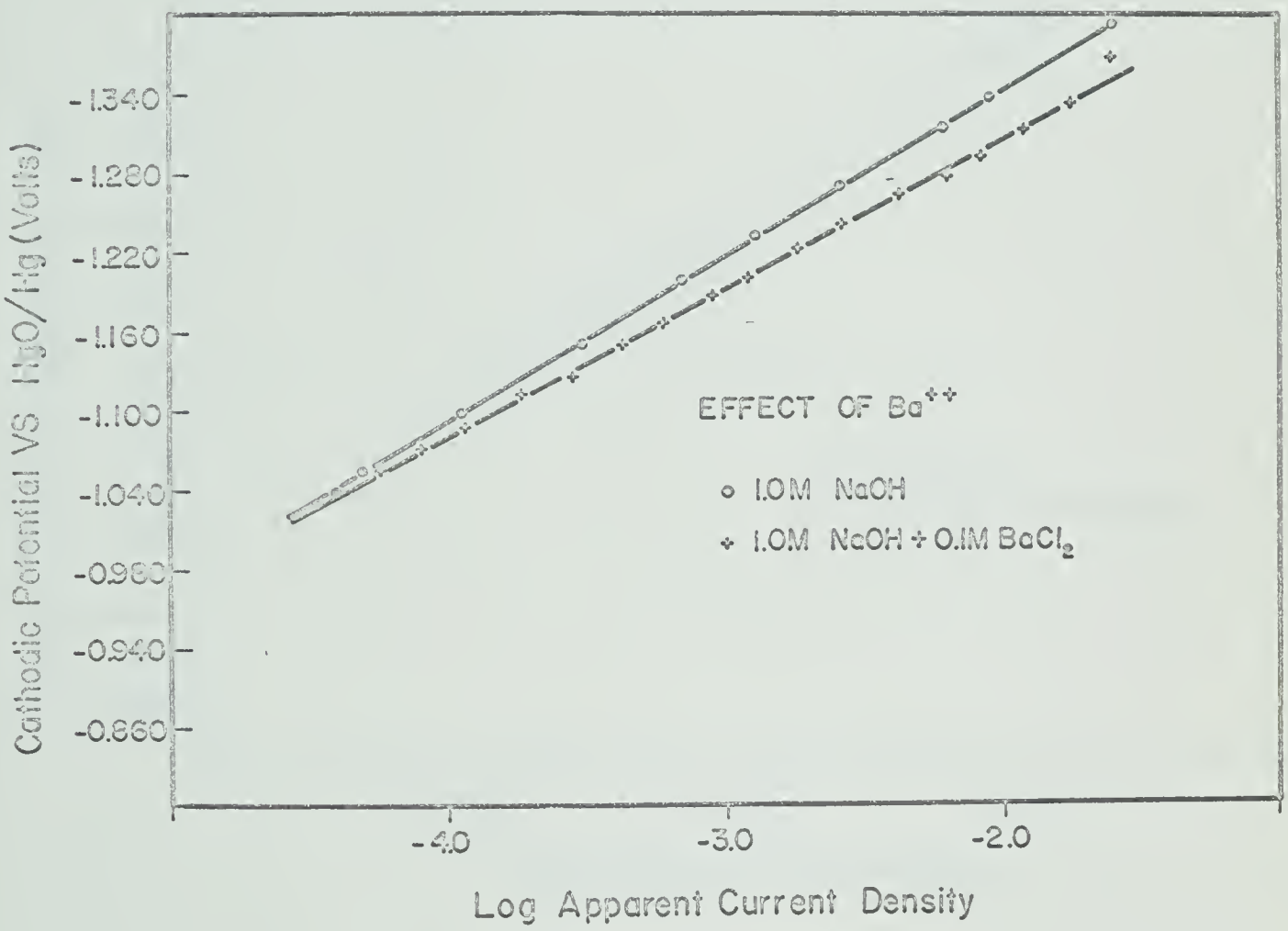

Fig. 18. Effect of Barium Ion

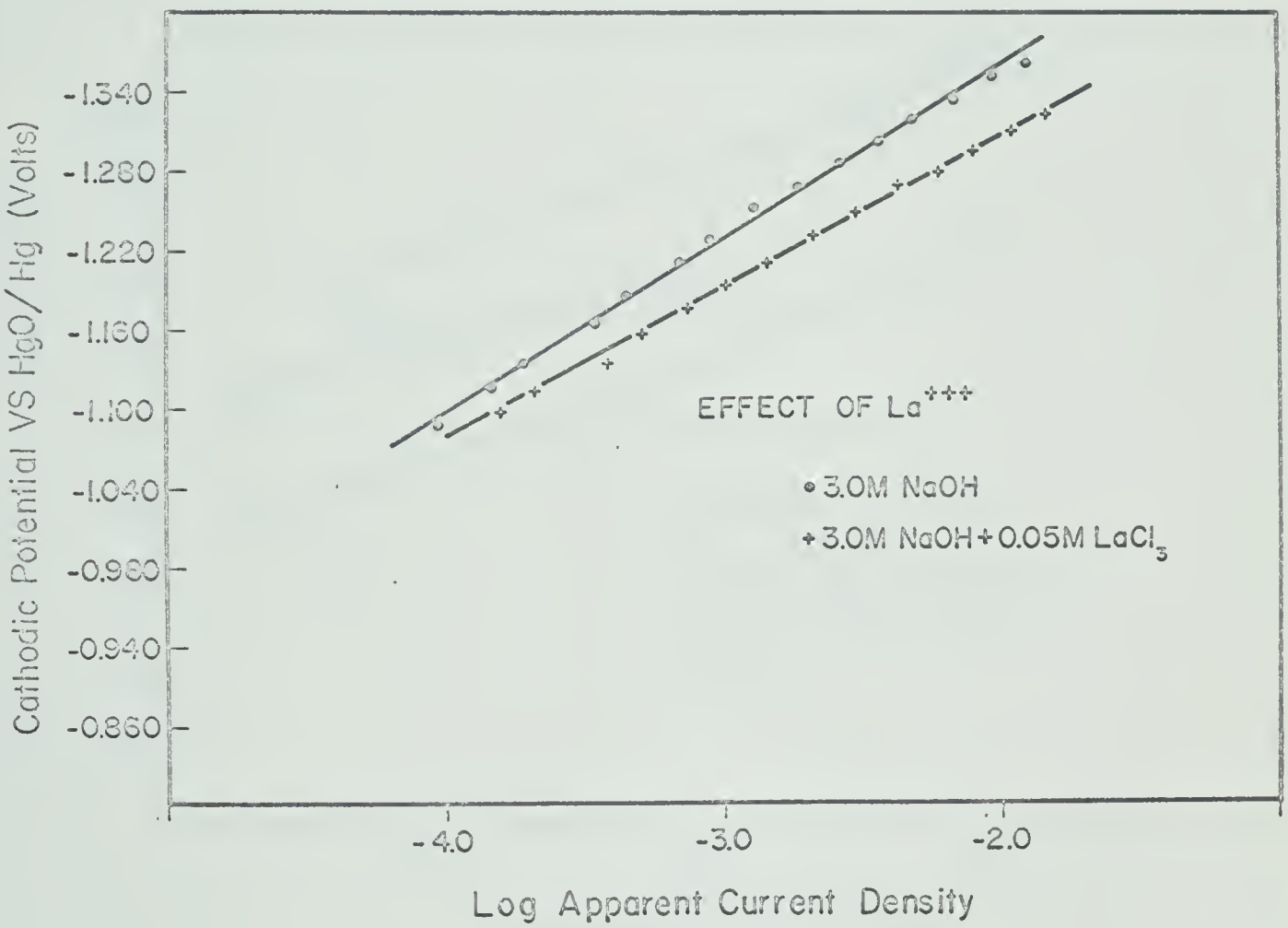

Fig. 19. Effect of Lanthanum Ion

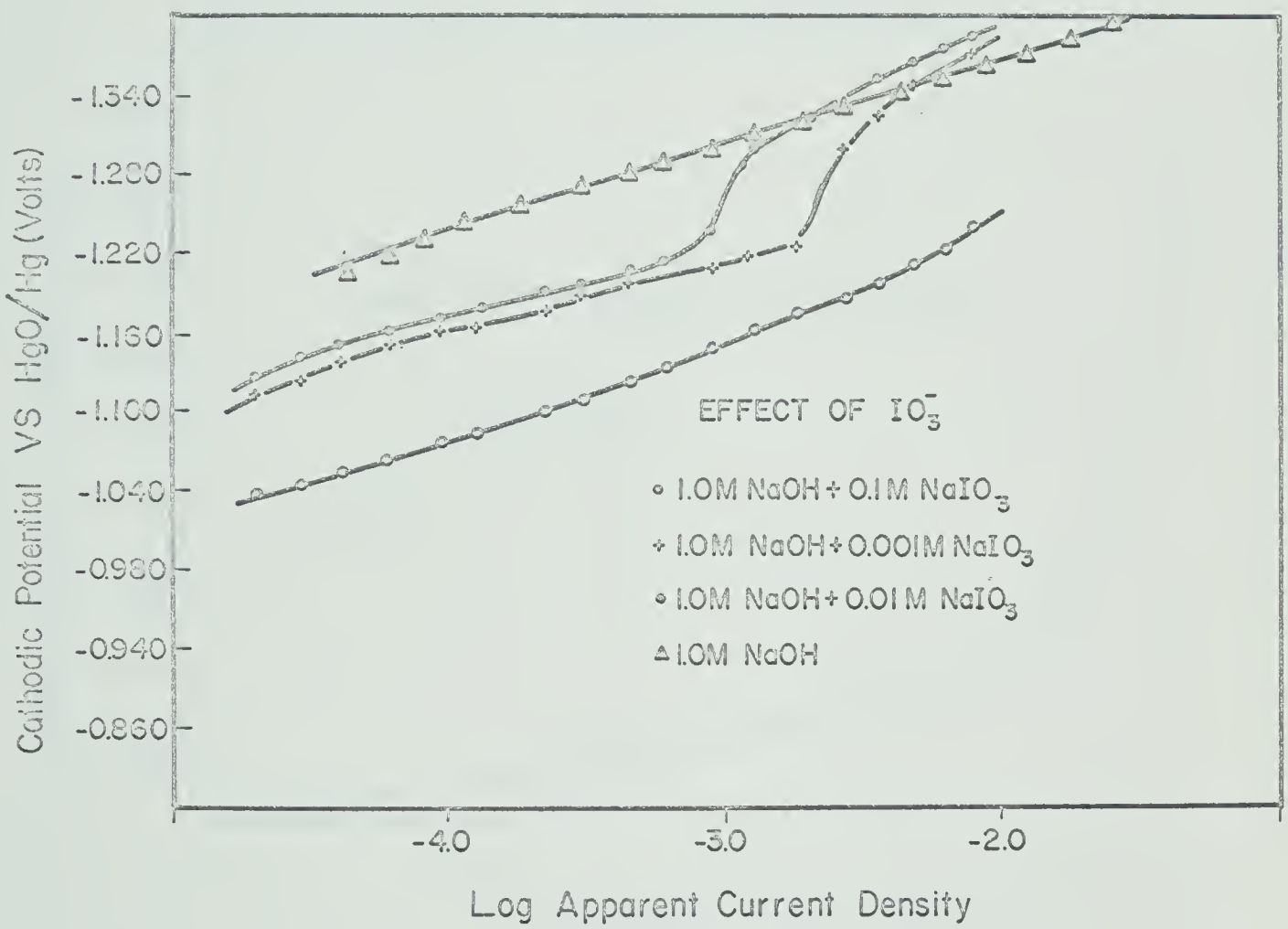

Fig. 20. Effect of Iodate Ion

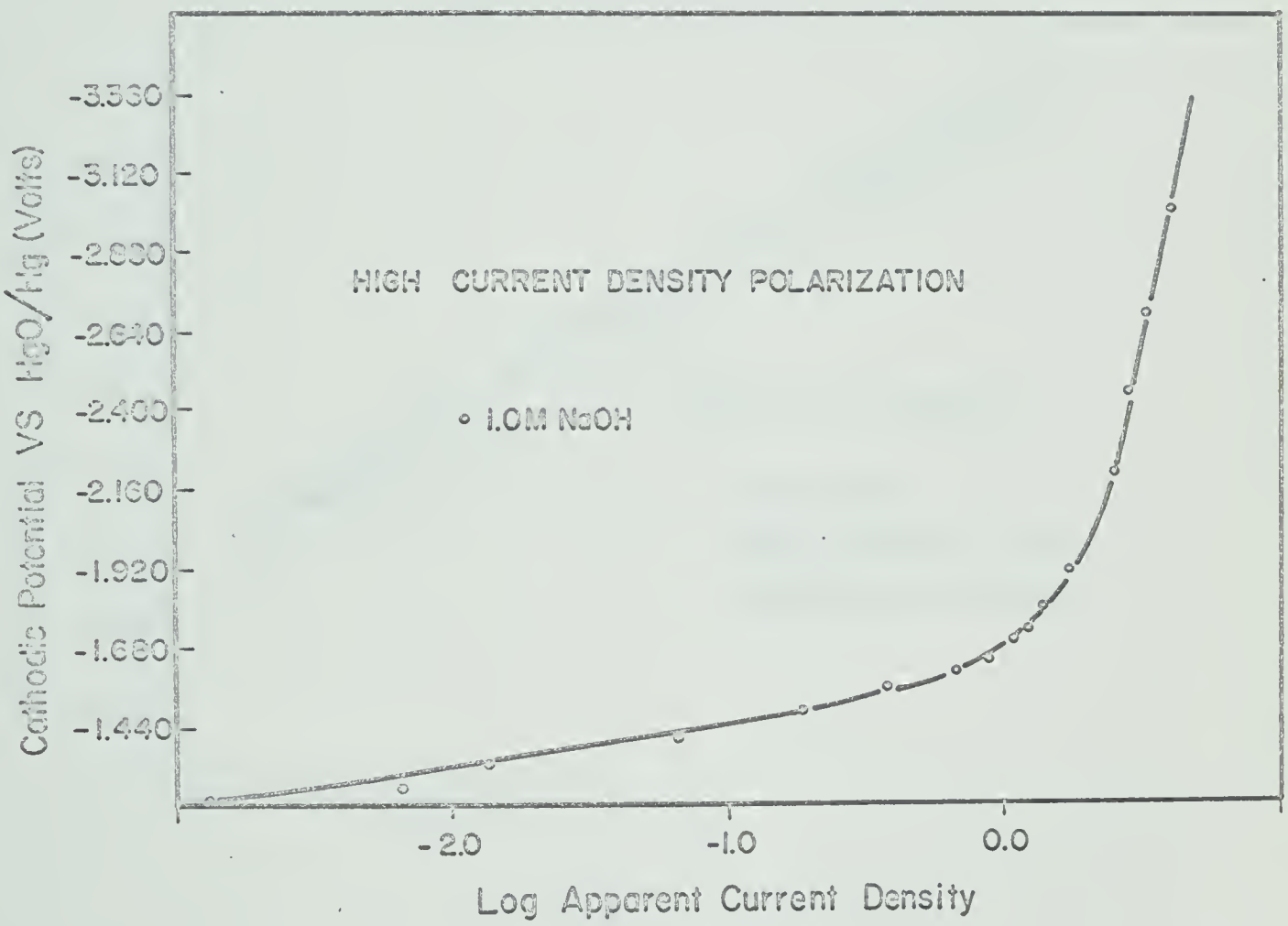

Fig. 21. High Current Density Studies

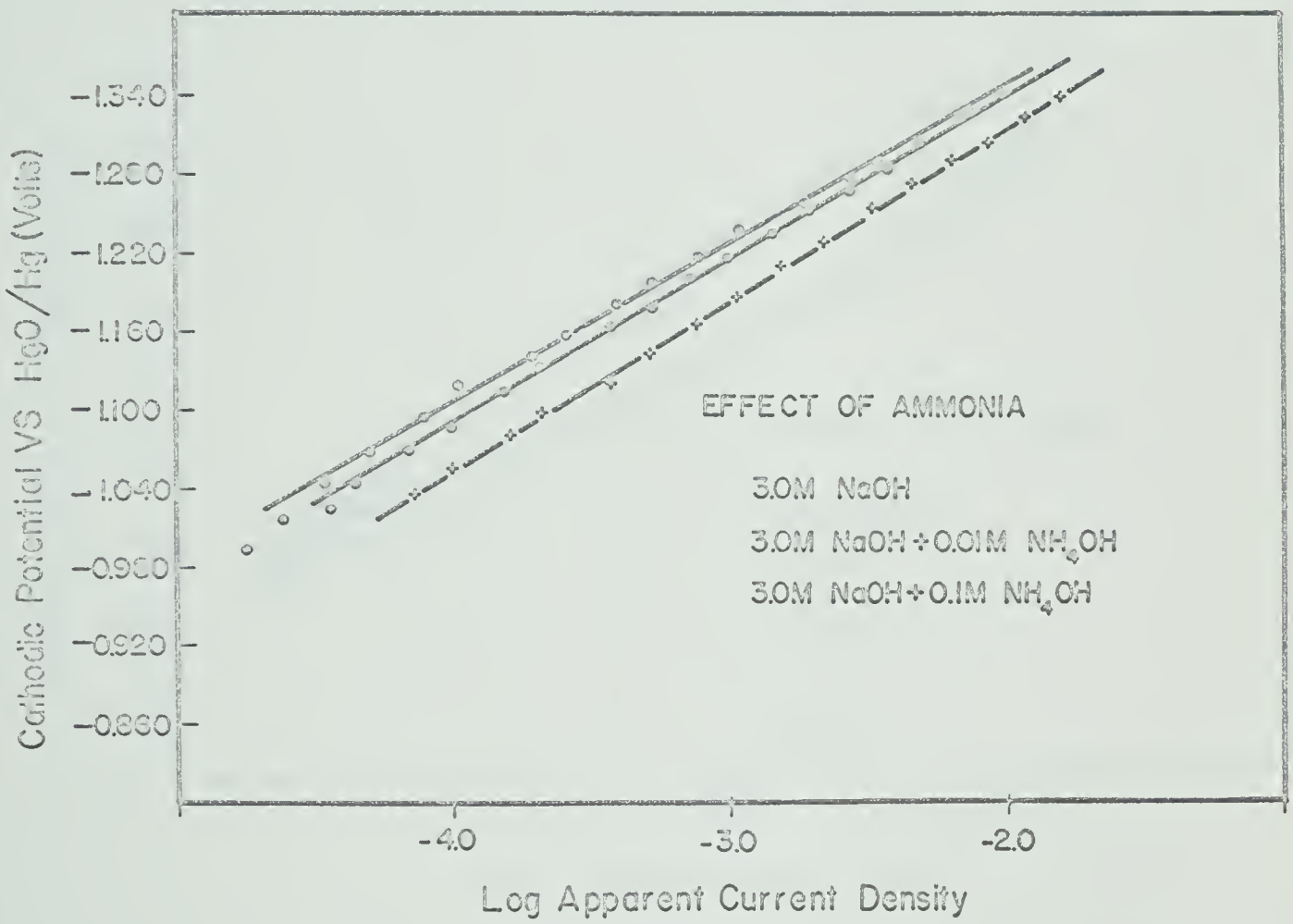

Fig. 22. Effect of Ammonia

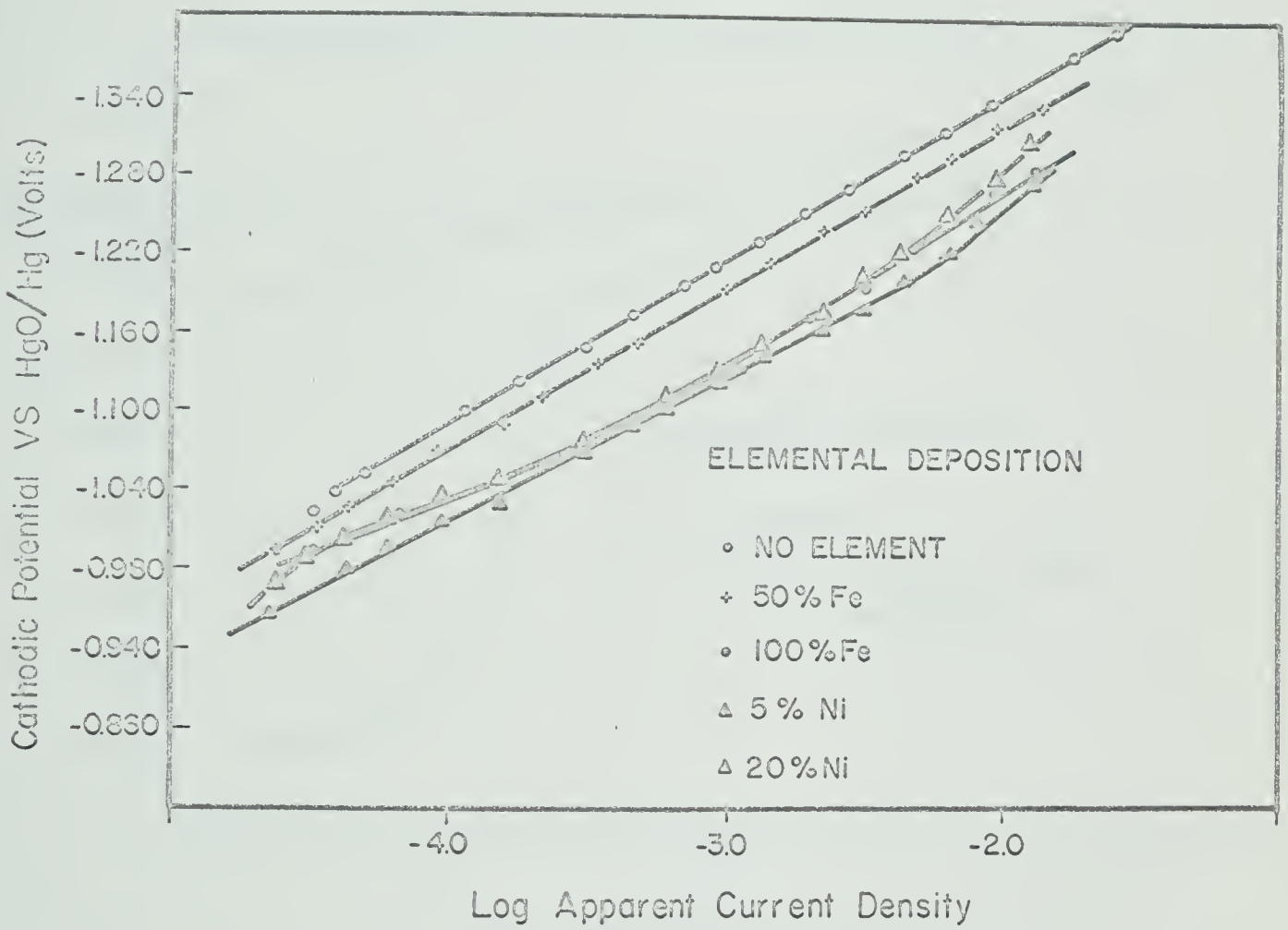

Fig. 23. Effect of Elements Fe and Ni

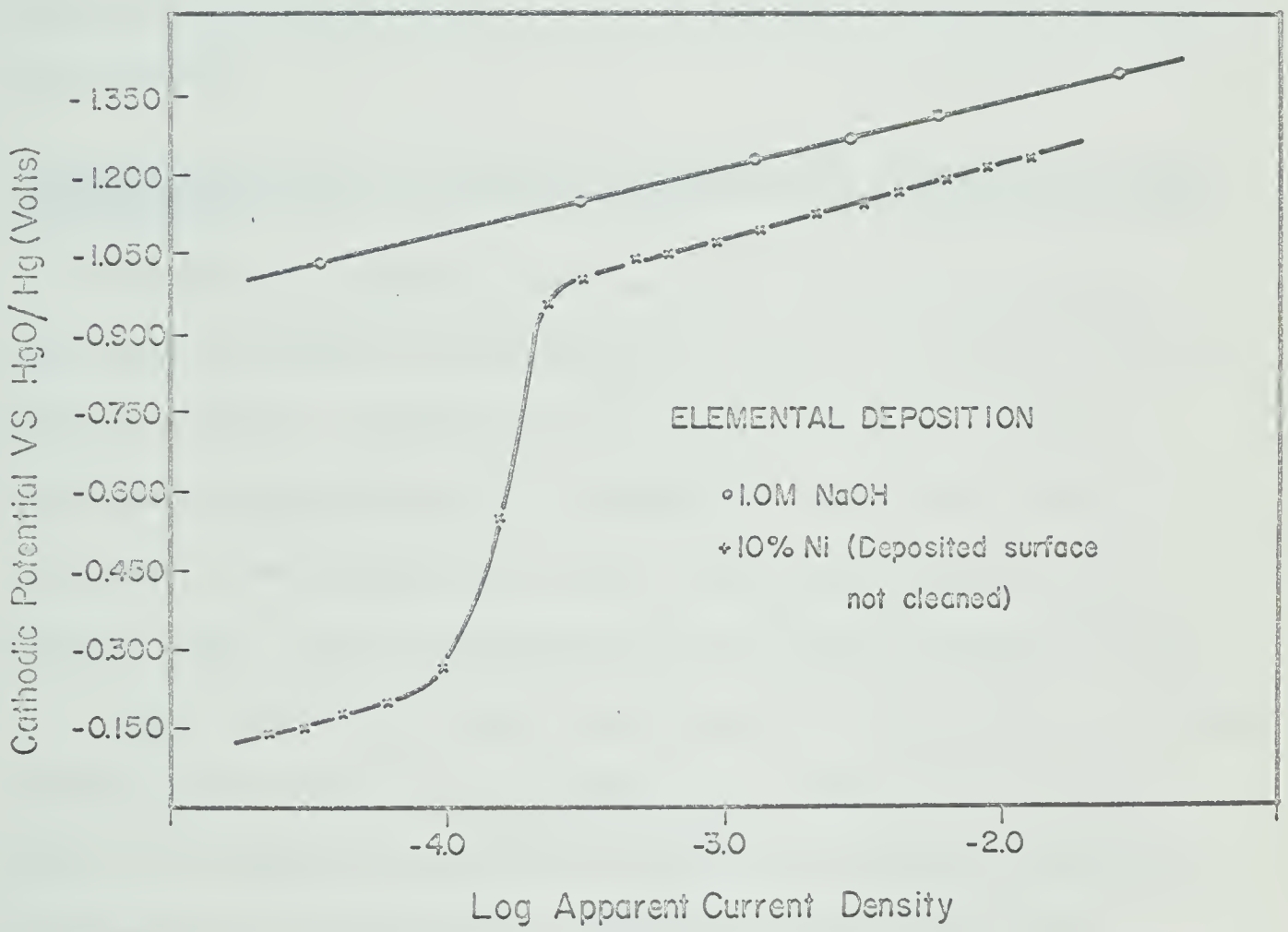

Fig. 24. Miscellaneous

As shown in Fig. 23 and Tables XXXII-XXXV, coating 100% of the surface with Fe or 5% or 10% of the surface with Ni produced irregular Tafel behaviours. In the latter conditions overpotential was lowered by as much as 70 mv.

An interesting potential-log rate relationship is shown in Fig. 24 and Table XXXVI. The electrode was transferred directly from the Ni plating bath to the electrolysis cell without cleaning the electrode.

Alteration of Nature of Electrode Surface by Pickling and Prolonged Electrolysis

Pickling the stainless steel surface with 1:1 HCl and H_2SO_4 acid mixture produced a brownish-black surface. As shown in Fig. 25 and Table XXXVII, a lowering of the overpotential was observed. At current density 10 ma/cm^2., the decrease was 110 mv. while at 0.1 ma/cm^2., the decrease was 50 mv. The Tafel slope of -0.102 v. was much lower than that observed for the normal electrode surface.

A very dark black surface was obtained on electrolysis at current density of 12.5 ma/cm^2. for 44 hours and 4.5 amp./cm^2. for 2-1/2 hours. No significant potential variation was observed during the prolonged electrolysis period. As shown in Fig. 25 and Table XXXVIII (Appendix II), Tafel behaviour was not observed at current densities lowere than 0.6 ma/cm^2. On scraping the black substance off gently with a spatula a new shiny surface appeared, indicating hydrogen embrittlement. Without scraping the surface free of the black material the shiny surface reappeared on dipping the electrode into an oxidizing acid bath like chromic-sulfuric or nitric-sulfuric. The same potential was observed on cathodic polarization at the same

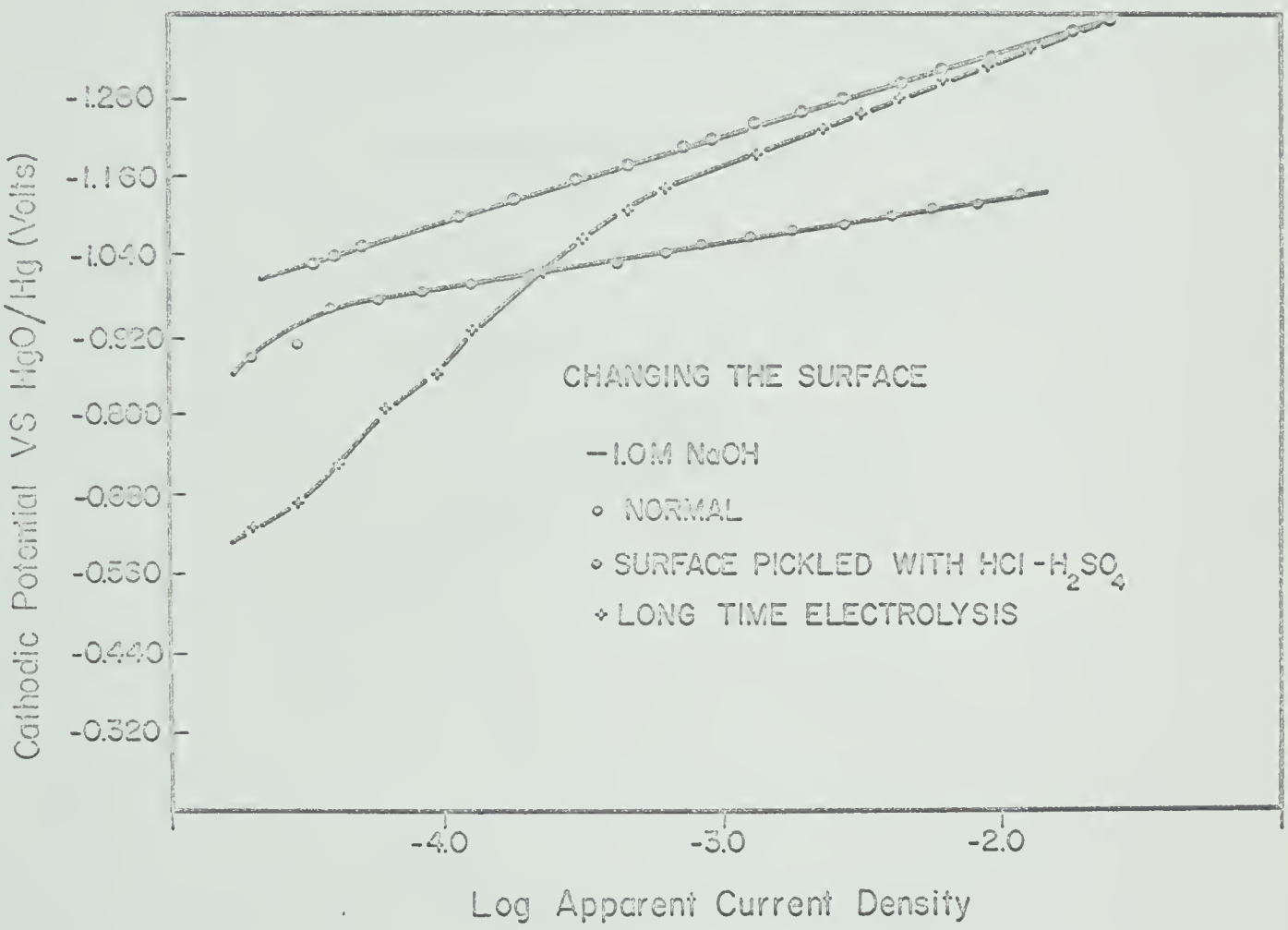

Fig. 25. Effect of Alteration of Nature of Electrode Surface

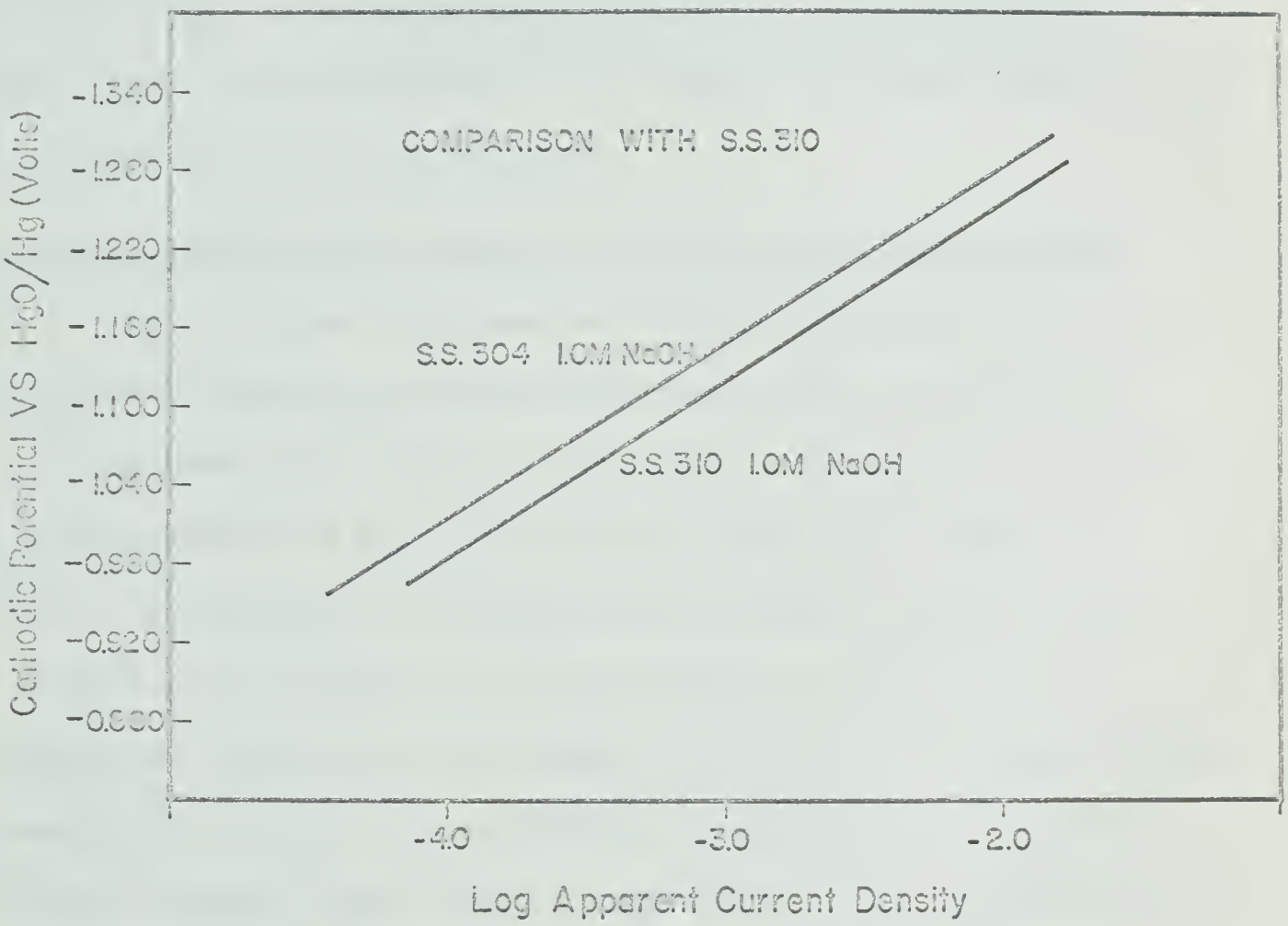

Fig. 26. Comparison of Stainless Steels 304 and 310

current density.

Comparison of Stainless Steel Types 304 and 310

Commercial stainless steel type 310, which has a composition of 2% Mn, 1.50% Si, 24-26% Cr, 19-22% Ni, 0.045% P, 0.030% Si, approximately 0.25% and the remaining Fe, was polarized in the same current density range. As shown in Fig. 26 and Table XXXIX (Appendix II), a slight lowering of overpotential was observed. It could not be related to the difference in the amount of oxides because of the uncertainty of the surface areas.

Interpretation of Galvanostatic Stripping Chronopotentiograms

Fig. 27a shows a galvanostatic anodic charging potential-time transient immediately after steady-state cathodic polarization. To comprehend each individual kink which occurred in the transient, an illustration of Fig. 27a is shown in Fig. 27b. Point "a" at t=o corresponds to the steady-state cathodic potential while section ab corresponds to the double layer charging. When the electrical double layer rearranged to point "b" an electrode process was able to occur at this potential. The oxidation of adsorbed atomic hydrogen formed during steady-state cathodic polarization is indicated by the horizontal region bc. After all of the atomic hydrogen had been ionized, the electrical double layer rearranged to a new potential so that a new electrode process was able to occur as indicated by the section cd. According to Bockris[51] the possible intermediates involved in oxygen evolution were metal hydroxides (M-OH) and metal oxides (M-O) and/or metal-peroxides ($M-HO_2$). As such, chromium, nickel, and iron hydroxides were probably formed in

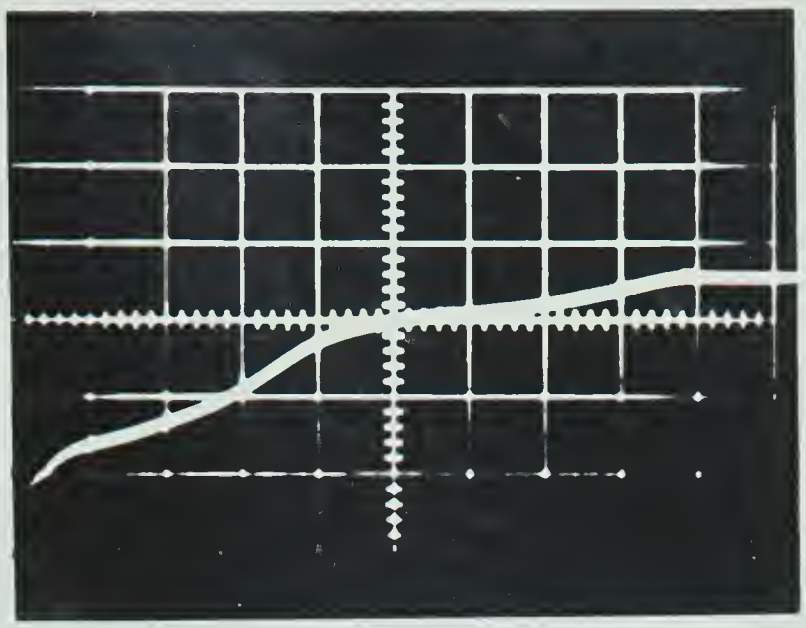

Fig. 27a. Galvanostatic Stripping Transient
ε = -1.132 vs. HgO/Hg; i_c = 0.3 ma/cm^2
i_a = 12 ma/cm^2.; 500 mv/cm; 0.2 sec/cm.

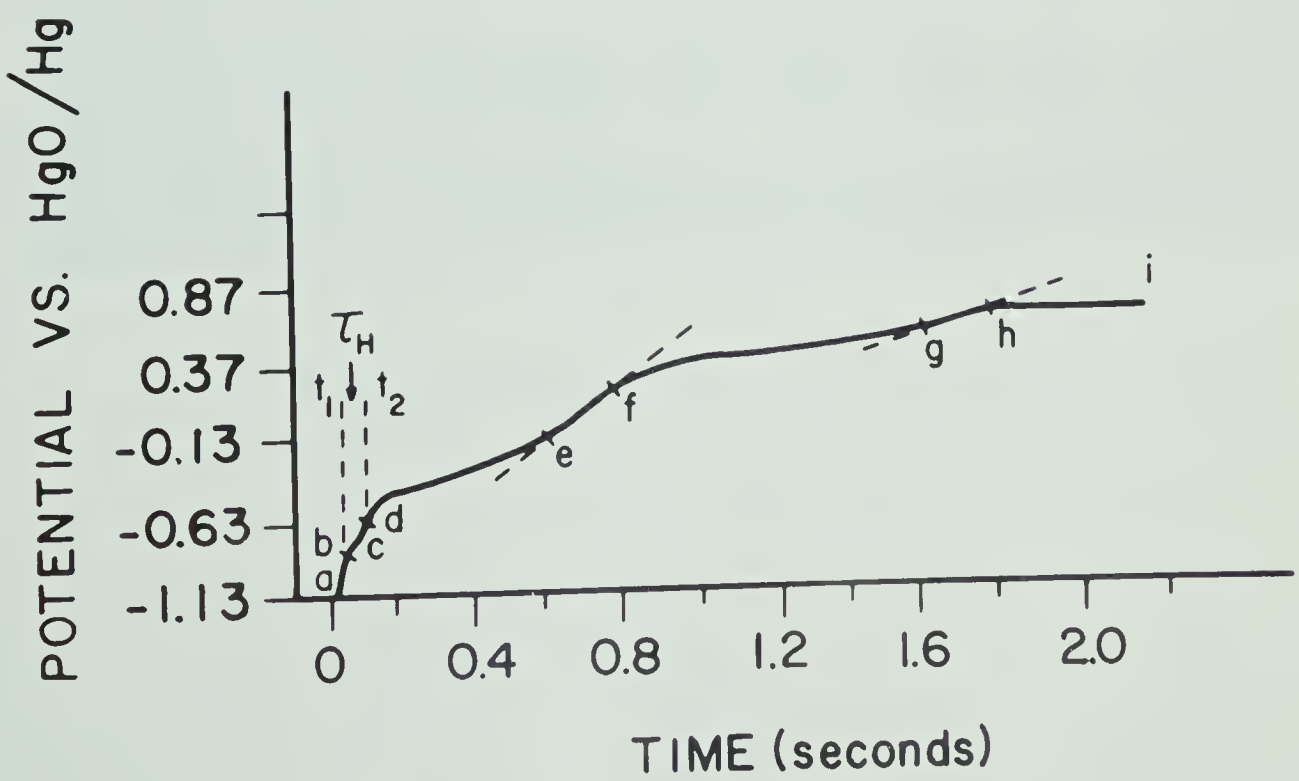

Fig. 27b. Illustration of 27a.

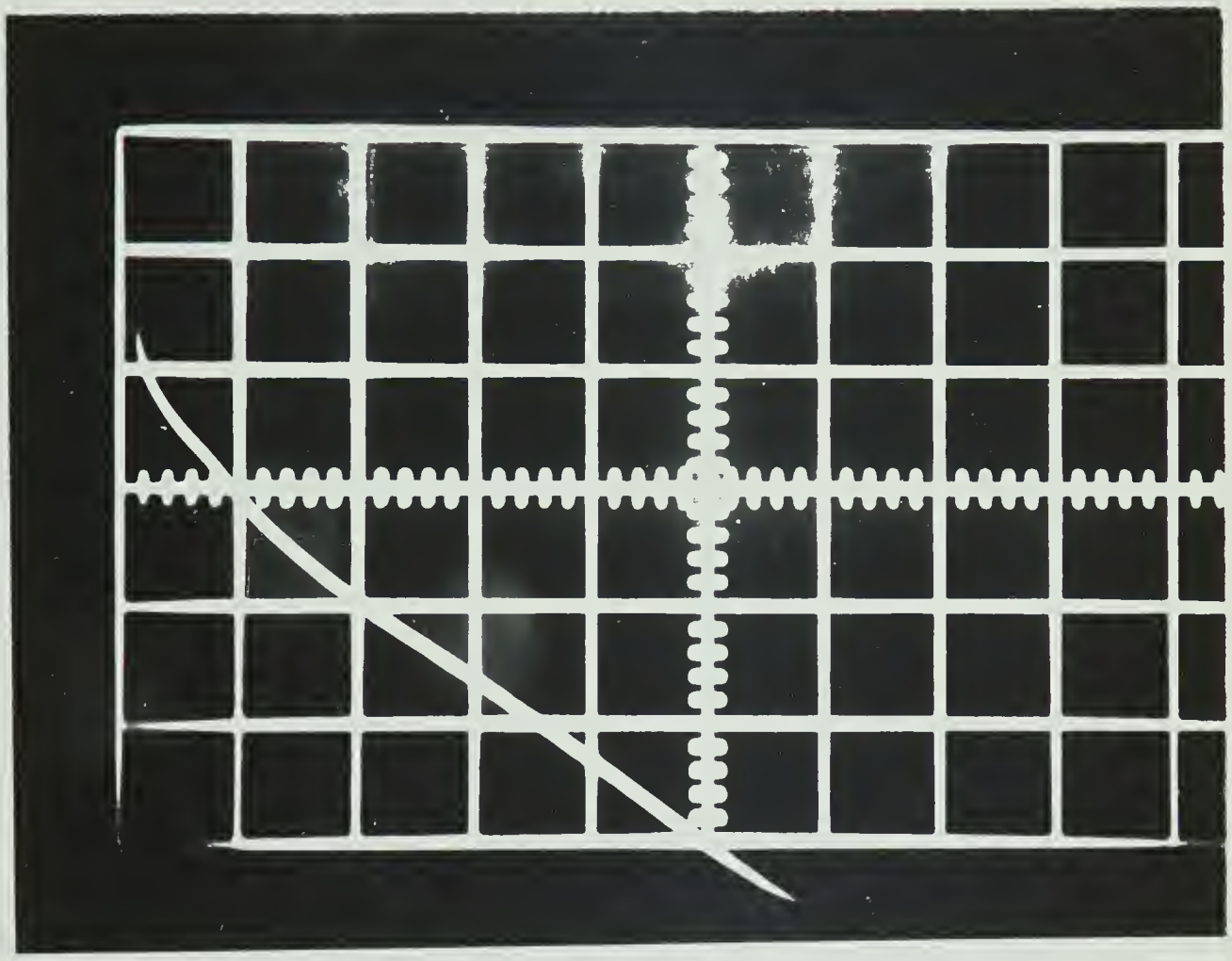

Fig. 28. Galvanostatic Stripping Transient
Same Conditions as Fig. 27a. Vertical Scale 200 mv/cm.

the section de of the transient. Formation of the similar oxides is probably indicated by interval fg, preceded by the double layer charging region ef. It follows that the evolution of oxygen occurred in the region hi, preceded by double layer charging region gh.

Fig. 27a shows a slow transient while Fig. 29 shows a fast transient obtained at a larger stripping anodic current density i_a.

Atomic Hydrogen Coverage From Galvanostatic Stripping Transients

If region bc in Fig. 27b corresponded to the ionization of atomic hydrogen produced during steady-state cathodic polarization, the coverage would be directly proportional to τ_H, the time required to ionize the atomic H is given by

$$Q_H = \int_{t_1}^{t_2} i_a dt = i_a(t_2 - t_1) = i_a \tau_H \qquad (95)$$

For example, τ_H in Fig. 28 was measured to be 5.8×10^{-3} sec. and the anodic current density of 96.1×10^{-3} amp./cm.^{2} was employed to produce the transient. As such

$$Q_H = 96.1 \times 10^{-3} \frac{\text{amp.}}{\text{cm}^2.} \times 5.8 \times 10^{-3} \text{ sec.} = 557 \frac{\mu \text{ Coulombs}}{\text{cm}^2.}$$

For a unit sq. cm. of electrode surface there are approximately 10^{15} metal atoms or sites. If one assumes that one H_2O molecule discharges onto one metal atom to form one reaction intermediate M-H, then a charge of about 640 μC of charges is necessary to form or to ionize a monolayer of M-H. Hence, the coverage θ_H can be calculated

$$\theta_H = \frac{Q_H}{640 \ \mu\text{C/cm}^2.} = \frac{557 \ \mu\text{C/cm}^2.}{640 \ \mu\text{C/cm}^2.} = 0.87$$

Table III

Hydrogen Coverage from Galvanostatic Stripping
(Anodic current density = 138.5 ma/cm^2.)

Potential vs. HgO/Hg (volt)	$\mu C/cm^2$ (±20%)	θ_H
-1.350	1500	2.3
-1.320	1250	2.0
1.300	1250	2.0
1.280	1250	2.0
1.250	1400	2.1
1.230	1400	2.1
1.20	1400	2.1
1.18	1400	2.1
1.16	1400	2.1
1.15	1400	2.1
1.12	1400	2.1
1.09	1400	2.4

The variation of θ_H with potential is listed in Table III where the anodic current density employed was 138.5 ma/cm^2. Since θ_H varied with the stripping current and θ_H is greater than unity in many cases as shown in Table III, then the θ_H measured by the method could not be true. This is evident as the double layer charging region cd (see Figs. 27 and 28) was not steep enough to separate the stages of the ionization of atomic hydrogen and the following oxidation process. Further support of the idea that θ_H measured by this method is not the true hydrogen coverage will be shown by the values obtained by the potential-step method discussed in the next section.

Interpretation of Current-Time Transients

A typical current-time trace is shown in Fig. 29a with an exaggerated illustration in Fig. 29b. Point b was the initial current supplied to the cell by the potentiostat. Four partial currents should be recognized at time t: (i) a portion used for charging the double layer, (ii) a portion for discharging H_2O to form reaction intermediate M-H, (iii) a fraction for dissolving some oxide film present on the metal surface, and (iv) a fraction for the evolution of H_2. The peak current was the result of the double layer charging[32]. After the double layer had been charged up, a decay of current was observed. As more and more oxide was dissolved, more and more atomic hydrogen was formed until the steady-state current was reached. In steady-state conditions the concentration of atomic hydrogen on the electrode surface is assumed constant (see Theory). The number of coulombs of electricity passed from initial time to time of steady-state current can be

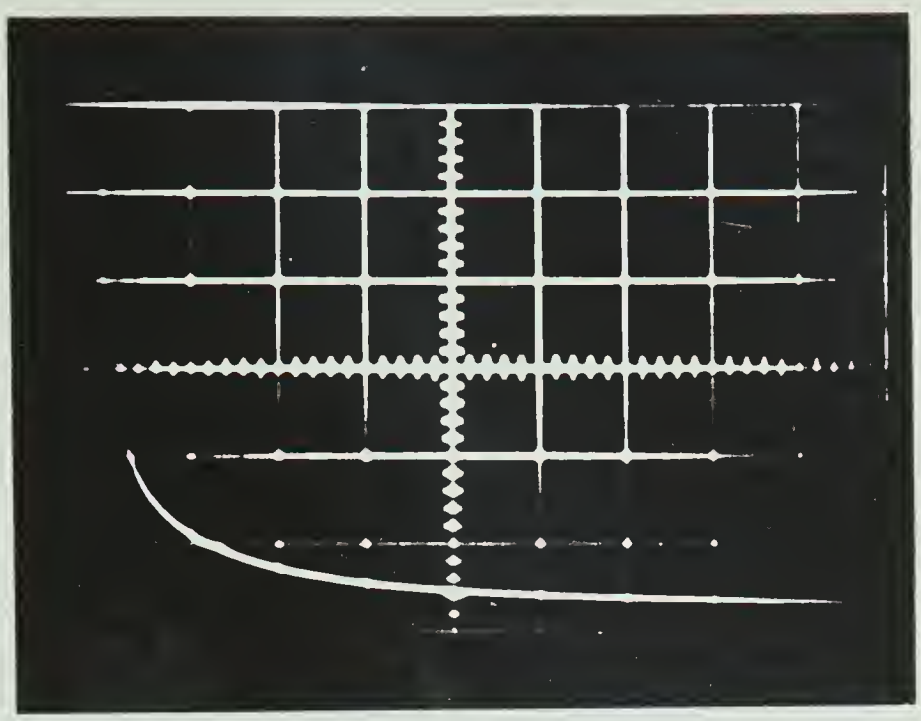

Fig. 29a. Current-Time Transient. ε = -0.950 vs. HgO/Hg
50 ma/cm.; 0.5 msec./cm.

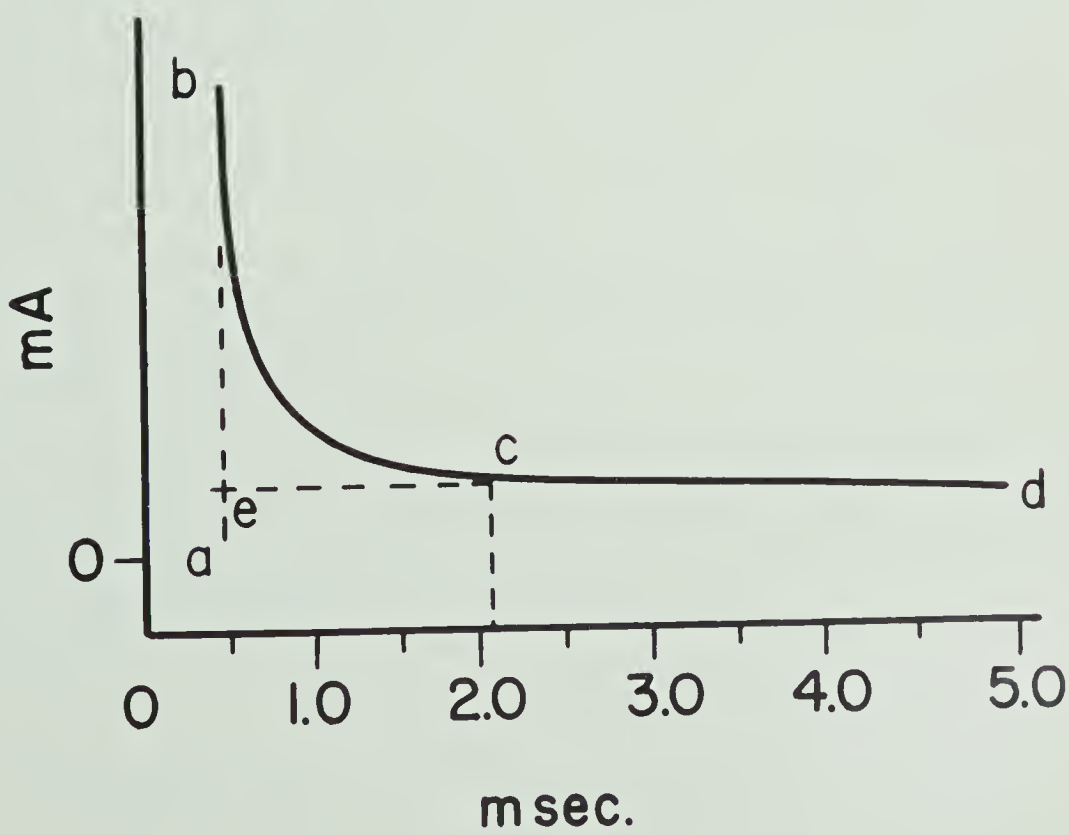

Fig. 29b. Illustration of 29a.

obtained by integration of the area bounded in ebc (see Fig. 29b),

$$Q = \int_{o}^{t} i dt \tag{96}$$

where Q can be partitioned into

$$Q = Q_{d.l.} + Q_{ox} + Q_{H} + Q_{H_2} \tag{97}$$

by the preceding discussion. On examining the galvanostatic charging transients (see Figs. 27 and 28), hydrogen evolution began at about -0.700 v. vs. 1.0 M NaOH/HgO/Hg (-0.60 vs. N.H.E.) for the stainless steel alkali system. Hence, the area under the peak for the -0.700 v. vs. HgO/Hg can be approximated as the sum of $Q_{d.l.}$ and Q_{ox}, which are the electricity required to charge up the double layer and to dissolve the oxide on the metal surface. For higher potentials, further amount of electricity used for charging the e.d.l.[48] and for dissolving the oxide can be neglected. Then equation (97) becomes

$$Q_{H} + Q_{H_2} = Q - Q_{-0.700} = Q - (Q_{d.l.} + Q_{ox}) \tag{98}$$

where Q is the number of coulombs measured under the i-t trace at more negative potentials.

The number of coulombs of electricity under the peaks were integrated with a K & E planimeter. The integration of the -0.700 v. and -0.950 v. peaks gave 6.8 and 42.4 $\frac{\mu C}{cm^2}$.

Hence

$$(Q_{H} + Q_{H_2})_{-0.950\ v.} = (42.4 - 6.8)\ \frac{\mu C}{cm^2} = 35.6\ \frac{\mu C}{cm^2} \tag{99}$$

If the rate of hydrogen evolution during the transient is assumed

constant and equal to the steady-state current density i_c at the designated potential -0.950 v., then Q_{H_2} can be evaluated

$$Q_{H_2} = \int_o^t i_c \, dt = i_c t$$

The steady-state current at -0.950 v. is 10^{-5} amp./cm^2. From Fig. 29a, t is 1.25 msec., then

$$Q_{H_2} = 10^{-5} \frac{\text{amp.}}{\text{cm}^2.} \times 1.25 \times 10^{-3} \text{ sec.} = .0125 \frac{\mu C}{\text{cm}^2.}$$

Hence, Q_{H_2} is negligible during the transient and this is true up to a potential of -1.400 vs. HgO/Hg. It follows that Q_H is equal to 42.4 $\frac{\mu C}{\text{cm}^2}$. The hydrogen coverage is calculated to be

$$\theta_H = \frac{Q_H}{640 \ \mu C} = \frac{42.4}{640} = 0.066$$

The variation of θ_H with potential is shown in Table IV and Fig. 30. The slope, $\frac{\partial \eta}{\eta \log \theta_H}$, obtained from the graph was -240 mv.

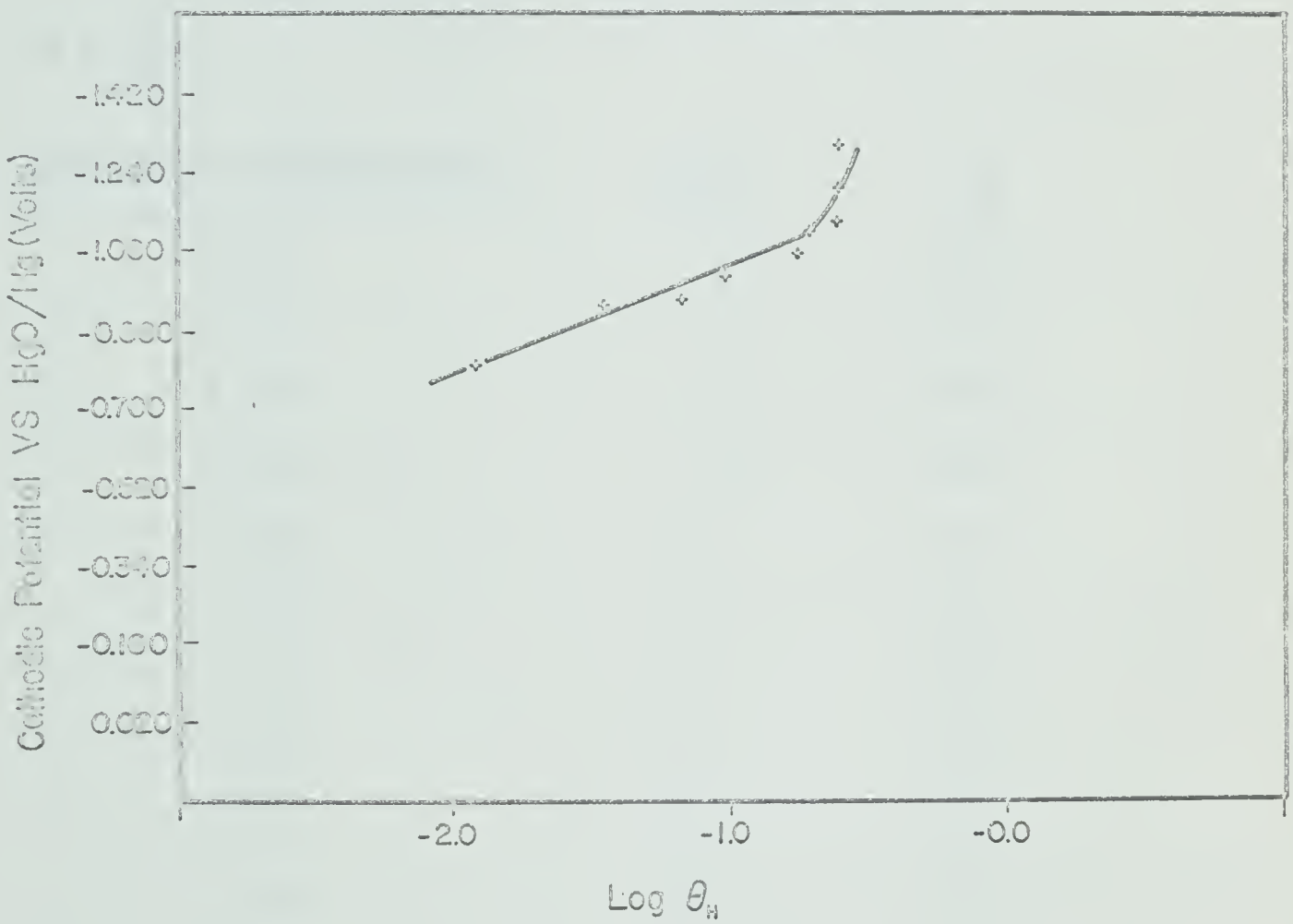

Fig. 30. Potential-Log θ_H Relationship

Table IV

Hydrogen Coverage by Potential-Step Method

1.0 M NaOH

Potential vs. HgO/Hg (volts)	$\mu C/cm^2$.	θ_H
-0.800	11.5	0.018
0.900	21.7	0.034
0.950	42.4	0.066
1.000	62.0	0.096
1.050	109	0.170
1.100	121	0.190
1.150	152	0.237
1.200	157	0.240
1.300	159	0.243
1.400	165	0.254

DISCUSSION

Surface State

The hydrogen evolution reaction at the stainless steel type 304 in strong sodium hydroxide solutions was found to be a highly irreversible phenomenon. The anomaly is that the cathodic polarization characteristics were entirely different from either Ni or Fe, two of the major components in the stainless steel alloy.

Tafel parameters exhibited by Ni[4], Fe[6], and s.s. 304 in 0.1 M NaOH solutions were collected and summarized in Table V. Unfortunately no data is available from the literature on the chromium cathode, which is the third major component present in the alloy. From Table V it can be seen that the overpotential η exhibited by the stainless steel cathode was much higher than that exhibited by Fe and Ni cathodes.

Fig. 31 shows the dependence of overpotential on the electrode material as derived by Conway and Bockris[61]. Two distinct groups of metal behaviour was found in the plot of overpotentials at a constant current density in 1.0 M HCl solutions versus the heats of adsorption of hydrogen on various metals. Transition metals such as Pt and Pd having a high % d-band character or low d-holes were found to have low M-H interaction energies. Having a low M-H interaction energy facilitates the discharge of protons or water molecules to form adsorbed M-H intermediates. For transition metals with low % d-band character or a high number d-band vacancies, the discharge of protons or water molecules to form M-H intermediates is more difficult. Hence, the discharge step should act as the

Table V

Comparison of Tafel Parameters in 0.1 M NaOH Solutions

Metal	b,v	a,v	i_o, $\frac{amp.}{cm^2}$	η, at 10^{-3} amp./cm^2.
Ni[26]	0.092	-0.487	1.2×10^{-5}	-0.176 vs. NHE
Fe[29]	0.120	-0.726	8.7×10^{-7}	
s.s. 304	0.134	-1.487	7.9×10^{-12}	-1.092 vs. NHE

Fig. 31. Dependence of Hydrogen Overpotential on Electrode Material

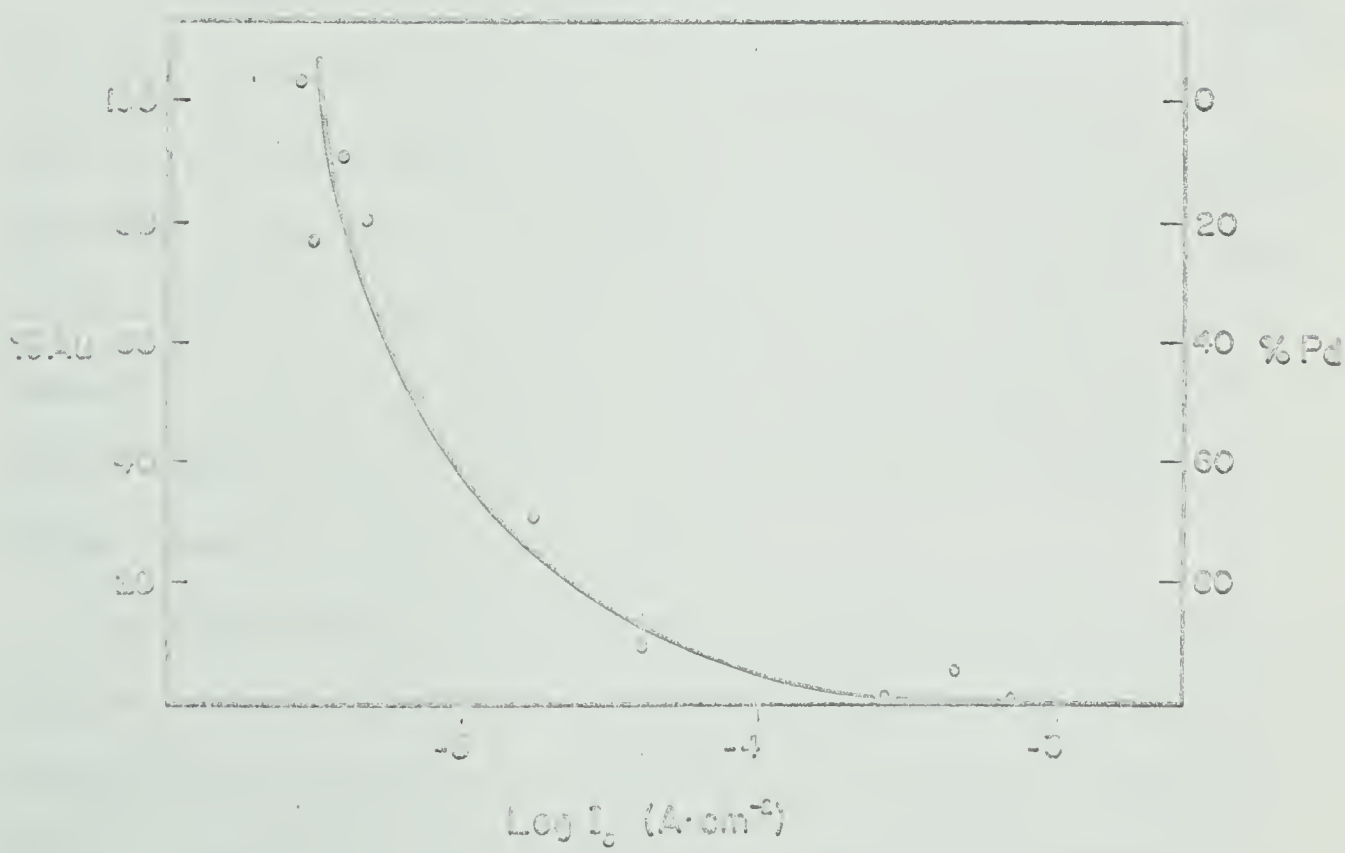

Fig. 32. Dependence of Exchange Current Density on Electrode Material

rate controlling step for the latter case. In the former case, the discharge of a proton or a water molecule should comprise the fast step in the h.e.r. mechanism.

On the other hand, non-transition metals behave entirely opposite to that of the transition metals. For example, Hg, which has a lower interaction energy, shows a higher overpotential than Tl.

A more effective way of explaining the concept of d-band character on the rate of hydrogen evolution has been shown[62]. The dependence of exchange current density as a function of % Au composition in a series of Au-Pd alloys is shown in Fig. 32. By decreasing the Au content of the alloy, the exchange current density decreased quite sharply until 60% Au. With further decreasing amount of Au content, the % d-band character increased more and more, resulting in an increase of the exchange current.

On the basis of the preceding discussion and on that of comparing the Tafel parameters with Ni and Fe, the stainless steel surface may have a non-transitional metallic or a very low % d-band character behaviour. According to Uhlig[63] Cr-Ni-Fe, Cr-Fe and Cr-Ni alloys containing 12% or more Cr content behave as pure Cr metal. On exposure to air or oxidizing solutions a passive oxide film is usually formed on the surface of the alloys and Cr. As such, no further chemical activity is displayed.

The nature and the mechanism of the formation of the passive film are generally disputed between the believers in the electron configuration theory and the believers in the chemical oxide-film theory. According to the former theory atoms of the elements Cr,

Ni, Co, Fe, etc., are characterized by incomplete inner shell (d electron) energy levels and by unfilled energy bands in the metallic state. The unfilled d energy bands tend to fill with electrons in the same sense that outer shells are completed in the formation of chemical compounds. The passive state is described as the condition of unfilled d bands in the metal or alloy, and the active state as that of the d band filled with electrons. Thus adsorbed oxygen or adsorbed oxidizing substances accompany maximum passivity because they are electron absorbers with no tendency to supply electrons to atoms of the metal surface.

In Cr-Ni-Fe alloys (stainless steels), the constituent Cr is most passive and is considered to impart this property to Ni and Fe by electron sharing which results from the stronger tendency of Cr to absorb electrons.

Regardless of the nature of the film, Uhlig[8] and Popat and Hackerman[64] suggested that the passive film should dissolve before or under cathodic hydrogen evolution conditions. However, after the stainless steel 304 metal surface was pickled with 1:1 acid mixture of HCl and H_2SO_4 and after a long time electrolysis, polarization curves carried out indicated an oxide film remained even after three normal experimental runs in the current density range $0.022 \times 10^{-3} - 25 \times 10^{-3}$ amp./cm.^{2}.

High Tafel slopes observed at the stainless steel-alkali interface also indicated the presence of a surface oxide film[65,66]. If the oxide film was of the usual type and of the usual thickness (greater than 30-50 A°), the total electrode capacity should be small (less than 10 μf/cm^2.)[64]. The range of capacities measured

in this work was 20-45 $\mu f/cm^2$. If the thin oxide film were a good electronic conductor, the capacity contribution to the total electrode capacity would be negligible[64].

Since the stainless steel type 304 included 18-20% Cr the alloy would be expected to behave like Cr metal[63], that is, a passive oxide film should exist on the alloy surface on exposure to air or oxidizing conditions. Pourbaix's diagram[67] showed that $Cr(OH)_2$ or CrO_2^- could exist at the potential and at the pH ranges covered in the present work. Similar potential-pH diagrams do not show the existence of any nickel or iron oxide under the same conditions. A potential-pH diagram for Cr is shown in Fig. 33. The presence of an oxide of any nature on the electrode surface would render the stainless steel a non-transition metallic character.

Gulbransen and Andrew[68] studied the kinetics of oxidation of Cr and found Cr_2O_3 formed under mild oxidizing conditions. Fig. 22 shows the effect of the addition of NH_4OH to 1.0 M NaOH solution in an attempt to partially dissolve any Cr_2O_3 present on the stainless steel surface. A slight increase in activity was found for the 0.1 M NH_4OH added.

Since nickel was the most active of the three major elements present in the stainless steel alloy, it was thought that only the Ni sites might be active in the hydrogen evolution reaction. Piontelli et al[69] carried out hydrogen overpotential measurements on various crystal planes of Ni and found that the most densely packed plane (1, 1, 1) had the highest activity. On the average, the interatomic distance of the Ni atoms on the stainless steel surface is 10-12 times that on a pure Ni surface. This large

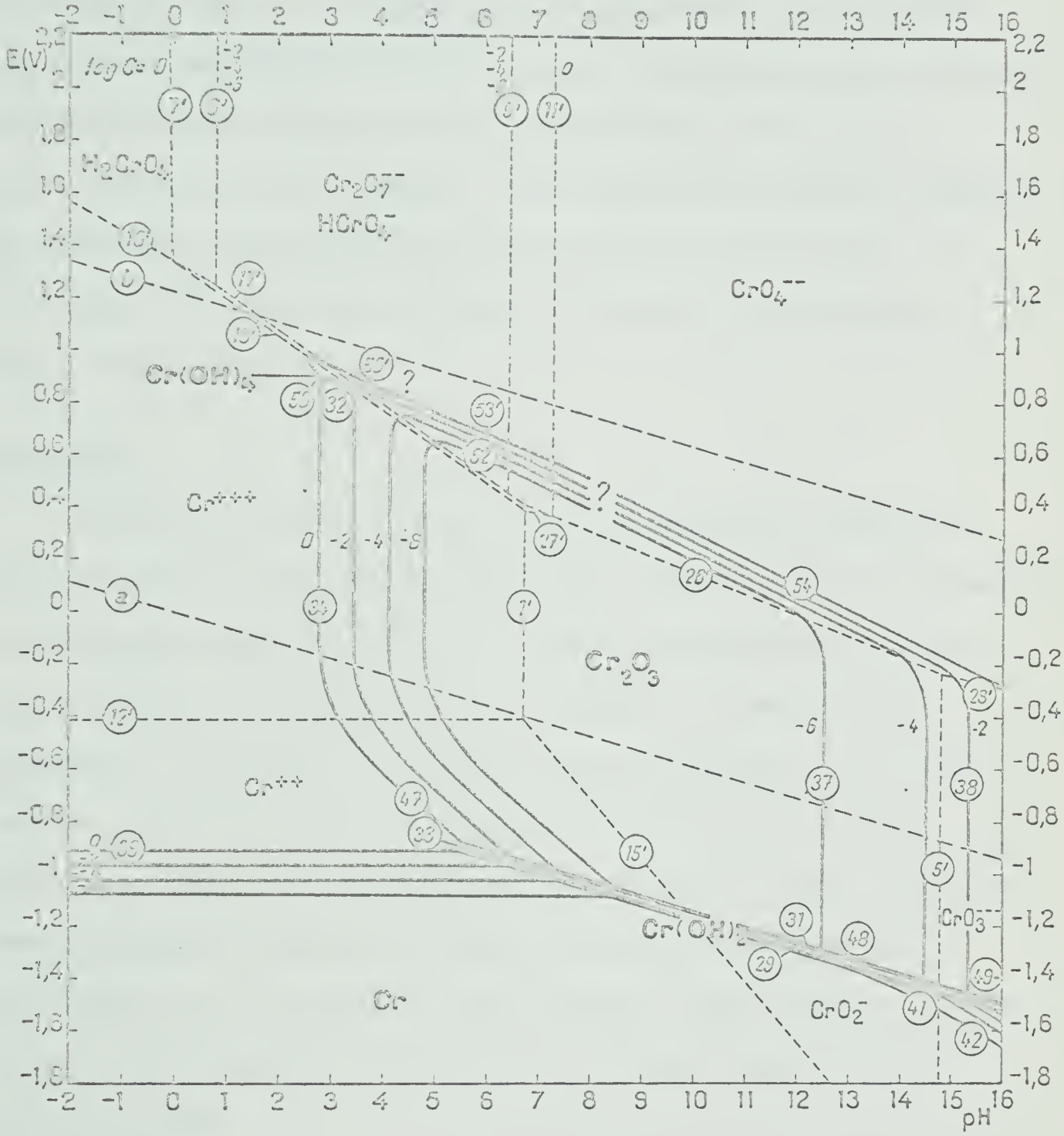

Fig. 33. Potential-pH Diagram For Chromium

interatomic distance may also explain the high polarization observed at the s.s. electrode. Polarization curves obtained after attempts to cover fractions of the surface with Fe or Ni by electrodeposition, is shown in Fig. 23. Although lower overpotentials were observed on surfaces deposited with these elements, the decrease was not enough to indicate that some part of the oxide surface had attained a pure metallic Fe or Ni surface. The elements were probably deposited as impurities and thereby the effective electrode areas were increased. The irregular behaviour of the Tafel curves seem to support this idea.

Mechanism

Either the discharge step, or the electrochemical desorption step, as the rate controlling reaction is compatible with the observed experimental slopes (see Table II). From the preceding discussion and also from the comparison shown in Table V, it would be unreasonable to classify the stainless steel electrode in the intermediate range of activity of hydrogen evolution in 0.1 M NaOH solutions, where both Fe and Ni belong. As such, a large activation energy should be required to form a M-H intermediate from the discharge of a H_2O molecule on the stainless steel surface. On this basis, it is reasonable to assign the discharge step as the rate controlling one.

The following step could be either fast Tafel recombination or fast electrochemical desorption. The stoichiometric number for mechanism (A) was defined as $\nu = 2$ and for mechanism (C) was defined as $\nu = 1$ (see Theory). Because corrosion occurred at lower

current densities, the stoichiometric number could not be determined for the present electrode-electrolyte system.

The values of differential electrode capacity obtained from dc charging, from decay curves and from TDR were very similar. No hint of any pseudocapacity existed. Hence, the mechanism could not be elucidated from capacity-potential profile.

It is generally recognized that the double layer effect could be studied in dilute alkali solutions. The theoretical variation of overpotential per decade change of pH was calculated to be -60 mv[5]. It is also recognized that the double layer effect was negligible for concentrated solutions. In the present work, a slight increase of overpotential was observed at high current densities and a larger increase was found at lower rates with increasing NaOH concentration (see Figs. 12-13).

Neutral salts such as NaF, NaCl, and NaI did not show any significant effect on the rates of hydrogen gas evolution. The anions F^-, Cl^- and I^- were probably not chemisorbed on the stainless steel surface. This is compatible with the recognized fact that the fluoride ion is never chemisorbed to any electrode surface in any electrode-electrolyte system. While Cl^- and I^- anions are known specifically to adsorb to electrode surfaces, both were probably repulsed by the highly negatively-charged metal surface. Of course, the presence of the passive metal-oxide on the surface should prevent the formation of any metal-halide anion chemical bond.

Although the addition of cations Ba^{+2} and La^{+3} showed a slight lowering of the hydrogen overvoltage (see Figs. 18-19), the decrease was not significant enough to render a quantitative interpretation

that the cation affects the rate of water discharge. The multivalent Ba^{+2} and La^{+3} ions are usually solvated and thus do not specifically adsorb to the electrode surface.

At high current studies, a limiting current density of about 4.5 amp./cm^2. was found (see Fig. 22). Similar polarization curves were found for Pt, Pd and Ni cathodes. Bockris and Azzam[2] found that for Pt in various HCl solutions, Tafel slopes changed from 30 mv. to 140 mv. at 20-70 amp./cm^2. Also in HCl, a change of Tafel slope from 30 mv. to infinity at 30 amp./cm^2. and 10 amp./cm^2. for Pd and Ni cathodes, respectively were found. Bockris and Potter[5] also found that the Tafel slope changed from 120 mv. to infinity at 10 amp./cm^2. for Ni in NaOH solutions. The phenomenon of the limiting current density was explained as the maximum rate at which the atomic hydrogen recombination reaction can take place. The kinetics of the h.e.r. could have been modified by the emergence of an alternative path or by changes in the energy of hydrogen adsorption at high coverages[5]. The shift of the Tafel slope from 30 mv. to 140 mv. for Pt probably changed the mechanism from (B) to either a rate controlling slow discharge or a rate controlling electrochemical desorption. Bockris and Azzam thought that the latter was more probable because it functioned in the steady state with the electrode surface highly covered with hydrogen atoms. For Ni a shift from mechanism (A) to a rate controlling electrochemical desorption mechanism was also concluded[5]. On the basis of a limiting current density found for the stainless steel-sodium hydroxide system, the mechanism of the h.e.r. is a slow discharge-fast Tafel recombination:

$$H_2O + M + e \overset{\text{slow}}{\rightleftharpoons} M\text{-}H + OH^-$$

$$M\text{-}H + M\text{-}H \xrightarrow{\text{fast}} 2M + H_2$$

Whether or not the mechanism changes, the limiting current density indicates that the maximum rate of recombination of H atoms has been reached.

Fig. 31 shows the potential-log θ_H relationship and a slope, $\frac{\partial\eta}{\partial \log \theta_H}$ = 240 mv., obtained by the potential-step method. This provides a quantitative criterion for the elucidation of the h.e.r. Recall equation (51) and include the activity of the metal

$$\theta_H = \left[\frac{k_1 a_M}{2k_2}\right]^{1/2} \exp\left[\frac{-z\alpha F\eta}{2RT}\right] \tag{51}$$

Rewriting it in logarithm form

$$\log \theta_H = \log \left[\frac{k_1 a_M}{2k_2}\right]^{1/2} - \frac{z\alpha F\eta}{2 \times 2.303\ RT} \tag{90}$$

it can be rearranged to give

$$\eta = \frac{2 \times 2.303\ RT}{z\alpha F} \log \left[\frac{k_1 a_M}{2k_2}\right]^{1/2} - \frac{2 \times 2.303\ RT}{z\alpha F} \log \theta_H \tag{91}$$

Putting T = 308°K, z = 1, and α = 1/2, it follows that

$$\frac{\partial\eta}{\partial \log \theta_H} = -\frac{2 \times 2.303\ RT}{z\alpha F} = -0.244\ \text{v.} \tag{92}$$

The experimental slope of -0.240 v. agreed very well with the theoretical potential-log θ_H variation for slow discharge-fast Tafel recombination mechanism.

Calculation of Specific Rate Constants and Free Energies of Activation

With the mechanisms of h.e.r. firmly established as slow discharge-fast recombination, the specific rate constants (k_1 and k_2) and the free energies of activation (ΔG_1^*, and ΔG_2^*) can be calculated. Recall equation (55)

$$\eta = \frac{2.303\ RT}{z\alpha F} \log Fk_1 + \frac{-2.303\ RT}{z\alpha F} \log i_c \qquad (55)$$

It can be rewritten to include the terms a_M, the activity of the metal

$$\eta = \frac{2.303\ RT}{z\alpha F} \log Fk_1 a_M + \frac{-2.303\ RT}{z\alpha F} \log i_c \qquad (93)$$

or $\eta = a - b \log i_c$

From Table II, the value of a is -1.503 v., the potential at $i_c = 1$ amp./cm^2. Hence

$$a = -1.503 = \frac{2.303\ RT}{z\alpha F} \log Fk_1 a_M \qquad (94)$$

It follows that

$$k_1 = \frac{1}{Fa_M} 10^{\frac{-1.503 \times z\alpha F}{2.303\ RT}} \qquad (95)$$

If the activity coefficient of the metal is unity, then

$$k_1 = \frac{1}{Fc_M} 10^{\frac{-1.503 \times z\alpha F}{2.303\ RT}} \qquad (96)$$

where c_M is the concentration of metal atoms, present on the electrode surface. Substituting $c_M = 10^{-9}$ g-atoms/cm^2., $\frac{2.303\ RT}{z\alpha F} = 0.133$ (see Table II) and F = 96,500 coulombs, then $k_1 = 5 \times 10^{-8}$.

From the absolute reaction rate theory the rate constant k_1 is related to the free energy of activation ΔG_1^* by

$$k_1 = \frac{kT}{h} \exp \left[\frac{-\Delta G_1^*}{RT} \right] \tag{97}$$

where k is the Boltzmann constant and h the Planck constant. Rearranging, (97) becomes

$$\Delta G_1^* = -2.303 \text{ RT} \log \frac{k_1 h}{kT} \tag{98}$$

Putting T = 308°K, h = 6.62×10^{-27} erg. sec., and k = 1.38×10^{-16} erg./deg. ΔG_1^* has the value of about +28 kcal./mole.

At limiting current density, the electrode surface is assumed to be covered by a monolayer of atomic hydrogen ($\theta_H = 1$). Hence the concentration of atomic hydrogen at unit coverage is 10^{-9} g-atoms/cm^2. Equation (52) can be rewritten

$$i_L = 2Fk_2 C_H^{\ 2} \tag{99}$$

It can be rearranged to

$$k_2 = \frac{i_L}{2FC_H^{\ 2}} \tag{100}$$

Putting in the values i_L = 4.5 amp./cm^2. (see Fig. 22), $C_H = 10^{-9}$ mole/cm^2. and F = 96,500 coulombs, k_2 has the value of about 2.3×10^{13}. The corresponding free energy of activation is -0.78 kcal./mole. This value agrees with the fact that little or no activation energy is needed for surface radical reactions[2].

The values of k_1 (5×10^{-8}) and of k_2 (2.3×10^{13}) give further evidence to the previous conclusion that the mechanism of h.e.r. at stainless steel 304-sodium hydroxide solution interface is a slow discharge of water molecule followed by fast atomic hydrogen recombination.

APPENDIX I

Time Domain Reflectometry - A New Method of Measuring Electrical Double Layer Capacities

Introduction

Many methods have been used to determine the electrical double-layer capacity at an electrode-electrolyte interface. Some are applicable only to certain types of electrodes and others do not give either precise or accurate results. The a.c. bridge technique, so successfully developed and applied by Grahame[52] to the dropping mercury electrode, cannot be applied to solid electrodes since their C_{dl}'s are usually frequency dependent[53, 54]. Systems other than bridge techniques have been developed for solid electrodes.

Morley and Wetmore[55] evolved the equation describing open-circuit potential decay transients. Double galvanostatic pulse charging was developed by Devanathan et al[46]. A similar group[56] employed a rapid upward change in electrode potential. Vetter has summarised and discussed the use of potential step transients in a recent monograph[32]. Only the a.c. bridge and the potential step methods avoid the problem of geometrical differentiation of the potential time traces at zero time in the charging process. The inaccuracies inherent in the slope determination mean inaccurate capacities. In an attempt to solve this problem, Angerstein-Kozlowska and Conway[57] obtained the reciprocal of the C_{dl} by electronically differentiating oscillographs of potential-time transients.

Time domain reflectometry (TDR) will be presented in this paper as a convenient new method of obtaining more accurate electrical double-layer data. Experiments are very easy to set up and perform, and calculations are simple to make.

TDR involves sending an extremely fast rise (~ 90 p secs) step voltage pulse of known height from a pulse generator down a transmission line to the electrode being studied. The TDR circuit is completed via a special auxiliary electrode. From the theory of propagation of electrical signals in transmission lines, reflections result. The incident and reflected waves are monitored by an oscilloscope. An electrical analogue is assumed for the electrode impedances. The electrode capacities, solution resistances and the polarization resistances are then elucidated from a set of derived equations.

Electrode capacities obtained by the TDR method will be compared with those obtained by the current interrupter and the galvanostatic stripping methods on a stainless steel electrode.

Theory

Time domain reflectometry can best be understood by considering the theory of propagation of energy down a transmission line.

The classical transmission line is assumed to be made up of a continuous structure of resistances, conductances, inductances and capacitances[58]. If the line is infinitely long the R's, G's, L's and C's are defined per unit length, then the characteristic impedance of the line is

$$Z_o = \frac{R + j\omega L}{G + j\omega C} \qquad (1)$$

ω is in radians and $(j)^2 = -1$.

A voltage introduced at a generator requires a finite time to traverse the line to a point x. As the voltage moves down the line, it will experience a phase lag compared to the voltage at the generator of an amount β per unit length because of the inductances and capacitances. At the same time, the voltage is attenuated by an

amount α per unit length by the series resistances and shunt conductances of the transmission line. The phase shift and attenuation are defined by the propagation constant γ.

$$\gamma = \alpha + j\beta \tag{2}$$

or $$\gamma = (R + j\omega L)(G + J\omega C) \tag{3}$$

The velocity at which the voltage travels down the line is

$$v_p = \frac{\omega}{\beta} \tag{4}$$

and the velocity of propagation is

$$v_p = \frac{v_c}{\varepsilon} \tag{5}$$

where v_c is the velocity of light in vacuum and is the dielectric constant. The voltage at any point x is written in terms of the initial voltage as

$$E_x = E\, e^{-\gamma x} \tag{6}$$

and the analogous expression for the current is

$$I_x = I\, e^{-\gamma x} \tag{7}$$

Now $$Z_o = Z_{initial} = \frac{E\, e^{-\gamma x}}{I\, e^{-\gamma x}} = \frac{E}{I} \tag{8}$$

When an electric wave is travelling down a transmission line, there is an exact balance between the electric and magnetic fields[59]. Half of the energy of the waves is in the electric field and half is in the magnetic field. If the wave encounters a different medium characterized by a different impedance, there is a new distribution of energy. Since no energy could be added to the wave, the new balance must be achieved by rejecting some of the impinging energy. This rejected energy constitutes a reflected wave. The above equations can be satisfied and yet no reflection occur if the load impedance,

Z_L, is equal to the transmission line impedance. In the case of a miss-match of impedances of the two circuit sections, the equations are satisfied if the rejected energy is considered to be a second wave originating at the load and propagating back up the line to the generator. The energy balance is then analogous to a bridge balance and the reflection coefficient is defined as

$$\rho = \frac{E_r}{E_i} = \frac{Z_L - Z_o}{Z_L + Z_o} \tag{9}$$

where E_r and E_i are the reflected and incident voltages respectively.

To apply the above to an electrochemical problem, let us construct an electrical analogue. Suppose a load as treated above consists of a capacitor C (to be the edl capacity) in parallel with a resistance R_p (which will become the polarization resistance) and another resistance R' (which will represent the solution resistance) is put in series with the shunted elements. The system is then as shown in Figure 34. If the elements in such a system are linear, then it satisfies both the principle of superposition and the principle of homogeneity[60]. If the values of R_p, C and R' do not change with time, the system is time-invariant. It is also a continuous-time system because none of the responses resulting from any input is held constant. Linear, continuous, time-invariant systems can be described by linear differential equations. The Laplace transforms change the differential equation to an algebraic equation. The initial conditions are then introduced automatically and absorbed into the algebraic expression. Once the algebraic equation is found and the initial conditions included, the algebraic equation can be transformed back to the time domain to obtain the required time solution.

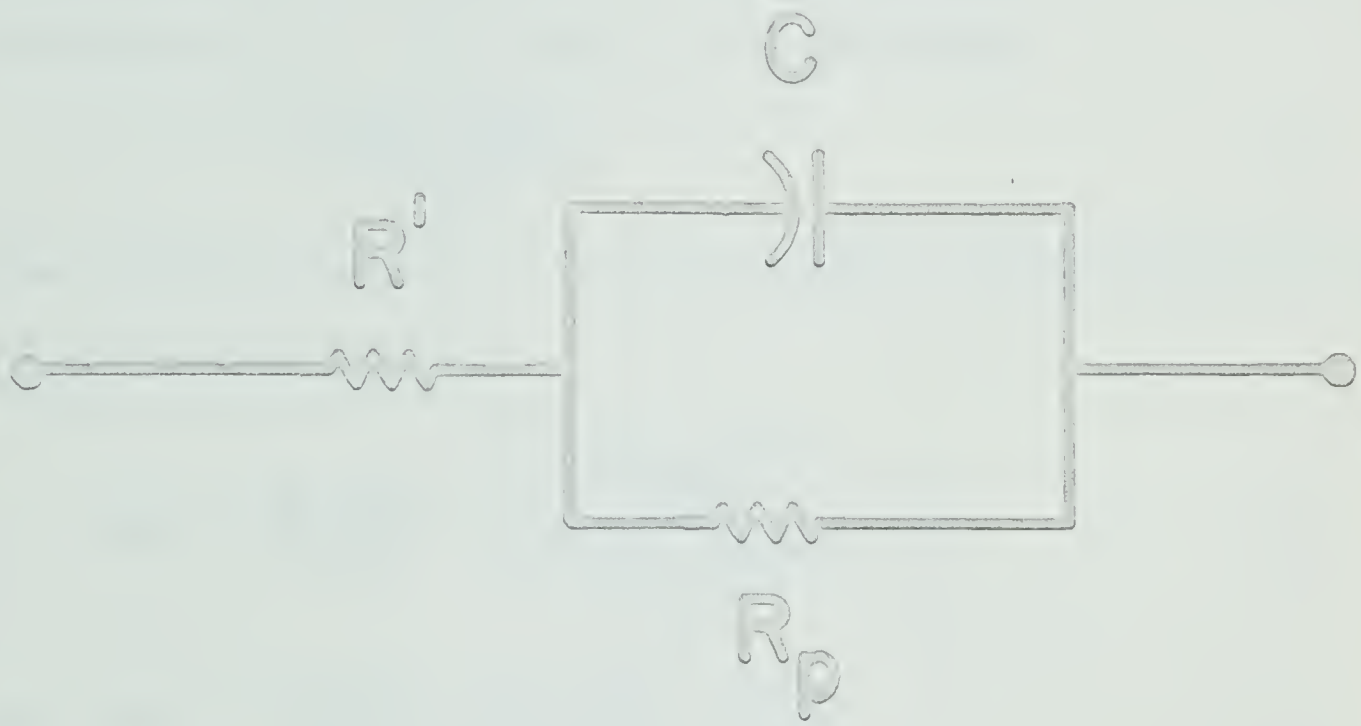

Fig. 34. Synthetic Circuit

By inspection, the impedance of the load shown in Figure 34 is

$$Z_L = \frac{R_p}{1 + j\omega R_p C} + R' = \frac{R' + R_p + j\omega R' R_p C}{1 + j\omega R_p C} \qquad (10)$$

Response of the system under sinusoidal steady state conditions can be determined by substituting

$$s = j\omega \qquad (11)$$

This implies that the imaginary axis is being traversed on the s-plane described by $s = \alpha + j\omega$. Equation (10) thus becomes

$$Z_L = \frac{R' + R_p + R' R_p Cs}{1 + R_p Cs} \qquad (12)$$

The reflection coefficient becomes a function of s with the substitution of equation (12) into (9).

$$\rho(s) = \frac{Z_L - Z_o}{Z_L + Z_o} = \frac{\dfrac{R' + R_p + R' R_p Cs}{1 + R_p Cs} - Z_o}{\dfrac{R' + R_p + R' R_p Cs}{1 + R_p Cs} + Z_o} \qquad (13)$$

$$\text{or} \quad \rho(s) = \frac{R_p + R' - Z_o + R_p(R' - Z_o)Cs}{R_p + R' + Z_o + R_p(R' + Z_o)Cs} \qquad (14)$$

The response of the load Z_L to the step voltage is obtained by multiplying $\rho(s)$ by the transofrm of the step voltage, $\frac{E_i}{s}$. Finally, the initial condition $\frac{E_i}{s}$ is add

$$F(s) = \frac{E_i}{s} + \frac{E_i}{s} \quad (s) \qquad (15)$$

and substituting equation (14) in gives

$$F(s) = \frac{E_i}{s} + \frac{E_i}{s} \quad \frac{R_p + R' - Z_o + R_p(R' - Z_o)Cs}{R_p + R' + Z_o + R_p(R' + Z_o)Cs} \qquad (16)$$

The inverse Laplace transform is then employed to revert this equation to an expression $v_r(t)$, described in the time domain

$$v_r(t) = L^{-1} \quad F(s) \quad = L^{-1}\left\{ \frac{E_i}{s} + \frac{E_i}{s} \frac{R_p + R' - Z_o +}{R_p + R' + Z_o +} \frac{R_p(R' - Z_o)Cs}{R_p(R' + Z_o)Cs} \right\} \quad (17)$$

The solution of (17) can be obtained only if the second term is simplified by the partial fraction method. Considering the second term only, let

$$\frac{A}{s} + \frac{B}{R_p + R' + Z_o + R_p(R' + Z_o)Cs} = \frac{1}{s} \frac{R_p + R' - Z_o + R_p(R' - Z_o)Cs}{R_p + R' + Z_o + R_p(R' + Z_o)Cs} \quad (18)$$

where A and B are coefficients. Then

$$(R_p + R' + Z_o)A = R_p(R' + Z_o)CAs + Bs = (R_p + R' - Z_o) + R_p(R' - Z_o)Cs \quad (19)$$

Collecting like terms, coefficient A has the value

$$A = \frac{R_p + R' - Z_o}{R_p + R' + Z_o} \quad (20)$$

and coefficient B

$$B = R_p(R' - Z_o)C - R_p(R' + Z_o)C \quad \frac{R_p + R' - Z_o}{R_p + R' + Z_o} \quad (21)$$

Equation (17) then becomes

$$v_r(t) = L^{-1}\left\{ E_i \quad \frac{1}{s} + \frac{R_p + R' - Z_o}{R_p + R' + Z_o} \frac{1}{s} + R_p(R' - Z_o)C - R_p(R' + Z_o) \frac{R_p + R' - Z_o}{R_p + R' + Z_o} \quad \frac{1}{R_p + R' + Z_o + R_p(R' + Z_o)Cs} \right\} \quad (22)$$

Dividing $R_p(R' + Z_o)C$ into the last term

$$v_r(t) = L^{-1}\left\{ E_i\left[\frac{1}{s} + \frac{R_p + R' - Z_o}{R_p + R' + Z_o}\,\frac{1}{s} + \right.\right.$$

$$\left.\left. \frac{R' - Z_o}{R' + Z_o} - \frac{R_p + R' - Z_o}{R_p + R' + Z_o}\,\frac{1}{s + \dfrac{R_p + R' + Z_o}{R_p(R' + Z_o)C}} \right]\right\} \tag{23}$$

which simplifies to

$$v_r(t) = L^{-1}\left\{ E_i\left[\frac{1}{s} + \frac{R_p + R' - Z_o}{R_p + R' + Z_o}\,\frac{1}{s} + \right.\right.$$

$$\left.\left. \frac{R' - Z_o}{R' + Z_o} - \frac{R_p + R' - Z_o}{R_p + R' + Z_o}\,\frac{1}{s + \frac{1}{\tau}} \right]\right\} \tag{24}$$

where $$\tau = \frac{R_p(R' + Z_o)C}{R_p + R' + Z_o} \tag{25}$$

Introducing the identities

$$L^{-1}\left\{ \frac{1}{s} \right\} = 1 \tag{26}$$

and $$L^{-1}\left\{ \frac{1}{s + \frac{1}{\tau}} \right\} = e^{\frac{-t}{\tau}} \tag{27}$$

gives

$$v_r(t) = E_i\left[1 + \frac{R_p + R' - Z_o}{R_p + R' + Z_o} + \frac{R' - Z_o}{R' + Z_o} - \frac{R_p + R' - Z_o}{R_p + R' + Z_o} \right] e^{\frac{-t}{\tau}} \tag{28}$$

By examining the boundary conditions of this equation, it should be possible to determine the magnetude and nature of the wave form. At time t = o, (28) becomes

$$v_r(o) = E_i\left[1 + \frac{R_p + R' - Z_o}{R_p + R' + Z_o} + \frac{R' - Z_o}{R_p + Z_o} - \frac{R_p + R' - Z_o}{R_p + R' + Z_o} \right] \tag{29}$$

which reduces to

$$v_r(o) = E_i \left(\frac{2R'}{R' + Z_o} \right) \tag{30}$$

At time t = ∞, (28) becomes

$$v_r(\infty) = E_i \left(1 + \frac{R_p + R' - Z_o}{R_p + R' + Z_o} \right) \tag{31}$$

which simplifies to

$$v_r(\infty) = E_i \frac{2(R_p + R')}{R_p + R' + Z_o} \tag{32}$$

The typical oscillograph wave form obtained is shown idealized in Fig. 35.

At time t = o, charge will begin to flow into capacitor C and the shunted elements in Fig. 34 act as a short circuit. It follows that at this point the effective load impedance is $Z_L = R'$. As the capacitor becomes more fully charged, the load impedance increases exponentially according to the time constant of the system, Z, resulting in an exponentially increasing voltage display. When the capacitor becomes fully charged at infinite time, the load impedance becomes large and the voltage levels off to a constant value as determined in equation (32).

Application to the H.E.R. at a Stainless Steel (304) Electrode

The results of the preceding discussion can be used to determine the electrode capacity resulting from charge transfer in the electrolytic evolution of hydrogen. The h.e.r. mechanism at the stainless steel 304 electrode in strong NaOH solution is slow discharge of the water

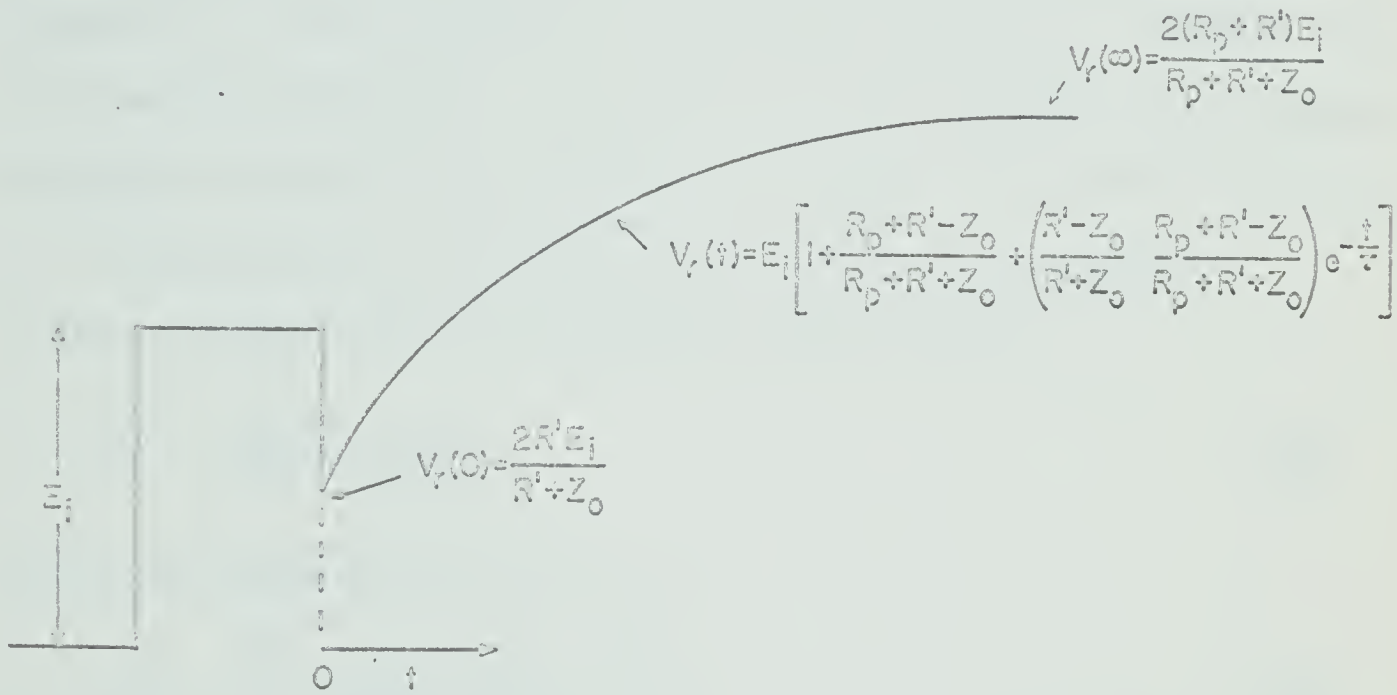

Fig. 35. Theoretical TDR Display

molecule followed by fast atomic hydrogen recombination (see Discussion in the main text).

When the exchange current density is low (about 10^{-12} amp/cm.^{2}), the equivalent circuit for such is[48] that shown in Fig. 34 without R'. If the step voltage is made to pass between the working electrode and an auxiliary electrode, a solution resistance, R', exists between the two electrodes. If the area of the auxiliary electrode is made much larger than that of the working electrode, its impedance can be neglected[10], which results in the circuit in Fig. 34. Assuming that the electrode parameters C, R_p and R' are linear elements, the equations developed previously can be applied to evaluate the solution resistance R', the polarization resistance R_p and the electrode capacity C. First R' is evaluated by rearranging equation (30) to

$$R' = \frac{v_r(o)}{2E_i - v_r(o)} Z_o \tag{33}$$

and R_p by rearranging equation (32)

$$R_p = \frac{(R' + Z_o)\, v_r(\infty) - 2R'E_i}{2E_i - v_r(\infty)} \tag{34}$$

The time constant is obtained by dividing the time to reach half the potential at full charge T by 0.693 and equating this to the equation given for τ (equation (25))

$$\tau = \frac{T}{0.693} = \frac{R_p(R' + Z_o)C}{R_p + R' + Z_o} \tag{35}$$

which can be rearranged for C

$$C = \frac{R_p + R' + Z_o}{R_p(R' + Z_o)} \quad \frac{T}{0.693} \tag{36}$$

which completes the extraction of the double layer capacity.

Experimental

Two geometrical arrangements were used. In both cases, the counter electrode was about one square inch of Pt, 1/2 of which was platinum black and 1/2 smooth platinum. The luggin capillary led to the half cell 1.0 M NaOH/HgO/Hg which was used to measure all cathodic potentials of the working electrode. The working electrode, made from stainless steel type 304 wire 1/32 inch diameter, was heat drawn to 0.036 cm to give an apparent electrode area of 0.001 cm^2 an area necessary in order that $v_r(\infty)$ could be found from the oscilloscope on a 10 μsec time base with a further offset of 10 μsec. The drawn wire was forced into teflon spaghetti rod and mechanically polished on 2/0 and 4/0 emery paper.

Both geometrical arrangements had the polarizing electrode, and the luggin capillary and reference cell (1.0 M NaOH/HgO/Hg) in the same relative positions. Only the TDR circuit was varied. One arrangement used and referred to here as the parallel arrangement, was the auxiliary (TDR) electrode, all of whose components were stainless steel type 304, and which consisted of 1-1/4 inch diameter, 1/8 inch thick discs separated by 1/4 inch and held by a small pin. The electrical leads were a small diameter rod. The working electrode was inserted through a hole in the upper disc so that its working face was about 1 mm from the auxiliary electrode surface and the working surfaces were parallel to obtain a minimum solution resistance.

In the perpendicular (90°) arrangement, the auxiliary electrode was placed alongside the working electrode so that their surfaces were at 90° to each other. Although this system had a higher solution resistance, its geometry is less complicated from both capacitance

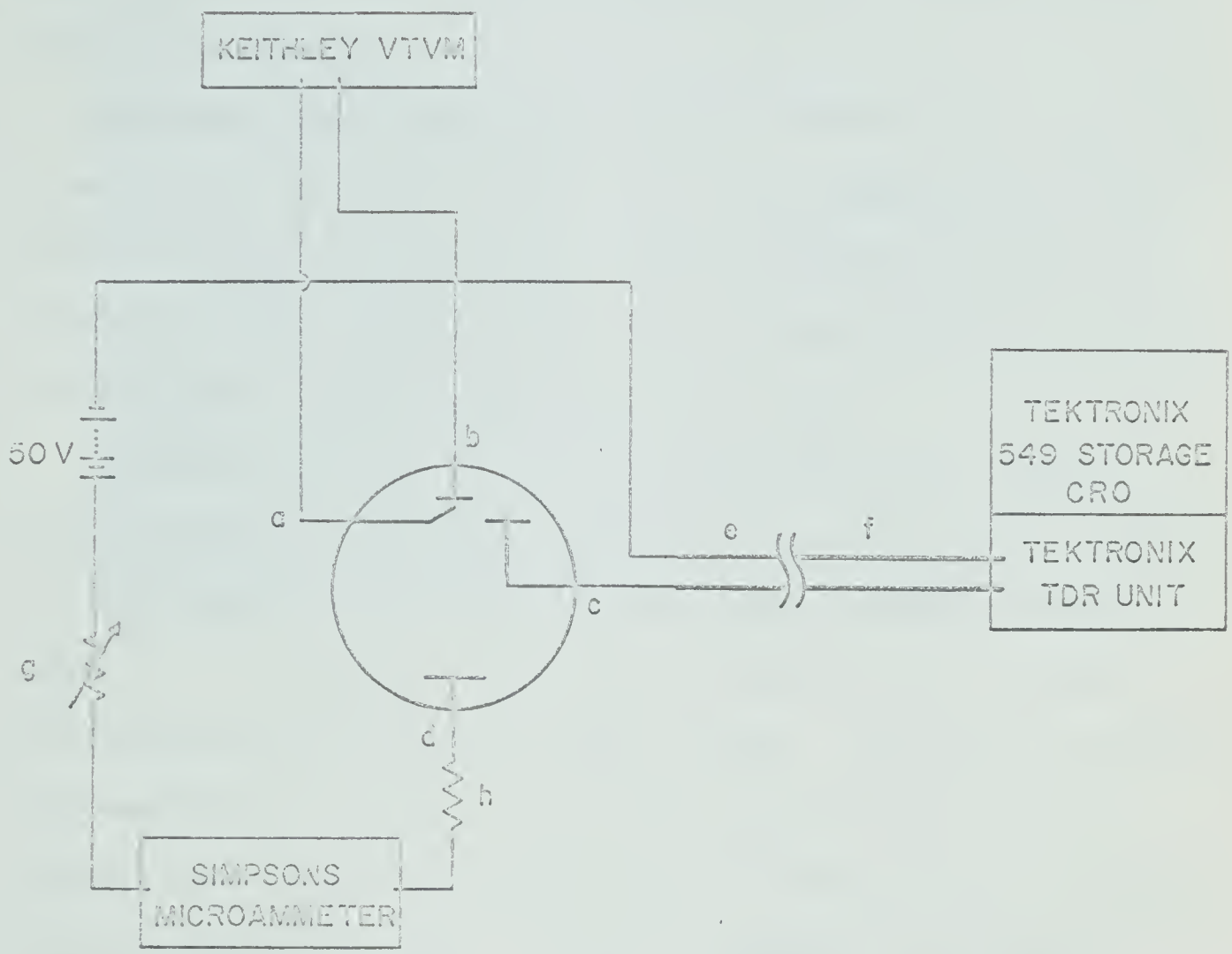

a Reference electrode
b Working electrode
c Auxiliary electrode
d Counter electrode
e 3 1/2 ft. RGA/u cable
f 100 ft. RGA/u cable
g Variable resistance
h Standard resistor

Fig. 36. TDR and Polarizing Circuit

and potential distribution points of view.

Both the Hewlett-Packard 1415 A TDR unit and Tektronix 1S2 sampling unit (TDR plug-in) with the Tektronix 549 storage oscilloscope were used, but all data here reported was obtained with the Tektronix equipment.

The same glass electrochemical cell was employed (see Experimental in main text). A tightly fitting teflon cap carrying the auxiliary, pre-electrolysis and working electrodes isolated the cell from the atmosphere. Same cleaning, deaeration, and pre-electrolysis procedures were employed. One molar NaOH solution was used.

Cathodic polarization of the working electrode was effected via the counter electrode by a constant current source which consisted of a high capacity 90 volt battery and a resistance box, as shown in Figure 36. The cathodic potentials were measured with a Keithley 660 differential vacuum tube voltmeter (VTVM). Polarization currents were measured with a Simpson microammeter or calculated from the potential drop (measured by VTVM) across a standard resistor inserted in the polarization circuit. To avoid an impedance contribution from the VTVM, it was detached when the TDR circuit was in use connecting the working and auxiliary electrodes. Similarly, the TDR circuit was disconnected while the overvoltage was being measured.

The working and auxiliary electrodes were connected to the output of the pulse generator on the 1S2 sampling unit (TDR) by 3-1/2 ft. of RG 62A/u in series with 100 ft. of RG 9B/u transmission line cable. Characteristic impedance of the former is 93 ohms and of the latter 50 ohms. Connectors of the GR 874 and BNC types were employed. Two 90° GR elbows connect the pulse generator and

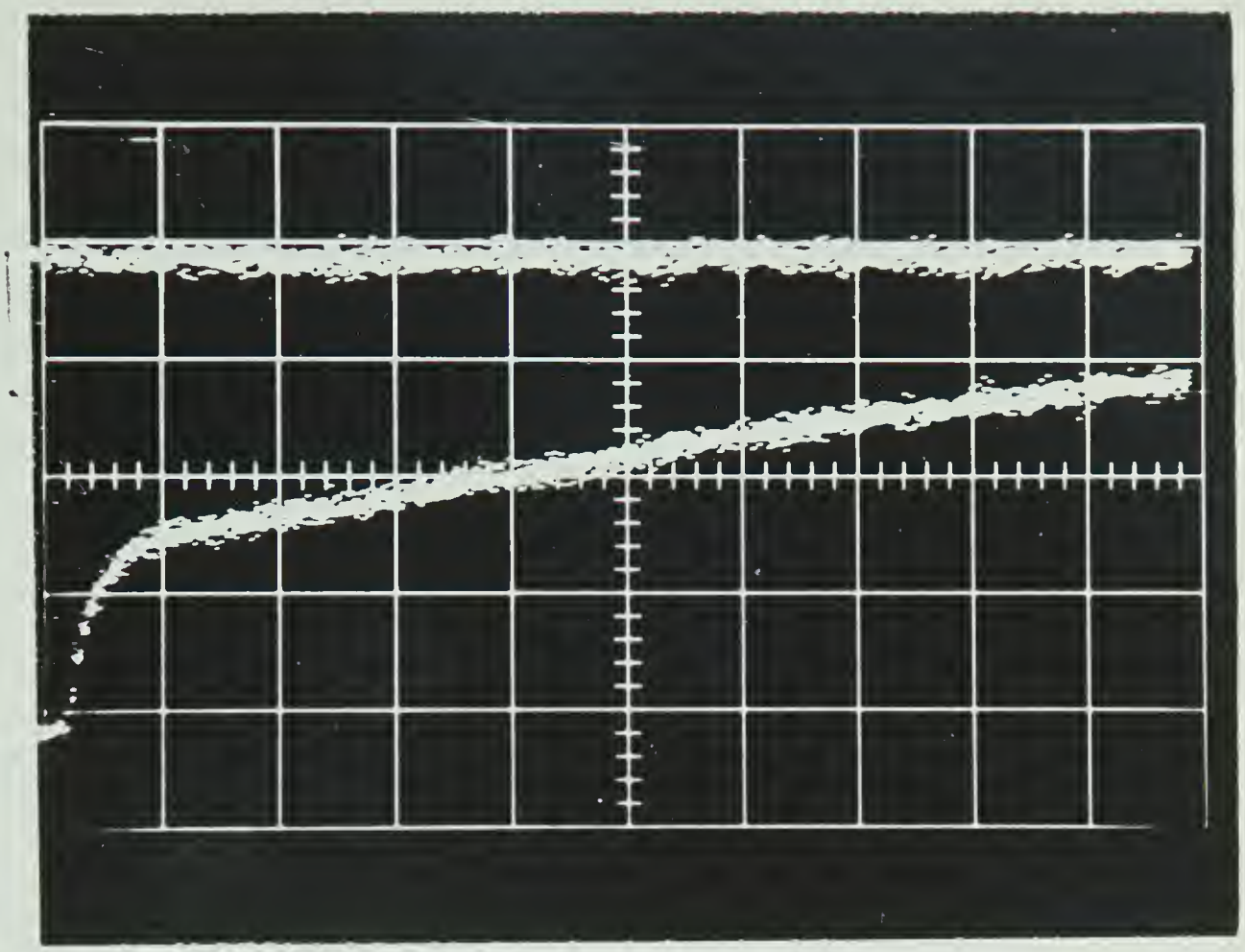

Fig. 37a. Synthetic Circuit TDR Signal

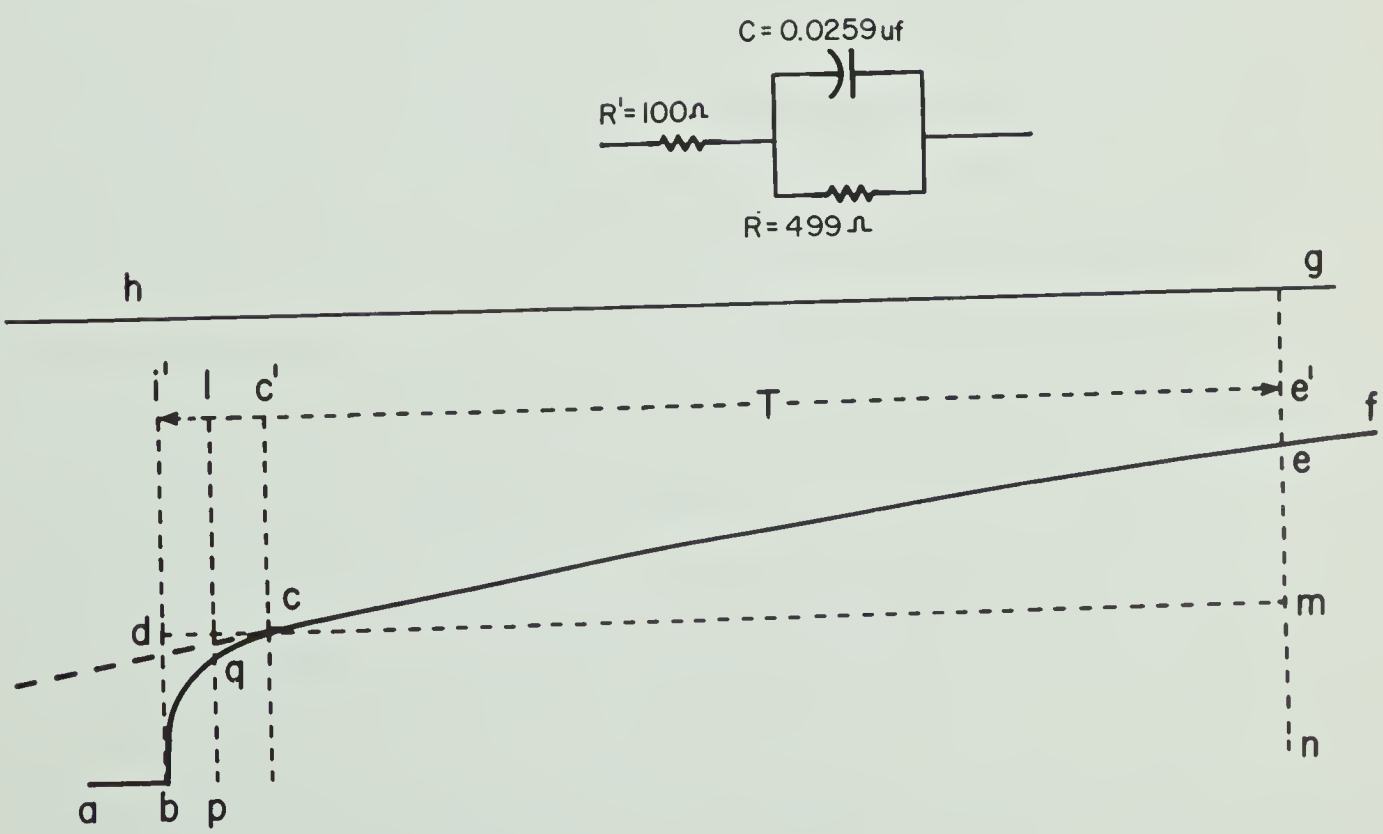

Fig. 37b. Illustration of 37a.

the C.R.O. which monitors the incident and reflected waves. Pulse heights of 1.0 V and 0.25 V are standard on the TDR unit, but attenuators can be employed for obtaining other pulse heights. Pulse durations of 0.2 μsec and 20 μsec are available. The TDR signals were photographed with an Exakta camera using a fast (ASA 3000) green sensitive polaroid land film. Generally, double exposures were necessary to obtain one trace showing the early part of the display for measurement of $v_r(o)$ and a second trace showing the later part of the display for measurement of $v_r(\infty)$.

Results

A TDR display of a synthetic load made from standard ZRC resistors and a standard Aerovox capacitor is reproduced in Figure 37a. Calculations of the parameters R', R_p and C can be made by reference to Figure 37b, stylized illustration of Figure 37a, and the choices of parameters offered. The ab portion of the curve corresponds to the voltage pulse travelling down the 50 ohm RG 9B/u transmission cable. If a longer transmission line was employed, the distance to point b would be extended, to point p perhaps. The vertical position of ab shows the pulse height of 25 mv.

The voltage $v_r(o)$ at time t = 0 is the sum of the pulse voltage and voltage |bc|. Ideally, bc should be vertical*. It should be noted that the 93 ohm impedance of the short piece of RG 62A/u is not separated by the Tektronix 1S2 sampling unit**. The resolution

---

* Hewlett-Packard's 1415 A TDR unit will give a vertical bc resulting in a clear cut measurement of $v_r(o)$.

** The same H.P. instrument can resolve these separate impedances.

is observed if R' is 50 ohms or less. The cf portion of the charging curve is quite linear. By using an opaque projector to obtain a magnification of X3 onto mm graph paper, $v_r(o)$ can be measured very accurately. The trace can be stored in the C.R.O. face and photographed with regular film to give the advantage of slide projection for greater magnification. Applying equation (22), R' is calculated to be 99.99 ohms, which is an accuracy better than 1%.

The upper trace in Figure 37a is the reflection at (effectively) infinite time or the fully charged state of the capacitor. Hence, $v_r(\infty)$ is obviously the sum of the pulse voltage and the voltage $|gn|$. R_p is then calculated from equation (34) to be 490 ohms, or an accuracy of better than 2%.

The half amplitude of the charging curve is taken as one half of gm intersecting the curve at point e. If the half amplitude time $T = |c'e'|$, the capacity calculated from equation (36) is less by 4.3% than the capacity of the capacitor used. If $T = |d'e'|$, the calculated capacity is larger by 7.3%. If, however, T is taken as being from the middle of c'd' to e', i.e., $T = |\ell e'|$, the calculated capacity is 0.02 140 μf or within 1% of the actual value.

The starting point for measurement of both T and $v_r(o)$ is more distinct if R' is made less than 50 ohms as is shown in Figure 38. The impedance of the RG 62A/u transmission cable and the load are resolved.

Figures 39 and 40 show the same effects (of reduced R', i.e., solution resistance) at the type 304 stainless steel-solution interface. The smaller solution resistance in Figure 40 was obtained by placing the working and auxiliary electrode surfaces parallel to one

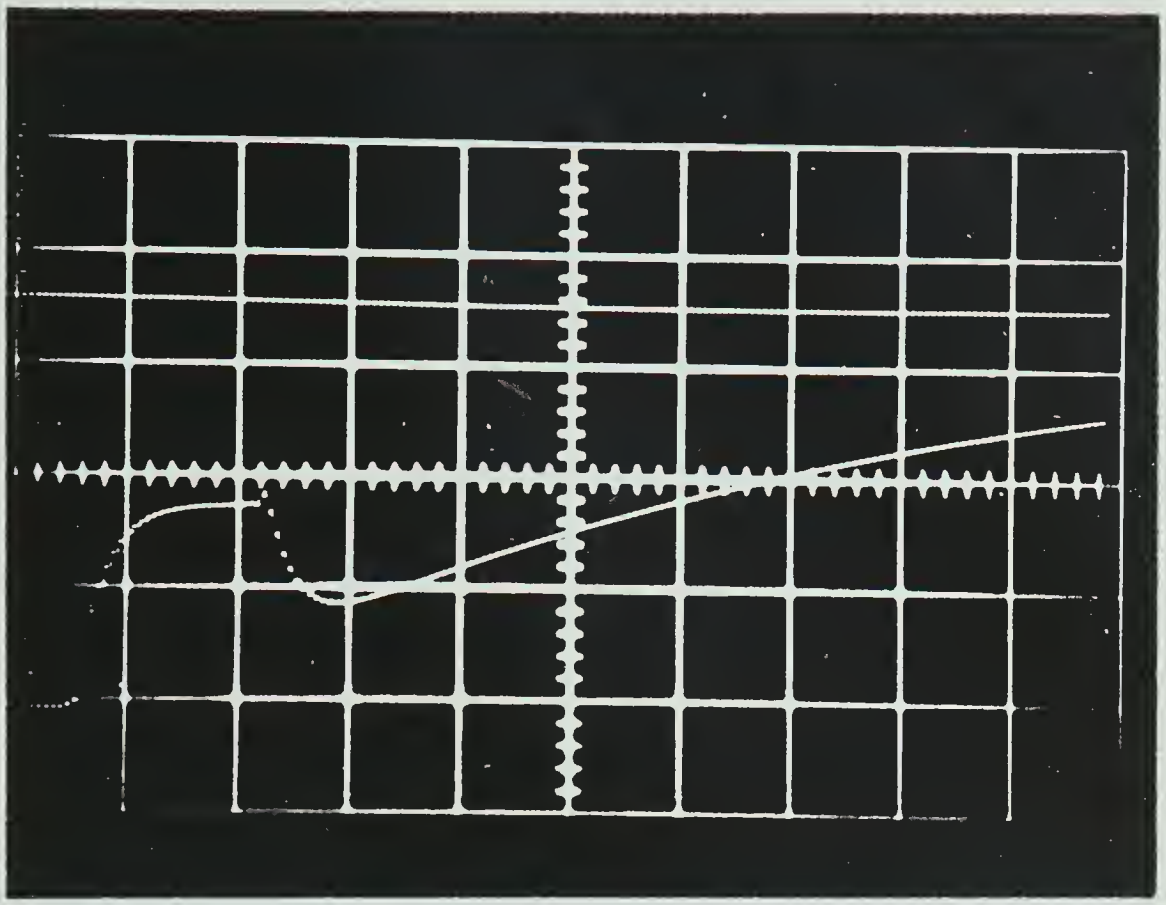

Fig. 38. TDR Display

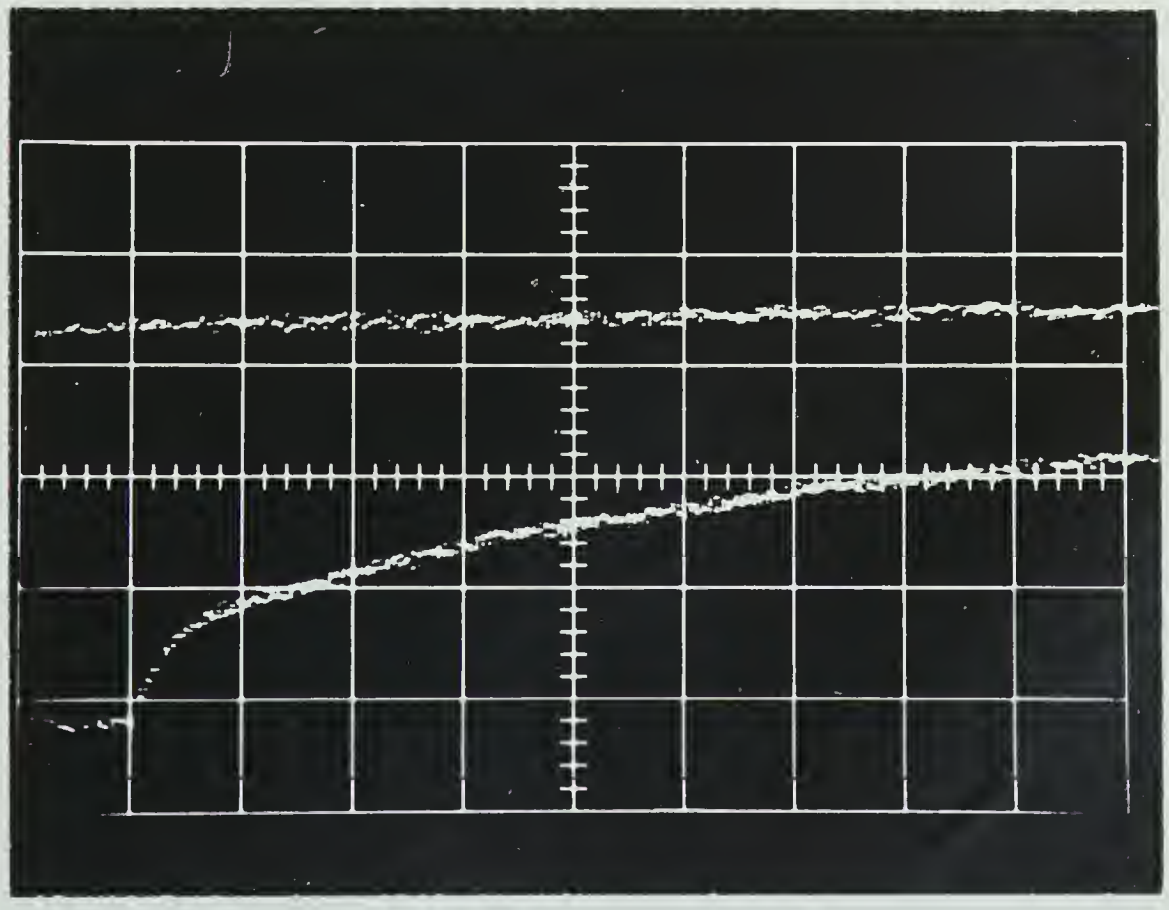

Fig. 39. TDR Display

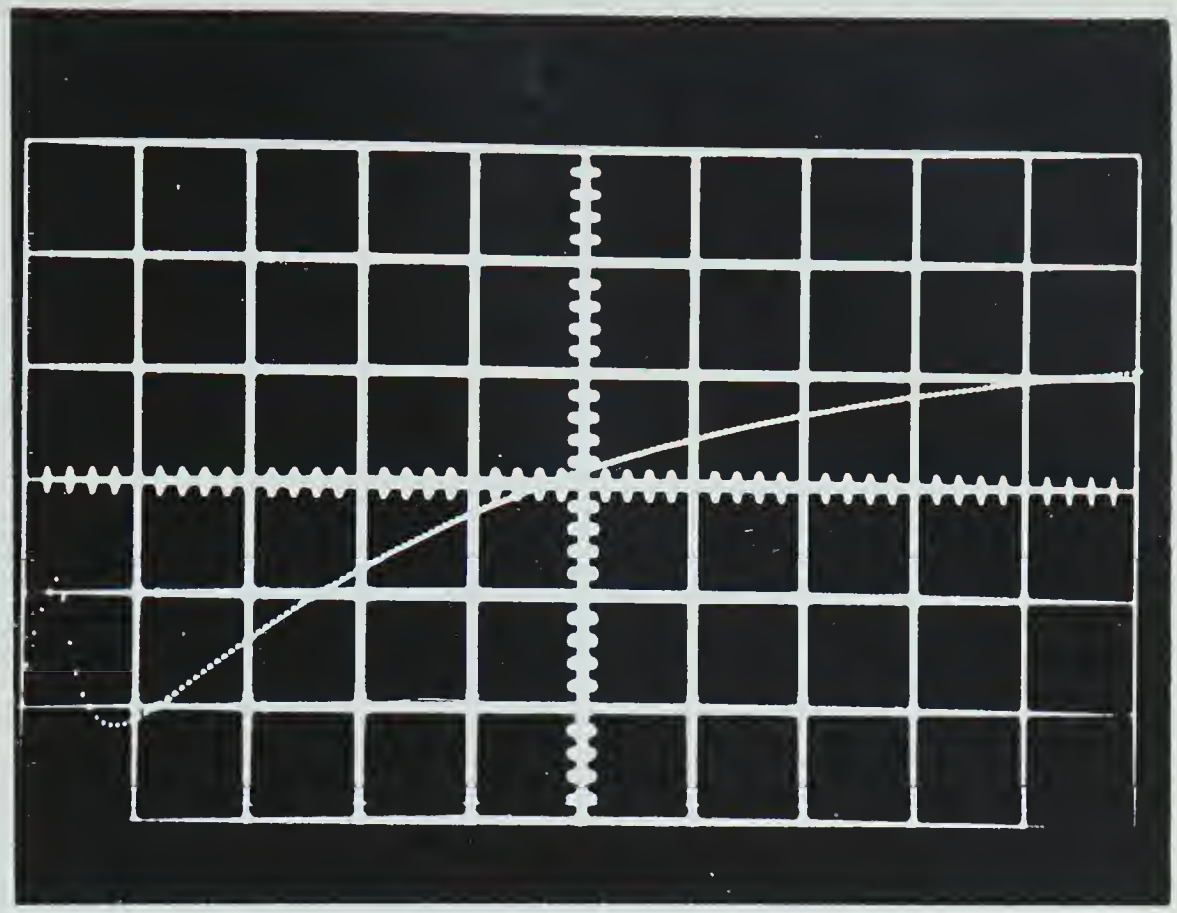

Fig. 40. TDR Display

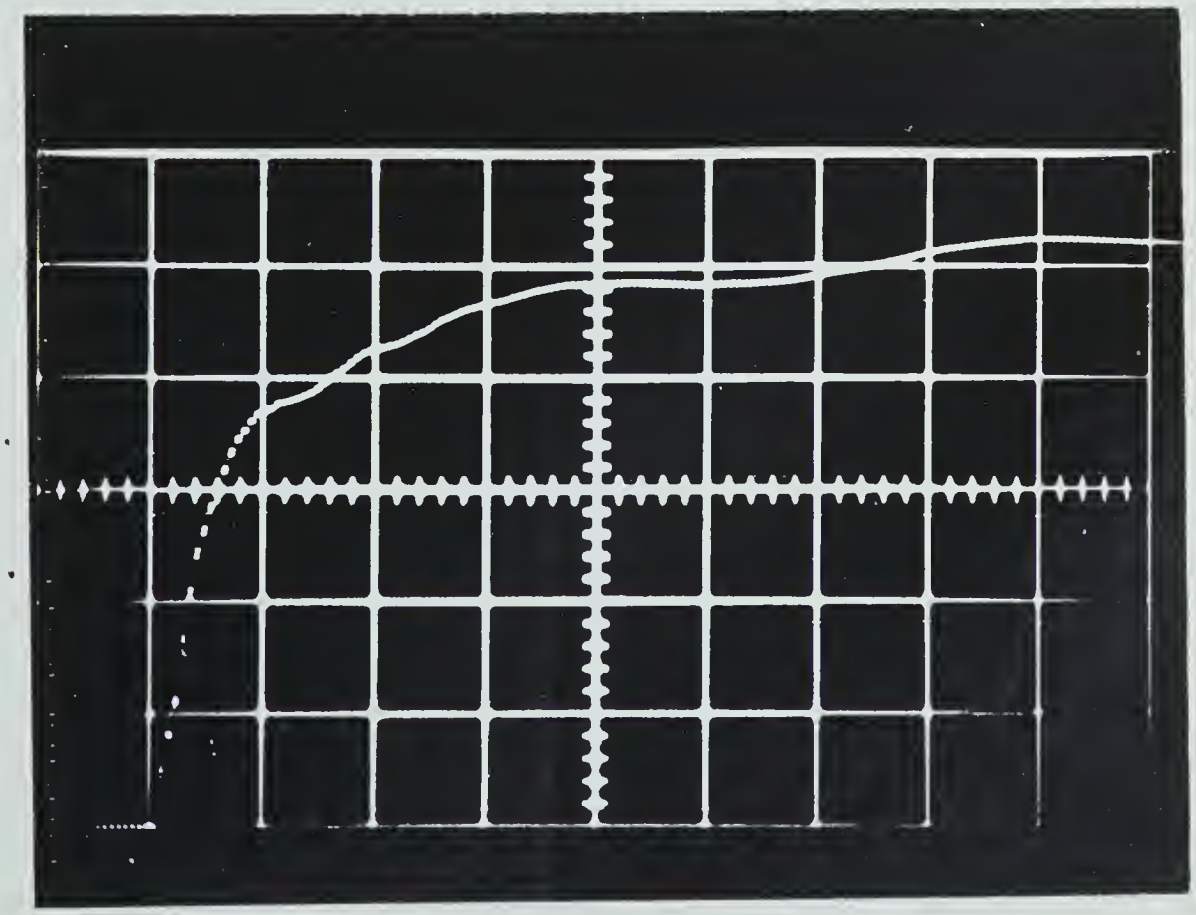

Fig. 41. TDR Display

another at a distance of about 1 mm. Figure 39 is typical of traces obtained with the 90° configuration which results in a higher solution resistance. Since the surface of the auxiliary electrode was much larger than that of the working electrode, the ground of the pulse generator must be connected to the former electrode. The consequence of connecting the ground to the working electrode is shown in Figure 41.

When large pulse heights were employed (1.0 V, 0.25 V and 0.10 V), the electrode potentials measured immediately after the TDR trace was taken were different and often much lower than those found immediately before the TDR determination. Potentials were the same before and after 25 mv TDR pulses.

Capacities measured using the 25 mv pulse for the 90° configuration are compared in Figure 42 with those obtained by the galvanostatic stripping and current interrupter methods. The TDR results are by far the less erratic. Capacity and other electrode parameters obtained by TDR are listed in Table VI.

TABLE VI

Table of Electrode Impedance Parameters

i (mA/cm^2)	E vs HgO/Hg	R_p (ohms)	C ($\mu f/cm^2$)
2.3	-1.322	371	28.5
10.0	-1.416	371	28.5
14.3	-1.441	354	28.3
19.0	-1.453	327	29.5
27.5	-1.485	339	29.3
40.5	-1.507	359	29.4

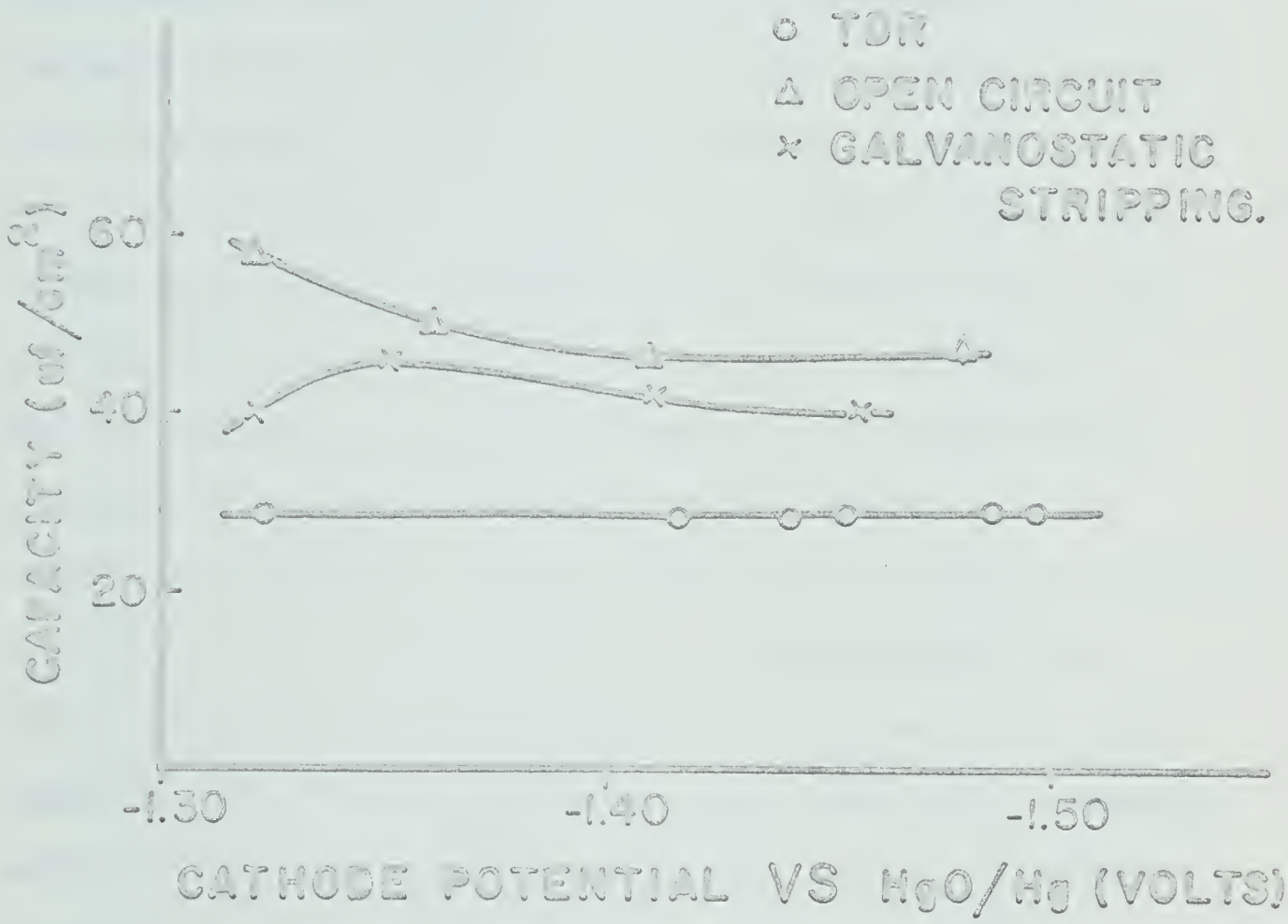

Fig. 42. Comparison of Potential-Capacity Data

Conclusions

It is concluded that time domain reflectometry constitutes an advance over other pulse charging techniques for investigating electrode capacities because the uncertainty of graphical differentiation (a notoriously inaccurate operation) is avoided. A further advantage is that if the electrochemical system to be investigated is well behaved (i.e., can be represented by an analogous electrical circuit), then the other electrode parameters (such as polarization resistance and solution resistance) are also easily and unambiguously obtained. It is further believed that, because of the rapidity of sampling and the display of the total charging curve, if the electrode system is not well behaved (i.e., must be represented by an array of more than one capacitor and resistance in parallel), the deviation from ideality will be obvious and measurable. That is, that if $v_r(t)$ is taken at intervals, say $\tau/2$, $\tau/4$, etc., since $v_r(\infty)$ and $v_r(o)$ are known and hence tentatively all the other parameters in the expression for $v_r(t)$, comparing the calculated and observed $v_r(t)$ should give information about the analogous electrical circuit and, in fact, it should be possible to fit the TDR pattern with a synthetic circuit.

APPENDIX II

Table I - Effect of NaOH Concentration

Stainless Steel 304. 0.1 M NaOH. He saturated

Current (ma)	Current Density (ma/cm^2)	Potential vs. NHE
4.20	9.36	-1.239
3.00	6.69	1.202
2.10	4.68	1.185
1.50	3.24	1.164
1.20	2.67	1.155
0.80	1.78	1.126
0.48	1.071	1.107
0.34	0.759	1.081
0.23	0.513	1.053
0.17	0.379	1.035
0.12	0.268	1.010
0.080	0.178	0.991
0.046	0.102	0.965
0.035	0.078	0.949
0.022	0.050	0.923
0.0155	0.0346	0.901
0.0110	0.0245	0.881
0.008	0.0176	0.851

APPENDIX II

Table II - Effect of NaOH Concentration

Stainless Steel 304. 1.0 M NaOH. He saturated

Current (ma)	Current Density (ma/cm^2)	Potential vs. NHE
6.00	25.6	-1.289
4.20	17.8	1.269
2.85	12.2	1.248
2.10	8.80	1.231
1.40	5.98	1.204
1.00	4.32	1.186
0.625	2.66	1.166
0.440	1.88	1.144
0.295	1.26	1.122
0.205	0.876	1.102
0.140	0.598	1.081
0.105	0.448	1.064
0.070	0.299	1.037
0.0425	0.181	1.013
0.0280	0.118	0.986
0.0190	0.080	0.960
0.0145	0.061	0.939
0.0100	0.0432	0.915

APPENDIX II

Table III - Effect of NaOH Concentration

Stainless Steel 304. 3.0 M NaOH. He saturated

Current (ma)	Current Density (ma/cm^2)	Potential vs. NHE (volt)
4.40	9.83	-1.239
3.10	6.93	1.223
2.15	4.80	1.205
1.50	3.35	1.186
1.20	2.68	1.172
0.80	1.79	1.155
0.485	1.08	1.135
0.340	0.758	1.116
0.230	0.513	1.096
0.170	0.379	1.080
0.115	0.256	1.057
0.085	0.190	1.038
0.046	0.102	1.009
0.0352	0.0786	0.993
0.0225	0.0502	0.966
0.0155	0.0346	0.941
0.0110	0.0246	0.917
0.0080	0.0179	0.894

APPENDIX II

Table IV - Effect of NaOH Concentration

Stainless Steel 304. 5.0 M NaOH. He saturated

Current (ma)	Current Density (ma/cm^2)	Potential vs. NHE
5.60	12.5	-1.230
4.00	8.95	1.213
2.75	6.15	1.194
1.90	4.25	1.176
1.40	3.12	1.152
1.00	2.23	1.144
0.60	1.31	1.124
0.280	0.625	1.087
0.21	0.469	1.072
0.140	0.312	1.049
0.100	0.223	1.030
0.060	0.134	1.004
0.0425	0.0949	0.990
0.0270	0.0602	0.966
0.0190	0.0425	0.947
0.0135	0.0305	0.925
0.0095	0.0212	0.892

APPENDIX II

Table V - Effect of NaOH Concentration

Stainless Steel 304. 10 M NaOH. He saturated

Current (ma)	Current Density (ma/cm^2)	Potential vs. NHE
3.70	8.26	-1.235
2.7	6.03	1.222
2.0	4.47	1.207
1.5	3.35	1.198
1.2	2.68	1.186
0.80	1.79	1.172
0.53	1.18	1.157
0.380	0.849	1.141
0.260	0.581	1.126
0.19	0.424	1.113
0.13	0.290	1.101
0.090	0.201	1.073
0.053	0.118	1.045
0.040	0.089	1.030
0.0260	0.0580	1.005
0.0180	0.0400	0.985
0.0120	0.0260	0.968
0.009	0.0200	0.953

APPENDIX II

Table VI - Effect of NaOH Concentration

Stainless Steel 304. 0.1 M NaOH He and then H_2 saturated

Current (ma)	Current Density (ma/cm^2)	Potential vs. NHE
2.80	11.96	-1.298
2.20	9.40	1.283
1.65	7.05	1.265
1.14	4.78	1.240
0.87	3.72	1.226
0.62	2.65	1.205
0.43	1.84	1.180
0.30	1.28	1.163
0.205	0.876	1.130
0.155	0.662	1.110
0.105	0.448	0.086
0.075	0.320	1.064
0.0425	0.181	1.036
0.0330	0.141	1.022
0.021	0.090	0.992
0.015	0.064	0.967
0.010	0.042	0.945
0.0075	0.032	0.918

APPENDIX II

Table VII - Effect of NaOH Concentration

Stainless Steel 304. 1.0 M NaOH. He and then H_2 saturated

Current (ma)	Current Density (ma/cm^2)	Potential vs. NHE
3.16	13.5	-1.335
2.40	10.2	1.314
1.7	7.26	1.294
1.3	5.55	1.273
0.90	3.84	1.257
0.65	2.78	1.239
0.45	1.92	1.215
0.32	1.37	1.195
0.21	0.897	1.171
0.16	0.683	1.154
0.10	0.427	1.129
0.080	0.341	1.107
0.045	0.192	1.079
0.034	0.145	1.051
0.022	0.094	0.997
0.0155	0.066	0.957

APPENDIX II

Table VIII - Effect of NaOH Concentration

Stainless Steel 304. 3.0 M NaOH. He and then H_2 saturated

Current (ma)	Current Density (ma/cm^2)	Potential vs. NHE
2.95	12.6	-1.293
2.20	9.42	1.284
1.60	6.86	1.266
1.14	4.87	1.250
0.87	3.71	1.236
0.625	2.66	1.219
0.435	1.86	1.200
0.305	1.30	1.182
0.210	0.900	1.160
0.160	0.683	1.143
0.105	0.448	1.112
0.080	0.341	1.096
0.044	0.190	1.067
0.034	0.145	1.049
0.022	0.094	1.018
0.0150	0.064	0.992
0.0110	0.047	0.966
0.0075	0.032	0.932

APPENDIX II

Table IX - Effect of NaOH Concentration

Stainless Steel 304. 5.0 M NaOH. He and then H_2 saturated

Current (ma)	Current Density (ma/cm^2)	Potential vs NHE
2.70	11.3	-1.307
2.20	9.40	1.297
1.60	6.83	1.283
1.20	5.12	1.266
0.87	3.71	1.252
0.625	2.67	1.235
0.43	1.83	1.217
0.305	1.30	1.200
0.205	0.876	1.183
0.160	0.683	1.168
0.105	0.448	1.147
0.080	0.333	1.129
0.0440	0.188	1.103
0.0335	0.143	1.088
0.0215	0.091	1.059
0.0150	0.064	1.035
0.0105	0.044	1.013
0.0075	0.032	0.998

APPENDIX II

Table X - Effect of NaOH Concentration

Stainless Steel 304. 10 M NaOH He and then H_2 saturated

Current (ma)	Current Density (ma/cm^2)	Potential vs. NHE
2.70	11.1	-1.290
2.20	9.40	1.278
1.7	7.26	1.266
1.16	4.96	1.252
0.89	3.70	1.240
0.635	2.71	1.225
0.440	1.88	1.210
0.315	1.34	1.195
0.215	0.92	1.179
0.160	0.683	1.166
0.11	0.470	1.148
0.080	0.341	1.132
0.045	0.192	1.109
0.034	0.145	1.094
0.0215	0.091	1.069
0.0150	0.064	1.047
0.0105	0.045	1.027

APPENDIX II

Table XI - Effect of Sodium Halides

Stainless Steel 304. 3.0 M NaOH and 0.1 M NaCl

Current (ma)	Current Density (ma/cm^2)	Potential vs. NHE
2.70	11.5	-1.299
2.15	9.19	1.279
1.60	6.83	1.259
1.12	4.78	1.239
0.86	3.67	1.223
0.61	2.60	1.201
0.425	1.81	1.179
0.300	1.28	1.157
0.205	0.876	1.132
0.160	0.683	1.112
0.105	0.448	1.089
0.080	0.341	1.071
0.043	0.183	1.047
0.033	0.141	1.032
0.021	0.089	1.008
0.015	0.064	0.989

APPENDIX II

Table XII - Effect of Sodium Halides

Stainless Steel 304. 3.0 M NaOH and 1.0 M NaCl

Current (ma)	Current Density (ma/cm^2)	Potential vs. NHE
2.70	11.5	-1.291
2.10	8.97	1.279
1.60	6.83	1.263
1.09	4.67	1.245
0.84	3.59	1.231
0.60	2.56	1.212
0.42	1.79	1.191
0.30	1.28	1.171
0.205	0.876	1.148
0.150	0.641	1.129
0.105	0.448	1.103
0.0800	0.341	1.084
0.0425	0.181	1.055
0.0335	0.147	1.039
0.0210	0.0897	1.012
0.015	0.064	0.990

APPENDIX II

Table XIII - Effect of Sodium Halides

Stainless Steel 304. 3.0 M NaOH and 3.0 M NaCl

Current (ma)	Current Density (ma/cm^2)	Potential vs. NHE (volt)
2.25	9.01	-1.288
1.80	7.65	1.277
1.40	5.98	1.263
1.05	4.49	1.247
0.65	2.78	1.235
0.55	2.35	1.218
0.39	1.67	1.200
0.285	1.22	1.181
0.200	0.853	1.161
0.150	0.641	1.146
0.100	0.427	1.121
0.070	0.299	1.101
0.042	0.179	1.073
0.0325	0.138	1.057
0.0210	0.089	1.028
0.0145	0.062	1.006
0.0105	0.044	0.987

APPENDIX II

Table XIV - Effect of Sodium Halides

Stainless Steel 304. 0.1 M NaOH and 2.9 M NaCl

Current (ma)	Current Density (ma/cm^2)	Potential vs. NHE (volts)
3.60	15.4	-1.297
2.65	11.3	1.281
1.95	8.33	1.266
1.45	6.19	1.249
1.02	4.36	1.234
0.72	3.05	1.214
0.53	2.26	1.192
0.355	1.51	1.171
0.240	1.02	1.149
0.180	0.769	1.132
0.120	0.512	1.110
0.090	0.384	1.093
0.0490	0.209	1.069
0.0373	0.159	1.055
0.0240	0.102	1.031
0.0167	0.071	1.008
0.0120	0.051	0.987

APPENDIX II

Table XV - Effect of Sodium Halides

Stainless Steel 304. 0.1 M NaOH and 4.9 M NaCl

Current (ma)	Current Density (ma/cm^2)	Potential vs. NHE (volts)
2.95	12.6	-1.270
2.30	9.83	1.253
1.70	7.26	1.234
1.15	4.92	1.218
0.88	3.76	1.204
0.63	2.69	1.183
0.43	1.83	1.158
0.305	1.30	1.136
0.210	0.897	1.112
0.160	0.683	1.096
0.105	0.448	1.074
0.075	0.320	1.057
0.047	0.200	1.029
0.033	0.141	1.007
0.0215	0.096	0.996

APPENDIX II

Table XVI - Effect of Sodium Halides

Stainless Steel 304. 3.0 M NaOH and 0.001 M NaI

Current (ma)	Current Density (ma/cm^2)	Potential vs. NHE (volts)
2.60	11.1	-1.269
1.90	8.11	1.255
1.40	5.98	1.240
0.98	4.19	1.223
0.70	2.99	1.209
0.48	2.05	1.191
0.34	1.50	1.173
0.235	1.00	1.152
0.180	0.769	1.135
0.120	0.512	1.107
0.085	0.363	1.089
0.0480	0.205	1.061
0.0365	0.156	1.045
0.0235	0.100	1.019

APPENDIX II

Table XVII - Effect of Sodium Halides

Stainless Steel 304. 3.0 M NaOH and 0.01 M NaI

Current (ma)	Current Density (ma/cm^2)	Potential vs. NHE (volts)
3.05	13.0	-1.271
2.40	10.2	1.258
1.80	7.69	1.242
1.35	5.77	1.227
0.96	4.10	1.213
0.59	2.52	1.195
0.48	2.05	1.173
0.34	1.45	1.152
0.235	1.00	1.129
0.180	0.769	1.109
0.120	0.512	1.084
0.090	0.384	1.065
0.048	0.205	1.037
0.0365	0.156	1.021
0.0235	0.100	0.995
0.0165	0.070	0.974
0.0115	0.049	0.955

APPENDIX II

Table XVIII - Effect of Sodium Halides

Stainless Steel 304. 3.0 M NaOH and 0.1 M NaI

Current (ma)	Current Density (ma/cm^2)	Potential vs. NHE (volts)
2.70	11.5	-1.278
2.10	8.97	1.270
1.60	6.83	1.257
1.14	4.87	1.244
0.89	3.80	1.232
0.660	2.82	1.215
0.465	1.99	1.195
0.335	1.43	1.176
0.230	0.982	1.154
0.175	0.747	1.138
0.120	0.512	1.111
0.085	0.363	1.091

APPENDIX II

Table XIX - Effect of Halide Ion Size

1.0 M NaOH. Potential vs. 1.0 M NaOH/HgO/Hg
(+ 0.100 V. vs. NHE)

Current (ma)	Current Density (ma/cm^2)	Potential vs. HgO/Hg (volts)
6.00	25.6	-1.392
4.20	17.8	1.372
2.85	12.1	1.351
2.10	8.80	1.334
1.40	5.98	1.307
1.00	4.32	1.289
0.625	2.66	1.269
0.440	1.88	1.247
0.295	1.26	1.225
0.205	0.876	1.205
0.140	0.598	1.184
0.105	0.448	1.167
0.070	0.299	1.140
0.0425	0.181	1.116
0.0280	0.118	1.089
0.0190	0.081	1.063
0.0145	0.061	1.042
0.0100	0.0432	1.018

APPENDIX II

Table XX - Effect of Halide Ion Size

1.0 M NaOH and 0.1 M NaF

Current (ma)	Current Density (ma/cm^2)	Potential vs. HgO/Hg (volts)
6.00	25.6	-1.383
4.25	17.7	1.364
2.90	12.4	1.343
2.15	9.18	1.326
1.40	5.98	1.300
0.925	3.95	1.280
0.640	2.73	1.260
0.445	1.90	1.240
0.300	1.28	1.220
0.215	0.910	1.199
0.145	0.618	1.180
0.105	0.448	1.160
0.070	0.299	1.135
0.0430	0.183	1.115
0.0290	0.123	1.089
0.0200	0.085	1.064
0.0150	0.0640	1.044
0.0105	0.0441	1.019

APPENDIX II

Table XXI - Effect of Halide Ion Size

1.0 M NaOH and 0.1 M NaCl

Current (ma)	Current Density (ma/cm^2)	Potential vs. HgO/Hg (volts)
5.60	23.9	-1.400
4.00	17.0	1.378
2.65	11.3	1.358
1.80	7.66	1.338
1.34	5.72	1.315
0.920	3.93	1.291
0.605	2.58	1.266
0.415	1.77	1.243
0.270	1.15	1.216
0.200	0.854	1.196
0.128	0.549	1.168
0.0920	0.383	1.146
0.0560	0.239	1.114
0.0425	0.181	1.093
0.0270	0.115	1.051
0.0180	0.0768	1.003
0.0131	0.0557	0.953
0.0092	0.0397	0.905

APPENDIX II

Table XXII - Effect of Halide Ion Size

1.0 M NaOH and 0.1 M NaI

Current (ma)	Current Density (ma/cm^2)	Potential vs. HgO/Hg (volts)
5.85	25.0	-1.420
4.20	17.9	1.393
2.85	12.1	1.385
2.00	8.54	1.364
1.50	6.41	1.347
1.05	4.48	1.327
0.63	2.69	1.302
0.440	1.88	1.274
0.300	1.23	1.250
0.220	0.940	1.232
0.145	0.619	1.206
0.105	0.448	1.185
0.070	0.299	1.154
0.0450	0.192	1.137
0.0285	0.121	1.106
0.0200	0.0854	1.082
0.0140	0.0598	1.061
0.0100	0.0427	1.040

APPENDIX II

Table XXIII - Effect of Cation Charge

1.0 M NaOH and 0.1 M $BaCl_2$

Current (ma)	Current Density (ma/cm^2)	Potential vs. HgO/Hg (volt)
5.75	24.6	-1.366
4.10	17.5	1.333
2.80	11.9	1.313
1.95	8.34	1.292
1.45	6.20	1.277
1.00	4.27	1.260
0.61	2.61	1.240
0.425	1.81	1.222
0.285	1.21	1.203
0.210	0.897	1.187
0.140	0.598	1.167
0.100	0.427	1.149
0.065	0.278	1.126
0.0430	0.184	1.113
0.0275	0.117	1.089
0.0190	0.0812	1.072
0.0135	0.0576	1.056
0.0095	0.0406	1.038

APPENDIX II

Table XXIV - Effect of Cation Charge

3.0 M NaOH and 0.05 M $LaCl_3$

Current (ma)	Current Density (ma/cm^2)	Potential vs. HgO/Hg (volt)
3.40	14.5	-1.323
2.55	10.9	1.310
1.85	7.90	1.295
1.40	5.98	1.281
0.99	4.23	1.269
0.71	3.03	1.252
0.49	2.09	1.233
0.35	1.49	1.216
0.24	1.02	1.196
0.180	0.77	1.179
0.120	0.513	1.157
0.090	0.384	1.137
0.0485	0.207	1.111
0.0370	0.158	1.098

APPENDIX II

Table XXV - Effect of Another Reducible Species

1.0 M NaOH and 0.001 M $NaIO_3$

Current (ma)	Current Density (ma/cm^2)	Potential vs. HgO/Hg
3.45	7.70	-1.340
2.80	6.25	1.320
2.10	4.69	1.296
1.60	3.57	1.246
1.20	2.68	1.196
0.815	1.81	1.053
0.560	1.25	1.045
0.400	0.891	1.018
0.265	0.588	1.022
0.200	0.448	1.008
0.130	0.290	0.978
0.100	0.223	0.956
0.0560	0.125	0.934
0.0420	0.0938	0.927
0.0270	0.0603	0.900
0.0185	0.0413	0.878
0.0130	0.0290	0.854
0.0095	0.0201	0.833

APPENDIX II

Table XXVI - Effect of Another Reducible Species

1.0 M NaOH and 0.01 M $NaIO_3$

Current (ma)	Current Density (ma/cm^2)	Potential vs. HgO/Hg (volt)
3.45	7.70	-1.368
2.80	6.25	1.351
2.10	4.68	1.330
1.60	3.56	1.305
1.20	2.67	1.278
0.900	2.00	1.244
0.560	1.25	1.200
0.400	0.892	1.077
0.265	0.590	1.027
0.200	0.446	1.011
0.130	0.289	0.992
0.100	0.223	0.981
0.0600	0.133	0.953
0.0420	0.0937	0.946
0.0270	0.0602	0.917
0.0185	0.0413	0.905
0.0130	0.0289	0.882
0.0095	0.0200	0.854

APPENDIX II

Table XXVII - Effect of Another Reducible Species

1.0 M NaOH and 0.1 M $NaIO_3$

Current (ma)	Current Density (ma/cm^2)	Potential vs. HgO/Hg (volt)
3.45	7.70	-1.080
2.80	6.25	1.052
2.10	4.68	1.025
1.60	3.56	1.000
1.20	2.67	0.976
0.81	1.81	0.950
0.560	1.25	0.922
0.400	0.892	0.897
0.270	0.602	0.868
0.200	0.446	0.849
0.135	0.301	0.820
0.100	0.223	0.798
0.0560	0.126	0.768
0.0425	0.0948	0.757
0.0270	0.0602	0.731
0.0185	0.0413	0.713
0.0130	0.0289	0.692
0.0095	0.0200	0.678

APPENDIX II

Table XXVIII - High Current Density Studies

Stainless Steel 304. Area = 0.020 $cm.^2$ 1.0 M NaOH

Current (ma)	Current Density (ma/cm^2)	Potential vs. HgO/Hg (volts)
0.036	1.30	-1.207
0.13	6.50	1.272
0.37	13.5	1.336
1.30	65.0	1.413
3.60	180.0	1.494
7.40	370	1.562
11.3	665	1.601
17.5	875	1.640
21	1050	1.700
24.0	1200	1.73
27.0	1350	1.80
34.5	1725	1.90
40.0	2000	2.02
50.0	2500	2.20
56.0	2800	2.45
64.0	3200	2.68
80.0	4000	3.04
86.0	4300	3.24

APPENDIX II

Table XXIX - Effect of Ammonia

3.0 M NaOH. Potential vs. 3.0 M NaOH/HgO/Hg
(vs. +0.069 v. vs. N.H.E.)

Current (ma)	Current Density (ma/cm^2.)	Potential vs. HgO/Hg (volt)
4.40	9.83	-1.339
3.10	6.93	1.323
2.15	4.80	1.305
1.50	3.35	1.286
1.20	2.68	1.272
0.80	1.79	1.255
0.485	1.08	1.235
0.340	0.758	1.216
0.230	0.513	1.196
0.170	0.379	1.186
0.115	0.256	1.157
0.085	0.190	1.138
0.046	0.102	1.109
0.0352	0.0786	1.093
0.0225	0.0502	1.066
0.0155	0.0346	1.041
0.0110	0.0246	1.017
0.0080	0.0179	0.994

APPENDIX II

Table XXX - Effect of Ammonia

3.0 M NaOH and 0.01 M NH_4OH

Current (ma)	Current Density (ma/cm^2)	Potential vs. HgO/Hg (volts)
2.50	10.7	-1.340
2.00	8.54	1.332
1.50	6.41	1.310
1.10	4.70	1.298
0.87	3.71	1.278
0.645	2.75	1.264
0.455	1.94	1.249
0.330	1.41	1.233
0.225	0.961	1.214
0.170	0.726	1.199
0.120	0.512	1.176
0.085	0.363	1.160
0.0475	0.203	1.132
0.0363	0.154	1.116
0.0233	0.099	1.089
0.0163	0.069	1.066
0.0115	0.043	1.043
0.0085	0.036	1.025

APPENDIX II

Table XXXI - Effect of Ammonia

3.0 M NaOH and 0.1 M NH_4OH

Current (ma)	Current Density (ma/cm^2)	Potential vs. HgO/Hg (volts)
3.70	15.8	-1.338
2.80	11.9	1.323
2.05	8.76	1.306
1.50	6.41	1.288
1.06	4.53	1.272
0.75	3.20	1.252
0.51	2.18	1.229
0.36	1.54	1.209
0.245	1.04	1.185
0.185	0.790	1.167
0.120	0.512	1.142
0.090	0.384	1.124
0.0495	0.211	1.097
0.0375	0.160	1.081
0.0242	0.103	1.056
0.0169	0.072	1.037

APPENDIX II

Table XXXII - Effect of Electrodeposition of Elements on Electrode Surface

1.0 M NaOH. 50% of surface covered with Fe

Current (ma)	Current Density (ma/cm^2)	Potential vs. HgO/Hg (volt)
6.00	13.4	-1.335
4.20	0.38	1.319
2.85	6.36	1.298
2.10	4.68	1.280
1.40	3.12	1.256
1.00	2.23	1.238
0.635	1.41	1.216
0.440	0.985	1.196
0.300	0.670	1.173
0.210	0.468	1.155
0.105	0.234	1.114
0.070	0.156	1.092
0.0430	0.091	1.072
0.0285	0.063	1.048
0.0195	0.043	1.026
0.0150	0.033	1.011
0.0105	0.0234	0.991

APPENDIX II

Table XXXIII - Effect of Electrodeposition of Elements on Electrode Surface

1.0 M NaOH. 100% Fe

Current (ma)	Current Density (ma/cm^2)	Potential vs. HgO/Hg (volt)
5.75	12.8	-1.287
4.05	9.04	1.269
2.80	6.25	1.246
2.05	4.58	1.226
1.40	3.12	1.195
1.00	2.23	1.174
0.620	1.38	1.152
0.435	0.973	1.132
0.300	0.670	1.113
0.205	0.458	1.092
0.140	0.312	1.075
0.105	0.234	1.063
0.070	0.156	1.045
0.0420	0.0938	1.031
0.0282	0.0630	1.017
0.0192	0.0429	1.003
0.0145	0.0324	0.995
0.0105	0.0234	0.982

APPENDIX II

Table XXXIV - Effect of Electrodeposition of Elements on Electrode Surface

1.0 M NaOH. 5% Ni

Current (ma)	Current Density (ma/cm^2)	Potential vs. HgO/Hg (volt)
5.70	12.7	-1.267
4.05	8.04	1.247
2.80	6.25	1.222
1.90	4.24	1.201
1.40	3.12	1.183
1.00	2.23	1.164
0.605	1.35	1.144
0.425	0.940	1.125
0.280	0.625	1.104
0.210	0.469	1.090
0.140	0.312	1.069
0.100	0.223	1.052
0.070	0.156	1.030
0.0430	0.0960	1.017
0.0275	0.0614	0.998
0.0190	0.0424	0.981
0.0135	0.0307	0.968
0.0100	0.0223	0.943

APPENDIX II

Table XXXV - Effect of Electrodeposition of Elements on Electrode Surface

1.0 M NaOH. 10% Ni

Current (ma)	Current Density (ma/cm^2)	Potential vs. HgO/Hg (volts)
5.60	12.5	-1.231
4.00	8.93	1.217
2.80	6.25	1.191
1.90	4.24	1.169
1.40	3.12	1.153
1.00	2.23	1.129
0.605	1.35	1.104
0.420	0.938	1.081
0.280	0.625	1.056
0.210	0.469	1.037
0.140	0.312	1.002
0.100	0.223	0.960
0.070	0.156	0.540
0.0430	0.0960	0.257
0.0280	0.0625	0.200
0.0190	0.0424	0.1800
0.0140	0.0312	0.160
0.0100	0.0223	0.143

APPENDIX II

Table XXXVI - Effect of Electrodeposition of Elements on Electrode Surface

1.0 M NaOH. 20% Ni

Current (ma)	Current Density (ma/cm^2)	Potential vs. HgO/Hg (volt)
5.65	12.6	-1.307
4.05	9.04	1.282
2.80	6.25	1.252
1.90	4.24	1.225
1.45	3.24	1.204
1.00	2.23	1.178
0.605	1.35	1.153
0.420	0.938	1.130
0.280	0.625	1.110
0.210	0.469	1.096
0.140	0.312	1.077
0.100	0.223	1.063
0.070	0.156	1.045
0.0430	0.0960	1.035
0.0275	0.0614	1.018
0.0190	0.0424	1.006
0.0135	0.0307	0.989
0.0100	0.0223	0.969

APPENDIX II

Table XXXVII - Effect of Alteration of the Nature of Electrode Surface

1.0 M NaOH. Electrode pickled with 1.1 HCl and H_2SO_4 mixture

Current (ma)	Current Density (ma/cm^2)	Potential vs. HgO/Hg (volt)
5.20	11.6	-1.137
3.65	8.15	1.124
2.45	5.46	1.111
1.80	4.01	1.099
1.20	2.67	1.084
0.800	1.70	1.072
0.560	1.25	1.061
0.385	0.856	1.048
0.260	0.580	1.035
0.180	0.401	1.021
0.125	0.278	1.007
0.090	0.201	0.995
0.0550	0.122	0.979
0.0375	0.0835	0.963
0.0250	0.0556	0.948
0.0170	0.0378	0.937
0.0130	0.0289	0.913
0.0090	0.0201	0.890

APPENDIX II

Table XXXVIII - Effect of Alteration of the Nature of the Electrode Surface

1.0 M NaOH. After 44 hours of electrolysis at 12.5 ma/cm^2

Current (ma)	Current Density (ma/cm^2)	Potential vs. HgO/Hg (volt)
5.60	12.5	-1.350
3.95	8.82	1.326
2.65	5.91	1.300
1.85	4.13	1.274
1.40	3.12	1.253
1.00	2.23	1.224
0.590	1.317	1.193
0.41	0.914	1.164
0.275	0.613	1.134
0.200	0.446	1.105
0.140	0.312	1.060
0.100	0.223	1.012
0.0555	0.124	0.927
0.0420	0.0937	0.856
0.0270	0.0602	0.807
0.0185	0.0412	0.716
0.0130	0.0290	0.665
0.00920	0.0205	0.632

APPENDIX II

Table XXXIX - Comparison with Stainless Steel 304

Stainless Steel 310. 0.322 cm^2 1.0 M NaOH

Current (ma)	Current Density (ma/cm^2)	Potential vs. HgO/Hg (volt)
4.30	13.4	-1.384
3.10	9.65	1.360
2.15	0.70	1.335
1.50	4.67	1.311
1.15	3.58	1.291
0.80	2.90	1.268
0.480	1.50	1.245
0.340	1.06	1.220
0.23	0.715	1.200
0.17	0.531	1.183
0.120	0.374	1.159
0.080	0.293	1.140
0.0460	0.143	1.111
0.035	0.109	1.093
0.0225	0.070	1.060
0.0155	0.0482	1.030
0.0110	0.0343	0.997
0.0080	0.029	0.964

REFERENCES

[1] P. Delahay, Double Layer and Electrode Kinetics, Interscience (New York), 1965, p. 1.

[2] J. O'M. Bockris and A. M. Azzam, Trans. Faraday Soc., 48, 145 (1952).

[3] J. O'M. Bockris and R. G. H. Watson, J. Chim. Phys., 49, C70 (1952).

[4] A. C. Makrides, J. Electrochem. Soc., 109, 977 (1962).

[5] J. O'M. Bockris and E. C. Potter, J. Chem. Phys., 20, 614 (1952).

[6] N. Pentland, J. O'M. Bockris, and E. Sheldon, J. Electrochem. Soc., 104, 182 (1957).

[7] M. A. V. Devanathan and M. Selvaratnam, Trans. Faraday Soc., 56, 1820 (1960).

[8] H. H. Uhlig, Corrosion and Corrosion Control, Wiley (New York), 1963.

[9] T. N. Rhodin, Corrosion, 12, 123t (1956).

[10] R. Parsons, Mod. Aspects of Electrochemistry, ed. J. O'M. Bockris, Vol. I., Butterworths (London), 1954, p. 103.

[11] A. Helmholtz, Wiss. Abb. Phys. Tech., Reichonst, 1, 925 (1879).

[12] B. E. Conway, Theory and Principles of Electrode Processes, Ronald Press (New York), 1964, p. 38.

[13] G. Gouy, J. Phys. Rad., 9, 457 (1910).

[14] D. L. Chapman, Phil. Mag., 25, 475 (1913).

[15] J. Malsch, Z. Physik., 29, 770 (1928).

[16] O. Stern, Z. Elektrochem., 30, 508 (1924).

[17] D. C. Grahame, Chem. Rev., 41, 441 (1947).

[18] M. A. V. Devanathan, J. O'M. Bockris, and K. Müller, Proc. Roy. Soc., London, A274, 55 (1963).

[19] J. R. MacDonald, J. Chem. Phys., 22, 1857 (1954).

[20] N. F. Mott and R. J. Watts-Tobin, Electrochim. Acta, 4, 79 (1961).

[21] D. M. Mohilner, Electroanal. Chemistry, ed. A. J. Bard, Dekker (New York) 1966, p. 244.

[22] M. Breiter, P. Delahay, and M. Kleinerman, J. Am. Chem. Soc., 90, 5111 (1958).

[23] T. Erdey-Gruz and M. Volmer, Z. Phys. Chem., 150A, 203 (1930); 157A, 165 (1931).

[24] R. W. Guerny, Ionic Processes in Solution, McGraw-Hill (New York), 1953.

[25] J. A. V. Butler, Proc. Roy. Soc., 157A, 423 (1936).

[26] S. G. Christov, Z. Elektrochem., 62, 567 (1958).

[27] B. E. Conway, Can. J. Chem., 37, 178 (1959).

[28] W. F. Libby, J. Phys. Chem., 56, 863 (1952).

[29] R. A. Marcus, Can. J. Chem. 37, 155 (1959).

[30] N. S. Hush, Trans. Faraday Soc., 57, 557 (1961).

[31] P. Delahay, New Instrumental Methods in Electrochemistry, Interscience (New York), 1954).

[32] K. J. Vetter, Electrochemical Kinetics, Transl. ed. S. Bruckenstein and B. Howard, Academic Press (New York), 1967.

[33] L. Young, Anodic Oxide Films, Academic Press (New York), 1961, p. 345.

[34] C. A. Hampel, ed., The Encyclopedia of Electrochemistry, Reinhold (New York), 1964.

[35] K. R. Williams, ed., An Introduction to Fuel Cells, Elsevier (London), 1966.

[36] E. C. Potter, Electrochemistry, Cleaver-Hume (London), 1956, p. 124.

[37] S. Glasstone, K. J. Laidler, and H. Eyring, The Theory of Rate Processes, McGraw-Hill (New York), 1941.

[38] J. O'M. Bockris, Modern Aspects of Electrochemistry, ed. J. O'M. Bockris, Vol. I, Butterworths (London), 1954, p. 180.

[39] R. Parsons and J. O'M. Bockris, Trans. Faraday Soc., 47, 914 (1951).

[40] P. Delahay, J. Am. Chem. Soc., 74, 3497 (1952).

[41] R. N. O'Brien and K. V. N. Rao, J. Electrochem. Soc., 112, 1245 (1965).

[42] D. J. G. Ives and G. J. Janz, Reference Electrodes, Academic Press, New York, London, 1961.

[43] S. Barnartt, J. Electrochem. Soc., 108, 102 (1961).

[44] G. R. Hoey and M. Cohen, J. Electrochem. Soc., 106, 776 (1959).

[45] G. Kortüm, Treatise on Electrochemistry, Elsevier, Amsterdam, 1965, p. 447.

[46] M. A. V. Devanathan, J. O'M. Bockris, and W. Mehl, J. Electroanal. Chem., 1, 143 (1959).

[47] S. Shuldiner, Recent Progress in Surface Science, eds. Danielli et al, Vol. 1, Academic Press (New York and London), 1964, Chapter 4, p. 159.

[48] E. Gileadi and B. E. Conway, Modern Aspects of Electrochemistry, ed. J. O'M. Bockris, Vol. III, Butterworths (London), 1964, p. 347.

[49] Handbook of Chemistry and Physics, 45th ed., The Chemical Rubber Co., (Cleveland), 1964-1965.

[50] C. L. Mantell, Electrochemical Engineering, 4th ed., McGraw-Hill, (New York), 1960, p. 92.

[51] J. O'M. Bockris, J. Chem. Phys., 24, 817 (1956).

[52] D. C. Grahame, Chem. Rev., 41, 441 (1947).

[53] J. O'M. Bockris, W. Mehl, B. E. Conway, and L. Young, J. Chem. Phys., 25, 776 (1956).

[54] J. O'M. Bockris and B. E. Conway, J. Chem. Phys., 28, 707 (1958).

[55] H. B. Morley and F. E. W. Wetmore, Can. J. Chem., 34, 359 (1956).

[56] M. A. V. Devanathan, Z. Starchurski and W. Beck, J. Electrochem. Soc., 110, 886 (1964).

[57] H. A. Kozlowska and B. E. Conway, J. Electroanal. Chem., 7, 109 (1964).

[58] Time Domain Reflectometry, Application Note 62, Hewlett-Packard Co., (1964).

[59] H. H. Skilling, Fundamentals of Electric Waves, 2nd ed., John Wiley, New York (1948), p. 145.

[60] H. Gupta, Transform and State Variable Methods in Linear Systems, J. Wiley, New York (1966), Chapter 1 and 3.

[61] B. E. Conway and J. O'M. Bockris, J. Chem. Phys., 26, 532 (1957).

[62] J. O'M. Bockris and S. Srinivasan, J. Electroanal. Chem., 11, 350 (1966).

[63] H. H. Uhlig, Corrosion Handbook, John Wiley (New York), 1966.

[64] P. V. Popat and N. Hackerman, J. Phys. Chem., 65, 1201 (1961).

[65] A. C. Makrides, J. Electrochem. Soc., 113, 1158 (1966).

[66] A. Frumkin, Disc. Faraday Soc., 1, 57 (1947).

[67] M. Pourbaix, Atlas of Electrochemical Equilibria in Aqueous Solutions, Pergamon Press (New York), 1966, p. 263.

[68] E. A. Gulbransen and K. E. Andrew, J. Electrochem. Soc., 104, 334 (1957).

[69] R. Piontelli, L. Peraldo Bicelli and A. Lallecchia, Rend. Accad. Naz. Pincei, VIII, 27, 312 (1959).